UNIVERSITY OF BELGRADE

FACULTY OF PHYSICS

Dragan S. Prekrat

PHASE TRANSITIONS IN MATRIX MODELS ON THE TRUNCATED HEISENBERG SPACE

Doctoral Dissertation

Belgrade, 2023

UNIVERZITET U BEOGRADU

FIZIČKI FAKULTET

Dragan S. Prekrat

FAZNI PRELAZI MATRIČNIH MODELA NA MODIFIKOVANOM HAJZENBERGOVOM PROSTORU

doktorska disertacija

Beograd, 2023

SUPERVISOR

Dr Maja Burić
Full Professor
University of Belgrade, Faculty of Physics

ADVISORY COMMITTEE

Dr Voja Radovanović
Full Professor
University of Belgrade, Faculty of Physics

Dr Dragoljub Gočanin
Assistant Research Professor
University of Belgrade, Faculty of Physics

Dr Antun Balaž
Research Professor
Institute of Physics Belgrade

DEFENSE DATE

March 3, 2023

Acknowledgments

> *"Our lives are not our own. We are bound to others, past and present, and by each crime and every kindness, we birth our future."*
>
> *David Mitchell, Cloud Atlas*

Firstly, I would like to sincerely thank my supervisor Prof. Maja Burić for inspiration, all the advice, and, most importantly, endless patience on the rocky road leading here.

I am greatly thankful to my colleagues from the Department of Physics and Mathematics at the University of Belgrade – Faculty of Pharmacy for teamwork, enormous encouragement, and frequent gentle pushes forward. I am also indebted to Prof. Denjoe O'Connor and Dr Samuel Kováčik for helping me enter the world of Monte Carlo simulations and Dr Juraj Tekel for a very stimulating collaboration.

Special thanks go to my noncommutative comrade Dr Luka Nenadović, together with whom I have struggled in the first half of the PhD game, and to my ex-roommate-at-faculty Dr Mirjana Vojnović for rooting for me all along.

The journey here would not be possible without the financial support of SEENET-MTP, LMU, COST, DIAS, and Project no. ON171031 of Serbian Ministry of Education, Science and Technological Development. In addition, I thank LMU and DIAS for their hospitality.

Last but by no means least, I would like to thank my family for their love and support and to my friends for keeping me sane and for being understanding throughout the past 12 years.

Phase transitions in matrix models on the truncated Heisenberg space

Abstract

In this dissertation, we study a self-interacting Hermitian matrix field in two dimensions coupled to the curvature of the noncommutative truncated Heisenberg space. In the infinite size limit, the model reduces to the renormalizable Grosse-Wulkenhaar's. We inspect the connection between the model's curvature term, UV/IR mixing, and renormalizability.

The model is numerically simulated using the Hybrid Monte Carlo method. In order to obtain the nontrivial phase structure, we first vary the scalings of the action term parameters and inspect the transition line stability under the change of matrix size. After we fix the scalings, we proceed to construct the phase diagrams and find their large matrix size limits. As a result, we establish the presence of the three phases previously found in other matrix models — the ordered, the disordered, and a purely noncommutative striped phase.

The curvature term proves crucial for the diagram's structure: when turned off, the triple point collapses into the origin as matrices grow larger; when turned on, the triple point recedes from the origin proportionally to the coupling strength and the matrix size. We use both the field eigenvalue distribution approach and a bound on the action to predict the position of the transition lines. Their simulated curvature-induced shift convincingly agrees with our analytical results.

We found that the coupling attenuation that turns the Grosse-Wulkenhaar model into a renormalizable version of the $\lambda\phi^4_\star$-model cannot stop the triple point recession. As a result, the stripe phase escapes to infinity, removing the problems with UV/IR mixing and explaining the success of the Grosse-Wulkenhaar model.

KEYWORDS

Noncommutative geometry • Grosse-Wulkenhaar model • Matrix models
Phase transitions • Renormalizability • Monte Carlo simulations

SCIENTIFIC FIELD

Physics

RESEARCH AREA

Noncommutative Quantum Field Theory

UDC NUMBER

530.122.3(043.3)
544.015.4:530.23(043.3)

Fazni prelazi u matričnim modelima na modifikovanom Hajzenbergovom prostoru

Rezime

U ovoj disertaciji, izučavamo samointeragujuće hermitsko matrično polje na koga deluje krivina nekomutativnog modifikovanog Hajzenbergovog prostora. U limesu beskonačnih matrica, ovaj model se svodi na renormalizabilni Grose-Vulkenharov. Cilj je da se ispita veza između člana sa krivinom, UV/IR mešanja i renormalizabilnosti modela.

Numeričkoj simulaciji modela smo pristupili Hibridnim Monte Karlo metodom. Radi dobijanja netrivijalne strukture faznog dijagrama, prvo variramo skaliranje parametara članova u dejstvu i ispitujemo stabilnost linija faznih prelaza pri promeni veličine matrica. Nakon što smo fiksirali skaliranje, konstruišemo fazne dijagrame i nalazimo njihove limese. Na ovaj način smo utvrdili pristustvo tri faze prethodno detektovane kod drugih matričnih modela — uređene, neuređene i čisto nekomutativne trakaste faze.

Član sa krivinom se pokazao presudnim po strukturu dijagrama: kada je uključen, trojna tačka modela kolapsira u koordinatni početak prostora parametara s povećanjem formata matrica; kada je isključen, trojna tačka se udaljava od koordinatnog početka srazmerno parametru krivine i veličini matrice. Za predviđanje položaja linija faznih prelaza, koristili smo metod raspodela svojstvenih vrednosti polja kao i procenjivanje granica na vrednosti samog dejstva. Simulirane vrednosti ovog krivinom izazvanog pomeranja se ubedljivo slažu sa našim analitičkim rezultatima.

Brizina isključivanja parametra krivine koje pretvara Grose-Vulkenharov model u renormalizabilnu verziju $\lambda\phi^4_\star$ modela je nedovoljna da zaustavi udaljavanje trojne tačke od koordinatnog početka. Posledica toga je da trakasta faza nestaje u beskonačnosti, rešavajući problem UV/IR mešanja, čime smo objasnili uspešnost Grose-Vulkenharovog modela.

KLJUČNE REČI

Nekomutativna geometrija • Grose-Vulkenharov model • Matrični modeli
Fazni prelazi • Renormalizabilnost • Monte Karlo simulacije

NAUČNA OBLAST

Fizika

UŽA NAUČNA OBLAST

Nekomutativna kvantna teorija polja

UDK BROJ

530.122.3(043.3)
544.015.4:530.23(043.3)

List of Publications

Publications whose content constitutes part of this dissertation are listed below.

1. D. Prekrat, K. N. Todorović-Vasović, and D. Ranković, "Detecting scaling in phase transitions on the truncated Heisenberg algebra," *J. High Energy Phys.* 03 (2021) 197, DOI: 10.1007/JHEP03(2021)197

   Dragan Prekrat performed the bulk of the data gathering and analysis. The co-authors performed simulations leading in part to Figures 3 and 11 in this article. The article contributed to:

   - Chapter 3, Section 1,
   - Chapter 4, Sections 1-5,
   - Appendix E,
   - Appendix C.

2. D. Prekrat, "Renormalization footprints in the phase diagram of the Grosse-Wulkenhaar model," *Phys. Rev. D* 104, 114505 (2021), DOI: 10.1103/PhysRevD.104.114505

   The article contributed to:

   - Chapter 1,
   - Chapter 4, Section 6,
   - Chapter 5, Sections 1-3,
   - Chapter 6,
   - Appendix A,
   - Appendix F.

Contents

1 Introduction and overview **1**

2 From NC QTF to matrix models **5**
2.1 NC algebras and products 5
2.2 UV/IR mixing 9
2.3 Grosse-Wulkenhaar's model 12

3 Phase transition simulation **15**
3.1 Matrix model 15
3.2 Hybrid Monte Carlo 21
3.3 Autocorrelation 24

4 Submodels and phase diagrams **29**
4.1 Parameter scaling 29
4.2 Potential term scaling 31
4.3 Kinetic term scaling 34
4.4 Curvature term scaling 39
4.5 *R*-off diagram 42
4.6 *R*-on diagram 45

5 Renormalization footprints **53**
5.1 Triple point proxies 53
5.2 *R*-off triple point 55
5.3 *R*-on triple point 56
5.4 Gauge model 58

6 Conclusions and outlook **61**

A Model correspondence **65**

B Eigenvalue distributions **67**

C Critical exponents and transition order **73**

D False vacua **79**

E Transition line coefficients **83**

F Triple point extrapolations **87**

G Curvature terms in the effective action **89**

List of Symbols and Abbreviations 97

Bibliography 99

List of Figures

2.1 (Non-)planar self-energy diagrams. 11

3.1 Simulated examples of theromodynamical observables (without curvature). . 17
3.2 Simulated examples of matrix field averages. 20
3.3 Simulated example of a probable matrix field configuration. 21
3.4 Simulation history example for the trace of the field 22
3.5 Simulation history example for the action. 23
3.6 Autocorrelation functions with residuals. 25
3.7 Large lag autocorrelation functions. 26
3.8 Large lag autocorrelation function modeling. 27
3.9 Residuals of transition-line fits. 28

4.1 3rd order transition in the pure potential model. 31
4.2 Scaling variants in the pure potential model. 32
4.3 Scaling variants of the kinetic term. 35
4.4 Scaling variants of the kinetic term. 36
4.5 Transition line parameters in the large matrix size limit. 37
4.6 Scaling variants of the curvature term. 40
4.7 Eigenvalue and trace distributions for the curvature term. 41
4.8 Phase diagrams (without curvature). 43
4.9 Phase diagram in the large matrix limit (without curvature). 44
4.10 Simulated examples of thermodynamics observables (with curvature). 46
4.11 Eigenvalue distribution for the curvature-modified vacuum. 47
4.12 Phase diagram contour plot (without curvature). 48
4.13 Phase diagram contour plot (with curvature). 49

5.1 Intersection of transition line extrapolations. 53
5.2 Detection of triple-point proxies. 54
5.3 Triple point location in the large matrix size limit (without curvature). 55
5.4 Triple point location for varying curvature parameter. 57

B.1 Theoretical vs. simulated eigenvalue distribution in the disordered phase. . . 70
B.2 Theoretical vs. simulated eigenvalue distribution in the striped phase. 71

C.1 Collapsed diagrams for thermodynamic observables. 74
C.2 Collapsed diagrams for thermodynamic observables. 75
C.3 The new phase susceptibility scaling. 76

D.1 Thermodynamical observables around false vacua. 81

E.1 Transitions for the kinetic term scaling variants in the large matrix size limit. . 84

List of Tables

4.1 Fit parameters for scaling variants in the pure potential model. 33
4.2 Analytical vs. simulated results for the transition points. 50
4.3 Transition line equations: the curvature shift. 51

6.1 Comparison of the renormalizability and the phase structure across models. . 62

C.1 Comparison of critical exponents. 76

E.1 Transition line parameters for the kinetic term scaling variants. 83

F.1 Fits of the triple-point position. 87

Chapter 1

Introduction and overview

> *"Then you should say what you mean," the March Hare went on.*
> *"I do," Alice hastily replied; "at least—at least I mean what I say—that's the same thing, you know."*
> *"Not the same thing a bit!" said the Hatter. "You might just as well say that 'I see what I eat' is the same thing as 'I eat what I see'!"*
>
> *Lewis Carroll, Alice in Wonderland*

We are often challenged to explain what we do in just a few words. What springs to mind in connection to noncommutative QFT is: CERN in Wonderland. A realm where space and time behave oddly and the rules are a bit off. As if that were not enough, even the chit-chat at the Hatter's tea party [1] seems to be inspired by the noncommutative quaternions [2].

Some seven decades later, in the 1940s, noncommutativity (NC) arrived from Wonderland to Quantumland, settling first in the canonical relation between position and momentum and shortly after—passed down from Heisenberg to Peierls, to Pauli, to Oppenheimer, and finally to Snyder [3]—into NC spacetime.

Noncommutativity of spacetime coordinates was initially proposed in the hope of resolving the confusion about the infinities in the nascent quantum field theory [4]. The first promising results in this regard were, however, achieved by the technique of renormalization. Since then, NC has occasionally reemerged, both in the fundamental and the effective form, from condensed matter physics to quantum gravity [5, 6]. Finally, when NC was discovered in the low energy sector of the string theory at the turn of the millennium [7], various new NC models followed.

Contrary to the expected better-than-commutative behavior, NC models experience more difficulties with renormalizability. Generically, their non-planar Feynman diagrams entangle small and large length scales, which prevents a successful absorption of divergences into the action terms [8, 9, 10, 11]. It was shown that this UV/IR mixing could be resolved by the proper balancing of the scales provided by the Langman-Szabo duality [12].

Grosse-Wulkenhaar (GW) model [13, 14, 15]

$$S_{\mathrm{GW}} = \int \frac{1}{2}(\partial\phi)^2 + \frac{\Omega^2}{2}((\theta^{-1}x)\phi)^2 + \frac{m^2}{2}\phi^2 + \frac{\lambda}{4!}\phi^4$$

managed to evade the UV/IR mixing problem. It features a self-interacting real scalar field on the Moyal space equipped with a $\star$-product

$$f \star g = f\, e^{i/2\,\overleftarrow{\partial}\theta\overrightarrow{\partial}}\, g \quad \Rightarrow \quad [x^\mu, x^\nu]_\star = i\theta^{\mu\nu}.$$

Its potential is enhanced by the external harmonic oscillator term of a possible gravitational origin. Namely, the model can be reinterpreted [16] as that of a scalar field in a curved NC space of the truncated Heisenberg algebra $\mathfrak{h}^{\mathrm{tr}}$:

$$S_{\mathfrak{h}} = \int \sqrt{g}\left(\frac{1}{2}(\partial\phi)^2 - \frac{\xi}{2}R_{\mathfrak{h}}\phi^2 + \frac{m_{\mathfrak{h}}^2}{2}\phi^2 + \frac{\lambda_{\mathfrak{h}}}{4!}\phi^4\right).$$

The oscillator Ω-term, which holds the key to renormalizability, is now seen as a coupling to the coordinate-dependant curvature $R_{\mathfrak{h}}$. Another possible source of the oscillator term was presented in [17], where it elegantly appears in the expansion of the kinetic term of the free scalar field situated in the Snyder-de Sitter space. This model also predicts the running of the curvature coupling, which is an essential ingredient of the GW-mediated $\lambda\phi_\star^4$-renormalizability. It would be interesting to see if similar conclusions could be reached in the fuzzy de Sitter space [18, 19].

UV/IR mixing still poses a problem for gauge fields on NC spaces [20]. Hoping to build on the GW model's success, [21, 22] tried to adapt it to a gauge field on $\mathfrak{h}^{\mathrm{tr}}$. Still, after extensive treatment, we found nonrenormalizability lurking in the form of divergent non-local derivative counterterms [23]. Apart from the trivial vacuum, it turned out this model contains another, which breaks the translational invariance. This echoes the translational symmetry-breaking stripe phase that seems to be at the root of UV/IR mixing. Its "stripes" refer to patterns of spatially non-uniform magnetization, which appear when the field oscillates around different values at different points in space [24, 25, 26]. They also seem to shatter the symmetry between large and small scales that keeps the UV/IR mixing in check: locally, the vacuum appears ordered, but globally, watched through the lenses of spatial averaging, it looks smudged into a disordered zero. This motivated us to find out what happens with the stripe phase in the GW model and to see how the model's renormalizability plays out from the phase transition point of view. We suspect that the presence of the striped phase in the phase diagram is equivalent to the nonrenormalizability of a model. More specifically, in this dissertation, we test the hypothesis that the GW model's diagram is stripe phase-free.

Phase diagrams on NC spaces have been extensively studied in various matrix models, since they regularize corresponding continuum theories in a numerical simulation-friendly fashion [27, 28, 29, 30, 31, 32, 33, 34, 35, 36, 37, 38, 39, 40, 41, 42, 43, 44, 45, 46, 47, 48]. They generically feature three phases that meet at a triple point. Two of these are readily present in commutative theories: in the disordered phase, field eigenvalues clump around zero; in the ordered phase, however, they gather around one of the mirror image-minima of the potential. The third one is a matrix counterpart of the NC stripe phase in which eigenvalues simultaneously gather around the positive and negative minimum. We, too, approached the testing of our hypothesis using the numerical Monte Carlo simulations of the particular matrix regularization of the two-dimensional GW model. The analytical investigation of the phases can be done along several lines. First, if we know how to solve the equations for the eigenvalue distribution [35, 38, 39, 43, 48], we can compute and compare the free energy in the three phases and decide in which phase it is minimized. We can also look at the distributions' features and from them extract constraints on the extension of the phases. This, however, requires a multi-trace expansion [30] of the non-diagonalizable kinetic part of the partition function integral into an infinite series of products of traces of powers of the field. Another, in essence, Wilsonian, approach is to establish a kind of a renormalization group flow in matrix size [49, 50, 51], recursively connecting adjacent matrix sizes and integrating differing vector degrees of freedom. In this dissertation, we found a few analytical results by computing bounds on the action and by exploiting the distribution approach in combination with the Harish-Chandra-Itzykson-Zuber (HCIZ) formula [52, 53].

The main body of this dissertation is organized as follows. Chapter 2 touches upon the necessary concepts in the noncommutative quantum field theories. Specifically, we introduce the $\mathfrak{h}^{\mathrm{tr}}$ space, UV/IR mixing, and the GW model. In Chapter 3, we proceed to define our matrix model and the relevant observables and discuss the Hybrid Monte Carlo method used for its numerical simulations. In Chapter 4, we inspect and fix the scalings of the action terms/parameters, construct the phase diagrams and find their large matrix size limits. We establish the presence of the three phases also found in other matrix models — the ordered, the disordered, and a purely noncommutative striped phase. Chapter 5 then deals with the connection between the renormalizability and the phase structure. We compare the model with (R-on) and without (R-off) the curvature term and look at the behavior of the triple point, which controls the extension of the problematic stripe phase. We inspect how the model bares under the oscillator term switch-off procedure that ensures the $\lambda\phi^4_\star$-model's renormalizability and find that the stripe phase is pushed out of the phase diagram into infinity. We finally conclude our study with Chapter 6. Appendices contain additional simulation data and more details of the calculations and data fits.

Chapter 2

From NC QTF to matrix models

This chapter introduces some mathematical and physical ideas on whose shoulders rests the main topic of this dissertation. We first start with the NC algebras, specifically the Moyal NC plane and its close relative truncated Heisenberg algebra. We then introduce a quantum field theory on NC space and explore unexpected problems with UV/IR mixing.

This chapter does not contain our original contributions, and its purpose is to set a stage for our analysis. We do not go too deeply into the details, and more rigorous treatments (as well as refreshing reviews) can be found in [41, 54, 55, 56].

2.1 NC algebras and products

In order to explore physics down the ladder of shrinking length scales, we need to use increasingly large energy densities. Unfortunately, this would eventually lead to the formation of a micro black hole, cutting off the access to the observed point. This type of argument implies that (our knowledge of) classical continuous spacetime breaks down at small distances. As a remedy, inspired by canonical relations between position and momenta in QM and by the quantization of its phase-space, we can promote the commutative coordinates into noncommutative operators

$$[\hat{x}^\mu, \hat{x}^\nu] = i\hat{\theta}^{\mu\nu}(x). \tag{2.1.1}$$

The anti-symmetric function $\hat{\theta}$ has dimensions of length squared and is small compared to Standard Model length scales, perhaps as small as the Planck scale. In principle, $\hat{\theta}$ can vary from point to point. On such a space — similarly to the phase space of QM — holds a spacetime uncertainty principle,

$$\Delta\hat{x}^\mu \Delta\hat{x}^\nu \geq \frac{|\langle\hat{\theta}^{\mu\nu}\rangle|}{2}, \tag{2.1.2}$$

which immediately hints towards a UV/IR mixing since concentrating on the small scales along one direction forces the averaging over large ones along the other.

We are interested in the simplest case of constant non-commutativity — the Moyal space

$\mathbb{R}^D_\theta$. Its non-commutativity can be expressed as a block-diagonal matrix

$$\hat{\theta}^{\mu\nu}(x) = \theta \bigoplus_{k=1}^{D/2} \epsilon^{\mu\nu}_{(k)} = \theta \bigoplus_{k=1}^{D/2} \begin{pmatrix} & +1 \\ -1 & \end{pmatrix}, \tag{2.1.3}$$

where D is dimension of the space in question. It will be useful to express the NC constant θ in terms of the NC mass scale μ as

$$\theta = \frac{1}{\mu^2}. \tag{2.1.4}$$

We work mainly in $D = 2$ and in (2.1.1) immediately recognize the NC Heisenberg algebra.

The Heisenberg algebra $\mathfrak{h}$ satisfies

$$[x, y] = i, \tag{2.1.5}$$

and it has infinite dimensional matrix representation in the Fock basis (that is, energy basis of harmonic oscillator)

$$x_{ij} = X_{ij} = \frac{1}{\sqrt{2}}(\delta_{i,j+1}\sqrt{j} + \delta_{i+1,j}\sqrt{i}), \tag{2.1.6a}$$

$$y_{ij} = Y_{ij} = \frac{i}{\sqrt{2}}(\delta_{i,j+1}\sqrt{j} - \delta_{i+1,j}\sqrt{i}), \tag{2.1.6b}$$

or using the matrix notation

$$X = \frac{1}{\sqrt{2}} \begin{pmatrix} & +\sqrt{1} & & & \\ +\sqrt{1} & & +\sqrt{2} & & \\ & +\sqrt{2} & & +\sqrt{3} & \\ & & +\sqrt{3} & & \ddots \\ & & & \ddots & \end{pmatrix}, \tag{2.1.7a}$$

$$Y = \frac{i}{\sqrt{2}} \begin{pmatrix} & -\sqrt{1} & & & \\ +\sqrt{1} & & -\sqrt{2} & & \\ & +\sqrt{2} & & -\sqrt{3} & \\ & & +\sqrt{3} & & \ddots \\ & & & \ddots & \end{pmatrix}. \tag{2.1.7b}$$

Once we, in the spirit of the cutoff renormalization, restrict these matrices to $N \times N$ format, they form the truncated Heisenberg algebra $\mathfrak{h}^{\mathrm{tr}}$, defined in [16] as

$$[x,y] = i(1-z), \qquad [x,z] = +i\{y,z\}, \qquad [y,z] = -i\{x,z\}, \tag{2.1.8}$$

with z having the matrix representation $Z_{ij} = N\delta_{i,j}\delta_{i,N}$. Truncated matrices are thus

$$X = \frac{1}{\sqrt{2}} \begin{pmatrix} & +\sqrt{1} & & & & \\ +\sqrt{1} & & +\sqrt{2} & & & \\ & +\sqrt{2} & & +\sqrt{3} & & \\ & & +\sqrt{3} & & \ddots & \\ & & & \ddots & & +\sqrt{N-1} \\ & & & & +\sqrt{N-1} & \end{pmatrix}, \tag{2.1.9a}$$

$$Y = \frac{i}{\sqrt{2}} \begin{pmatrix} & -\sqrt{1} & & & & \\ +\sqrt{1} & & -\sqrt{2} & & & \\ & +\sqrt{2} & & -\sqrt{3} & & \\ & & +\sqrt{3} & & \ddots & \\ & & & \ddots & & -\sqrt{N-1} \\ & & & & +\sqrt{N-1} & \end{pmatrix}, \tag{2.1.9b}$$

$$Z = \begin{pmatrix} \mathbb{0}_{N-1} & \\ & N \end{pmatrix}. \tag{2.1.9c}$$

By introducing the strength ϵ of NC, we can further generalize $\mathfrak{h}^{\mathrm{tr}}$ into the modified truncated Heisenberg algebra $\mathfrak{h}^{\mathrm{tr}}_{\epsilon}$ which satisfies

$$[x,y] = i\epsilon(1-z), \qquad [x,z] = +i\epsilon\{y,z\}, \qquad [y,z] = -i\epsilon\{x,z\}, \tag{2.1.10}$$

This allows us to play with the NC strength and make the following connections in the appropriate limits

$$\text{commutative limit} \quad \xleftarrow{\epsilon\to 0} \quad \mathfrak{h}^{\mathrm{tr}}_{\epsilon} \quad \xrightarrow{\epsilon\to 1} \quad \mathfrak{h}^{\mathrm{tr}} \quad \xrightarrow[N\xrightarrow{w}\infty]{z\to 0} \quad \mathfrak{h}.$$

Algebra $\mathfrak{h}_\epsilon^{\mathrm{tr}}$ is axially symmetric [57] with the rotation generator:

$$\mathcal{M} = i\epsilon(x^2 + y^2 + z). \tag{2.1.11}$$

So far, we have been describing dimensionless coordinates. To make the final connection to (2.1.1), we substitute (x, y, z) with $(\mu x, \mu y, \mu z)$, where x, y, z now have the dimension of length.

In [16], differential calculus was defined on $\mathfrak{h}_\epsilon^{\mathrm{tr}}$ using the frame formalism, forming a curved NC space as a background for scalar, spinor and gauge models. Differentials are generated by the momenta $[p_\alpha, \cdot\,]$. The choice of momenta is not unique, one being

$$\epsilon p_1 = i\mu^2 y, \qquad \epsilon p_2 = -i\mu^2 x, \qquad \epsilon p_3 = i\mu\left(\mu z - \frac{1}{2}\right), \tag{2.1.12}$$

leading to a scalar curvature

$$\begin{aligned} R &= \frac{11\mu^2}{2} + 4i\epsilon\mu p_3 + 8\epsilon^2(p_1^2 + p_2^2) \\ &= \frac{15\mu^2}{2} - 4\epsilon\mu^3 z - 8\epsilon^2\mu^4(x^2 + y^2). \end{aligned} \tag{2.1.13}$$

Other choices have also been studied, leading to the same quadratic form of curvature shifted only by a constant proportional to the identity matrix. In its matrix representation, on the relevant subspace $z = 0$, and in units $\mu = 1$, the curvature has a form:

$$R = \frac{31}{2}\mathbb{1} - 16\begin{pmatrix} 1 & & & & & \\ & 2 & & & & \\ & & 3 & & & \\ & & & \ddots & & \\ & & & & N-1 & \\ & & & & & N/2 \end{pmatrix}_{N\times N}. \tag{2.1.14}$$

In its eigenvalues, we recognize the energy levels of the harmonic oscillator.

Let us now return to Moyal space. Once we introduce the mass scale, it is connected to spaces of our truncated algebras through an infinite matrix limit. The NC of coordinate operators can be viewed as the NC of ordinary functions equipped with an extraordinary star product

$$(f \star g)(x) = \lim_{y,z\to x} \exp\left(\frac{i\theta^{\mu\nu}}{2}\frac{\partial}{\partial y^\mu}\frac{\partial}{\partial z^\nu}\right) f(y)g(z), \tag{2.1.15}$$

or, in a condensed notation

$$f \star g = f\, e^{i/2\,\overleftarrow{\partial}\theta\overrightarrow{\partial}}\, g. \tag{2.1.16}$$

We can expand the right-hand side to see that the first term is just the standard commutative product and the higher terms are NC corrections. We can also easily see that a product of coordinates no longer commutes

$$[x^\mu, x^\nu]_\star = i\theta^{\mu\nu}. \tag{2.1.17}$$

Namely, since higher derivatives are zero, we are left with only the first term of the exponent expansion

$$\begin{aligned}[x^\mu, x^\nu]_\star &= x^\mu \star x^\nu - x^\nu \star x^\mu \\ &= (1 + i\theta^{\mu\nu}/2) - (1 + i\theta^{\nu\mu}/2) = i\theta^{\mu\nu}.\end{aligned} \tag{2.1.18}$$

The star-product has a number of nice properties under integration. When we deal with product of only two functions, we can drop the star and work with the ordinary commutative product

$$\int f_1 \star f_2 = \int f_1 f_2 = \int f_2 f_1. \tag{2.1.19}$$

This means that the propagator of the field living on this space will not be affected by NC. When we add more functions, this leads to cyclicity under the integral

$$\int f_1 \star f_2 \star \cdots \star f_{n-1} \star f_n = \int (f_1 \star f_2 \star \cdots \star f_{n-1}) f_n \tag{2.1.20}$$

$$= \int f_n (f_1 \star f_2 \star \cdots \star f_{n-1}) \tag{2.1.21}$$

$$= \int f_n \star f_1 \star f_2 \star \cdots \star f_{n-1}, \tag{2.1.22}$$

so the integral behaves like a trace, giving the first green light for a trip to the land of matrices.

We are now ready to see what happens when we try to define a simple scalar theory on this unusual space.

2.2 UV/IR mixing

UV/IR mixing in D-dimensional case of scalar $\lambda\phi^4_\star$ is nicely presented in [41]. A 2-dim gauge theory example is found in [58] and [59].

Let us consider a real $\lambda\phi^4_\star$ on a D-dimensional Moyal space

$$S[\phi] = \int \mathrm{d}^D x \left(\phi \left(-\partial^2 + m^2 \right) \phi + \frac{\lambda}{4!} \phi \star \phi \star \phi \star \phi \right). \tag{2.2.23}$$

The background field method, where we decompose the field into a solution of the classical equation of the motion $\phi_\varnothing$ and the quantum fluctuation $\delta\phi$

$$\phi = \phi_\varnothing + \delta\phi, \tag{2.2.24}$$

after integration over fluctuations gives the effective action. In the momentum space, the part that we are interested in, which is quadratic in the field, reads

$$\begin{aligned} S^{(2)}_{\text{eff}} = \int \frac{\mathrm{d}^D p}{(2\pi)^D} |\phi_\varnothing(p)|^2 (p^2 + m^2) + \\ + \frac{\lambda}{4!} \int \frac{\mathrm{d}^D p}{(2\pi)^D} |\phi_\varnothing(p)|^2 \int \frac{\mathrm{d}^D k}{(2\pi)^D} \frac{2 + \exp\left(-ik_i \theta_{ij} p_j\right)}{k^2 + m^2}.\end{aligned} \tag{2.2.25}$$

The first term is just the standard commutative inverse propagator. The second term contains one-loop quantum corrections from planar (pl) and non-planar (np) self-energy diagrams, shown in Figure 2.1:

$$\Sigma_{\text{pl}} = \frac{\lambda}{4!} \int \frac{\mathrm{d}^D k}{(2\pi)^D} \frac{2}{k^2 + m^2}, \tag{2.2.26a}$$

$$\Sigma_{\text{np}} = \frac{\lambda}{4!} \int \frac{\mathrm{d}^D k}{(2\pi)^D} \frac{\exp(-ik_i \theta_{ij} p_j)}{k^2 + m^2} = \frac{\lambda}{4!} \int \frac{\mathrm{d}^D k}{(2\pi)^D} \frac{\exp(-i\theta k \times p)}{k^2 + m^2}. \tag{2.2.26b}$$

The antisymmetric product $\times := \bigoplus \epsilon_{ij}$ notation stresses the non-planar nature of the Σ_{np} diagram ($p \times p = 0$).

We can trade off integration over momenta for integration over dimensionless parameter by using Schwinger parametrization

$$\frac{1}{k^2 + m^2} = \int_0^\infty \mathrm{d}\alpha \, e^{-\alpha(k^2 + m^2)}. \tag{2.2.27}$$

The integral in the non-planar term reads

$$\mathcal{I}_\theta(p) = \int \frac{\mathrm{d}^D k}{(2\pi)^D} \frac{e^{-i\theta k \times p}}{k^2 + m^2} = \frac{1}{(4\pi)^{d/2}} \int_0^\infty \frac{\mathrm{d}\alpha}{\alpha^{d/2}} \, e^{-\alpha m^2 - \frac{(\theta_{ij} p_j)^2}{4\alpha}}. \tag{2.2.28}$$

Its problematic behaviour at the lower bound $\alpha = 0$ can be regularized by multiplying the integrand by the cutoff-dampened exponential

$$\exp\left(-\frac{1}{\alpha \Lambda^2}\right), \tag{2.2.29}$$

leading to

$$\mathcal{I}_\theta(p, \Lambda) = \frac{1}{2\pi} \left(\frac{m \Lambda_{\text{eff}}}{4\pi}\right)^{\frac{D-2}{2}} K_{\frac{D-2}{2}}\left(\frac{2m}{\Lambda_{\text{eff}}}\right), \tag{2.2.30}$$

with the effective cutoff defined as

$$\frac{1}{\Lambda_{\text{eff}}^2} = \frac{1}{\Lambda^2} + \frac{(\theta_{ij} p_j)^2}{4}. \tag{2.2.31}$$

Using the small argument expansion of the modified Bessel function K, we finally obtain

$$\Sigma_{\text{np}} = \begin{cases} \dfrac{\lambda}{96\pi} \log \dfrac{\Lambda_{\text{eff}}^2}{m^2} + \cdots, & D = 2, \\[2ex] \dfrac{\lambda m^2}{384\pi^2} \left(\dfrac{\Lambda_{\text{eff}}^2}{m^2} - \log \dfrac{\Lambda_{\text{eff}}^2}{m^2}\right) + \cdots, & D = 4. \end{cases} \tag{2.2.32}$$

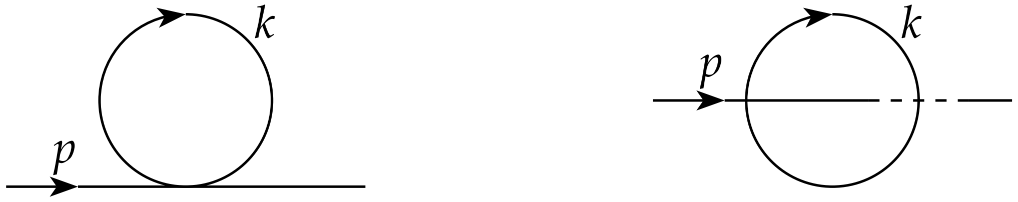

Figure 2.1: Planar (left) and non-planar (right) self-energy Feynman diagrams.

The expressions for Σ_{pl} are obtained by setting $\theta = 0$, i.e. by replacing $\Lambda_{\text{eff}} \to \Lambda$. Putting them together gives the effective action

$$S_{\text{eff}}^{(2)} = \int \frac{\mathrm{d}^2 p}{(2\pi)^2} \left(p^2 + m^2 + \frac{\lambda}{48\pi} \log \frac{\Lambda^2}{m^2} + \frac{\lambda}{96\pi} \log \frac{\Lambda_{\text{eff}}^2}{m^2} \right) |\phi_{\varnothing}(p)|^2. \tag{2.2.33}$$

As we can see, the first log-term in the action can be absorbed in the mass renormalization. The second log-term is finite in the momentum UV regime even after removal of the cutoff. However, in the IR regime $p^2 \to 0$ (and in the naive commutative limit $\theta \to 0$), it causes the two-point function to diverge together with the cutoff Λ_{eff}

$$\Lambda_{\text{eff}}(\Lambda \to \infty) = \frac{2}{|\theta_{ij} p_j|}. \tag{2.2.34}$$

Since the small momenta here effectively acts as a large momentum divergence, though its NC-inverse, this effect is known as the UV/IR mixing.

Interestingly, according to [9], there seems to be no UV/IR mixing on the fuzzy sphere. In this case, the relevant parts of planar and non-planar diagram cancel out leaving a well defined logarithmic UV divergence in the mass term

$$\delta m_{\text{ren}}^2(S_N^2) = \frac{\lambda}{8\pi} \sum_{J=0}^{N} \frac{2J+1}{J(J+1)+m^2} \sim \log N. \tag{2.2.35}$$

There is, however, an additional term in the effective action called an NC anomaly

$$-\frac{\lambda}{24\pi} \int \phi h(\widetilde{\Delta}) \phi, \tag{2.2.36}$$

where $\widetilde{\Delta}$ is a function of the Laplacian whose eigenfunctions are sphere harmonics

$$\widetilde{\Delta} Y_l^L = L Y_l^L, \tag{2.2.37}$$

and h is a harmonic number

$$h(L) = \sum_{k=1}^{L} \frac{1}{k}, \qquad h(0) = 0. \tag{2.2.38}$$

2.3 Grosse-Wulkenhaar's model

Due to UV/IR mixing, we cannot renormalize the $\lambda\phi_\star^4$ model. Grosse and Wulkenhaar proposed a solution to this problem by introducing an additional harmonic oscillator Ω-term [13, 14, 15]

$$S_{\text{GW}} = \int \mathrm{d}x^D \left(\frac{1}{2}\partial^\mu\phi \star \partial_\mu\phi + \frac{\Omega^2}{2}((\theta^{-1})_{\mu\rho}x^\rho\phi) \star ((\theta^{-1})^{\mu\sigma}x_\sigma\phi) + \right.$$

$$\left. + \frac{m^2}{2}\phi\star\phi + \frac{\lambda}{4!}\phi\star\phi\star\phi\star\phi \right), \quad (2.3.39)$$

or in a condensed form

$$S_{\text{GW}} = \int \frac{1}{2}(\partial\phi)^2 + \frac{\Omega^2}{2}((\theta^{-1}x)\phi)^2 + \frac{m^2}{2}\phi^2 + \frac{\lambda}{4!}\phi^4. \quad (2.3.40)$$

The added term solved the UV/IR mixing problem at zero momentum, possibly due to Langman-Szabo (LS) dual form of this action [12], which introduces a symmetry between large and small energy scales in the spirit of T-duality. The LS-dual term seems to counteract the IR divergence of the kinetic term in the action [57]. The GW renormalizability analysis in [13] is quite involved and conducted in the matrix base.

We will restrict ourselves to two-dimensional case since it is connected to the matrix model we studied. In $D = 2$ the model is superrenormalizable with the divergent part of the mass renormalization given by [60]

$$\delta m^2_{\text{ren}} = \frac{\lambda}{12\pi(1+\Omega^2)} \log\frac{\Lambda^2\theta}{\Omega}, \quad (2.3.41)$$

where Λ represents the renormalization momentum cutoff scale. Since Ω itself does not renormalize, it turns out that it is possible to redefine the $\lambda\phi_\star^4$ as a $\Omega \to 0$ limit of the series of these super-renormalizable models. Parameter Ω then serves as a series label [61], and it is chosen to satisfy

$$\frac{1-\Omega^2}{1+\Omega^2} = \sqrt{1 - \frac{1}{(1+\log(\Lambda/\Lambda_{\text{ren}}))^2}}, \quad (2.3.42)$$

that is

$$\Omega \sim \frac{1}{\log\Lambda}. \quad (2.3.43)$$

As one can see, in the equation (2.3.41), Ω can not be directly set to 0, reflecting the zero-momentum UV/IR divergence. The slowly decreasing Ω in (2.3.43) circumvents this problem and adds a sub-leading divergence to the mass renormalization.

As we already mentioned in the introduction, the GW harmonic oscillator has a nice geometrical interpretation. Namely, in [16], it is shown that the GW model is obtained in the large N limit from the model of a scalar field on $\mathfrak{h}^{\text{tr}}$

$$S_{\mathfrak{h}} = \int \sqrt{g} \left(\frac{1}{2}(\partial\phi)^2 - \frac{\xi}{2}R_{\mathfrak{h}}\phi^2 + \frac{m^2_{\mathfrak{h}}}{2}\phi^2 + \frac{\lambda_{\mathfrak{h}}}{4!}\phi^4 \right). \quad (2.3.44)$$

The oscillator Ω-term from (2.3.39) is here partially absorbed into the kinetic term. The rest is contained in the product of the curvature $R_{\mathfrak{h}}$ and the field. As a quick confirmation, we can see from (2.1.13) and (2.3.39) that both Ω-term and $R_{\mathfrak{h}}$ are quadratic in NC coordinates.

Chapter 3

Phase transition simulation

This chapter contains the results of the original research. It is partially based on [46]. We here introduce the simulated matrix model and discuss the details and performance of the used simulation algorithm.

3.1 Matrix model

The GW model (2.3.44) can be converted into a matrix model using the Weyl transform [41]:

$$\phi \longleftrightarrow \Phi, \qquad \int \longleftrightarrow \sqrt{\det 2\pi\theta}\,\mathrm{tr}\,. \tag{3.1.1}$$

We investigated its matrix regularization S_N

$$S_N = \mathrm{tr}\left(c_k \Phi \mathcal{K} \Phi - c_r R \Phi^2 - c_2 \Phi^2 + c_4 \Phi^4\right), \tag{3.1.2}$$

in which the field Φ is a $N \times N$ Hermitian matrix, $\mathcal{K}$ the kinetic operator

$$\mathcal{K}\Phi = [P_\alpha, [P_\alpha, \Phi]], \tag{3.1.3}$$

dependant on momenta P_α

$$P_1 = -Y, \qquad P_2 = X, \tag{3.1.4}$$

and R the curvature of $\mathfrak{h}^{\mathrm{tr}}$ space projected onto $Z = 0$ section

$$R = \mathcal{R}\,\mathbb{1} - 8\left(X^2 + Y^2\right), \qquad \mathcal{R} = \frac{15}{2}. \tag{3.1.5}$$

All originally dimensionful quantities are here expressed in units of μ. The minus sign in front of the mass term is chosen for convenience, so that positive c_2 parameterizes the relevant portion of the phase diagram, while positive c_4 ensures that S_N is bounded from below. They will be accompanied by the rescaled model parameters

$$\widetilde{c}_2 = \frac{c_2}{N}, \qquad \widetilde{c}_4 = \frac{c_4}{N}. \tag{3.1.6}$$

The parameters of the GW model and our matrix model are closely related, and their exact connection is given in Appendix A.

In order to construct the phase diagram of our model, we need to find thermodynamic observables (Figure 3.1):

- energy per degree of freedom

$$E = \frac{\langle S_N \rangle}{N^2}, \tag{3.1.7}$$

- kinetic energy per degree of freedom

$$E_k = \frac{\langle c_k \operatorname{tr} \Phi \mathcal{K} \Phi \rangle}{N^2}, \tag{3.1.8}$$

- heat capacity per degree of freedom

$$C = \frac{\operatorname{Var} S_N}{N^2}, \tag{3.1.9}$$

- magnetization per eigenvalue

$$M = \frac{\langle | \operatorname{tr} \Phi | \rangle}{N}, \tag{3.1.10}$$

- staggered magnetization per eigenvalue

$$M_{\pm} = \frac{\langle | \operatorname{tr}((\mathbb{1}_{N/2} \oplus (-\mathbb{1}_{N/2}))\Phi)| \rangle}{N}, \tag{3.1.11}$$

- magnetic susceptibility per eigenvalue

$$\chi = \frac{\operatorname{Var} |\operatorname{tr} \Phi|}{N}, \tag{3.1.12}$$

- staggered magnetic susceptibility per eigenvalue

$$\chi_{\pm} = \frac{\operatorname{Var} |\operatorname{tr}((\mathbb{1}_{N/2} \oplus (-\mathbb{1}_{N/2}))\Phi)|}{N}, \tag{3.1.13}$$

- Binder cumulant

$$U = 1 - \frac{\langle | \operatorname{tr} \Phi |^4 \rangle}{3 \langle | \operatorname{tr} \Phi |^2 \rangle^2}. \tag{3.1.14}$$

We also need to keep an eye on the distribution of eigenvalues and traces of the field. Expectation value $\langle \mathcal{O} \rangle$ and variance $\operatorname{Var} \mathcal{O}$ of the observable $\mathcal{O}$ are given by

$$\langle \mathcal{O} \rangle = \frac{\displaystyle\int \mathrm{d}\Phi \, \mathcal{O} \, e^{-S}}{\displaystyle\int \mathrm{d}\Phi \, e^{-S}}, \qquad \operatorname{Var} \mathcal{O} = \langle \mathcal{O}^2 \rangle - \langle \mathcal{O} \rangle^2. \tag{3.1.15}$$

We computed standard uncertainties $\Delta\mathcal{O}$ from decorrelated data at 68% confidence level.

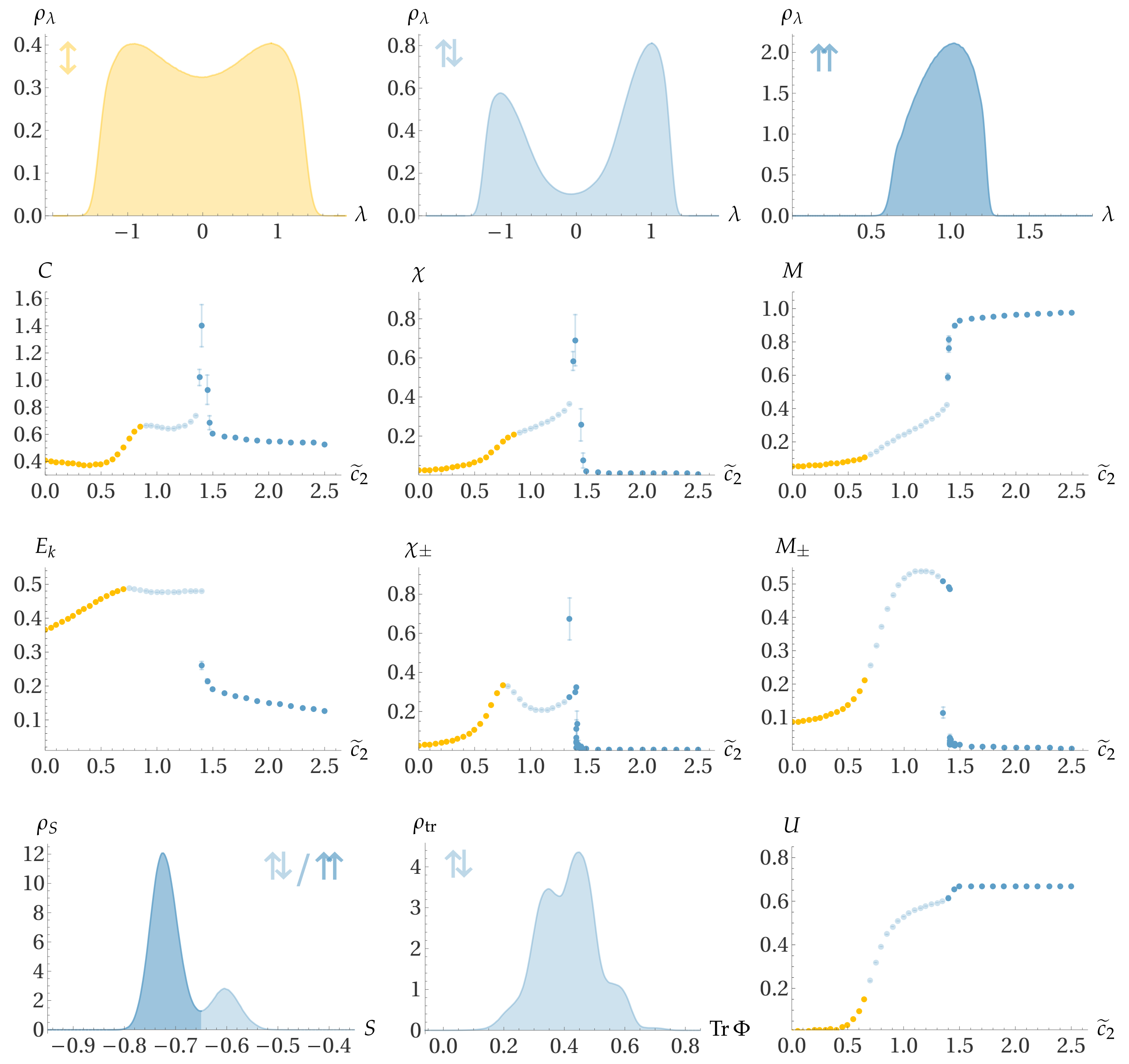

Figure 3.1: Example profiles of simulated thermodynamic observables for $N = 16$, $(c_k, c_r, \widetilde{c}_4) = (1, 0, 0.25)$, as functions of rescaled mass parameter $\widetilde{c}_2 = c_2/N$, with disordered phase colored in yellow/orange and ordered phases in different shades of blue. Transitions are driven by changes in shape of the eigenvalue distribution ρ_λ, as captured in the top row at $\widetilde{c}_2 = 0.5, 1.0, 2.0$ (left to right). We see two transitions as two peaks in C and matching (would-be-) peaks in χ. We also easily see $\updownarrow$ and $\uparrow\uparrow$ phases in plots of M and U, while the $\uparrow\downarrow$ phase is clearly visible in $M_\pm$, $\chi_\pm$, and in E_k. Energy distribution ρ_S in the bottom left figure lives at $\widetilde{c}_2 = 1.4$, near the border of two ordered phases, and represents two competing states with different energies, each belonging to one of the phases. A jump between those states causes a 1st order transition and prominent peaks in C and χ. The remaining shy peak in C signals a 3rd order transition and it is similar in shape to the well known 3rd order transition of the PP model shown in Figure 4.1. Finally, the center bottom figure lives at $\widetilde{c}_2 = 1.39$ and reveals $\uparrow\downarrow$ phase to be a mixture of different local minimum field configurations with different ratios of positive and negative eigenvalues. Magnetization and traces are expressed in units of $\sqrt{N \langle \mathrm{tr}\, \Phi^2 \rangle}$, eigenvalues in units of $\sqrt{\mathrm{tr}\, \Phi^2 / N}$, and S in units of $\widetilde{c}_2^2 / (4\widetilde{c}_4)$. Errorbars are mostly covered by data markers.

Let us note that just defined thermodynamic observables are intensive in matrix size. Factor $1/N$ counteracts the instances of trace, but it is not immediately obvious that we need to divide by N^2. At first glance, it seems counter-intuitive that variances have the same N dependence as the means since they explicitly include the squares of the means. However, if we introduce the temperature T as the inverse prefactor in the exponent of the path integral

$$E(T) = \frac{\displaystyle\int \mathrm{d}\Phi\, S\, e^{-S/T}}{\displaystyle\int \mathrm{d}\Phi\, e^{-S/T}}, \tag{3.1.16}$$

we can find the specific heat as

$$C(T) = \frac{\partial E(T)}{\partial T}. \tag{3.1.17}$$

Setting $T = 1$ recovers our initial definitions. Since the N dependence stems not from the temperature but from the action itself, we conclude that $E(T)$ and $C(T)$ must both be of the same order in N. The analogue argument holds for M and χ.

The Lebesgue measure for integration of Hermitian matrices Φ is defined as a product of differentials of all real degrees of freedom

$$\mathrm{d}\Phi = \prod_{i<j} \mathrm{d}\mathrm{Re}\,\Phi_{ij}\, \mathrm{d}\mathrm{Im}\,\Phi_{ij} \prod_{k} \mathrm{d}\Phi_{kk}. \tag{3.1.18}$$

Since a Hermitian matrix can be represented as a product of a diagonal matrix $\Lambda = \mathrm{diag}\,\lambda_i$ containing the real eigenvalues of Φ and a unitary matrix U (radial-angular decomposition), we can perform a change of variables in the path integral and write

$$\mathrm{d}\Phi = \mathrm{d}U \mathrm{d}\Lambda\, \Delta^2(\Lambda), \tag{3.1.19}$$

where the Vandermonde determinant $\Delta(\Lambda)$

$$\Delta(\Lambda) = \prod_{1\le i<j\le N} (\lambda_j - \lambda_i), \tag{3.1.20}$$

comes from the Jacobian of the transformation. When the action can be diagonalized using unitary transformation, we can integrate out the unitary degrees of freedom. This means that in the absence of kinetic and curvature terms, it is possible to simplify the integration over Hermitian matrices in (3.1.15), leaving only computationally much cheaper integration over eigenvalues. With kinetic term included, it is not possible to simultaneously diagonalize all four contributions, and we had to settle with working with relatively small matrix sizes in order to keep the simulation time manageable. Assuming

$$\langle \mathcal{O} \rangle = \lim_{N\to\infty} \langle \mathcal{O} \rangle_N, \qquad \langle \mathcal{O} \rangle_N = \langle \mathcal{O} \rangle \left(1 + \frac{\omega_1}{N} + \frac{\omega_2}{N^2} + \cdots \right), \tag{3.1.21}$$

observable estimate at a percent level precision would require $N \sim 100$. The largest matrix size we used was $N = 70$, so we have a reasonable confidence in the extrapolations from the collected simulation data.

Phase transitions in finite systems form smeared finite peaks and edges in profiles of free energy derivatives, as we can see in example data from our simulations in Figure 3.1.

Different quantities yield slightly different estimates of transition points, but they ultimately converge for large enough matrices. To locate them, we scanned through parameter space by varying c_2 at fixed c_4, which played a role of temperature, and searched for peaks in C and χ. We modeled peaks with a triangular distribution of width w and then took $w/(2\sqrt{6})$ as a measure of uncertainty of their position, which gives 65% confidence interval. The edges of the triangular distribution are taken to lie at least 2-3 standard errors below the best choice for the maximum, with at least two points in proper increasing/decreasing order on each side of the maximum.

Already the analysis of the classical action provides a clue about the structure of the phase diagram. The equation of motion reads

$$2c_k[P_\alpha,[P_\alpha,\Phi]] - c_r\{R,\Phi\} + \Phi\left(-2c_2 + 4c_4\Phi^2\right) = 0, \tag{3.1.22}$$

and its kinetic, curvature and pure potential parts are respectively solved by

$$\Phi = \frac{\operatorname{tr}\Phi}{N}\,\mathbb{1}, \qquad \Phi = \mathbb{0}, \qquad \Phi^2 = \begin{cases} \mathbb{0} & \text{for } c_2 \leq 0, \\ \dfrac{c_2\,\mathbb{1}}{2c_4} & \text{for } c_2 > 0. \end{cases} \tag{3.1.23}$$

Obviously, competition is at work between three types of vacua characteristic of three phases discovered in the related matrix models [41] and depicted in Figures 3.1, 3.2 and 3.3:

- disordered ↕-phase — dominant contributions come from oscillations around the trivial vacuum $\langle\Phi\rangle_{\updownarrow} = \mathbb{0}$,
- non-uniformly ordered ↕-phase (also: striped phase, matrix phase) — dominant contributions come from oscillations around $\langle\Phi\rangle_{\uparrow\downarrow} \propto U\,\mathbb{1}_\pm\,U^\dagger$, U being a unitary matrix and $\mathbb{1}_\pm$ non-trivial square roots of the identity matrix,
- uniformly ordered ↑↑-phase — dominant contributions come from oscillations around $\langle\Phi\rangle_{\uparrow\uparrow} \propto \mathbb{1}$.

The pure potential (PP) model, with only mass and quartic term, exhibits the ↕-phase for $c_2 < 0$ and a 3rd order phase transition between ↕ and ↑↓ phases for large enough $c_2 > 0$. When the kinetic term is turned on, the ↑↑-phase also appears. The ↑↓-phase is a matrix equivalent of the stripe phase. Large mass parameter lives in the ↑↑-phase, and large quartic coupling in the ↕-phase, with the ↑↓-phase nested in between. The phases meet at a triple point.

It turns out that the kinetic part of the action E_k and staggered magnetization/susceptibility are excellent indicators of the matrix phase. The P_α-commutators annihilate highly symmetric $\mathbb{0}$ and $\mathbb{1}$ vacuum states, while yielding non-zero contributions on $\mathbb{1}_\pm$.

The phases can also be characterized by the field's eigenvalue distribution (Appendix B). One-cut deformed Wigner semicircle distribution corresponds to the ↕-phase, two-cut distribution to the ↑↓ and one-cut asymmetric distribution to the ↑↑ phase. Since eigenvalues come from twin vacua connected by $\mathbb{Z}_2$-symmetry, for large enough matrices system gets stuck in one of them, and we see asymmetric ↑↓ and ↑↑ distributions as in Figure 3.1,

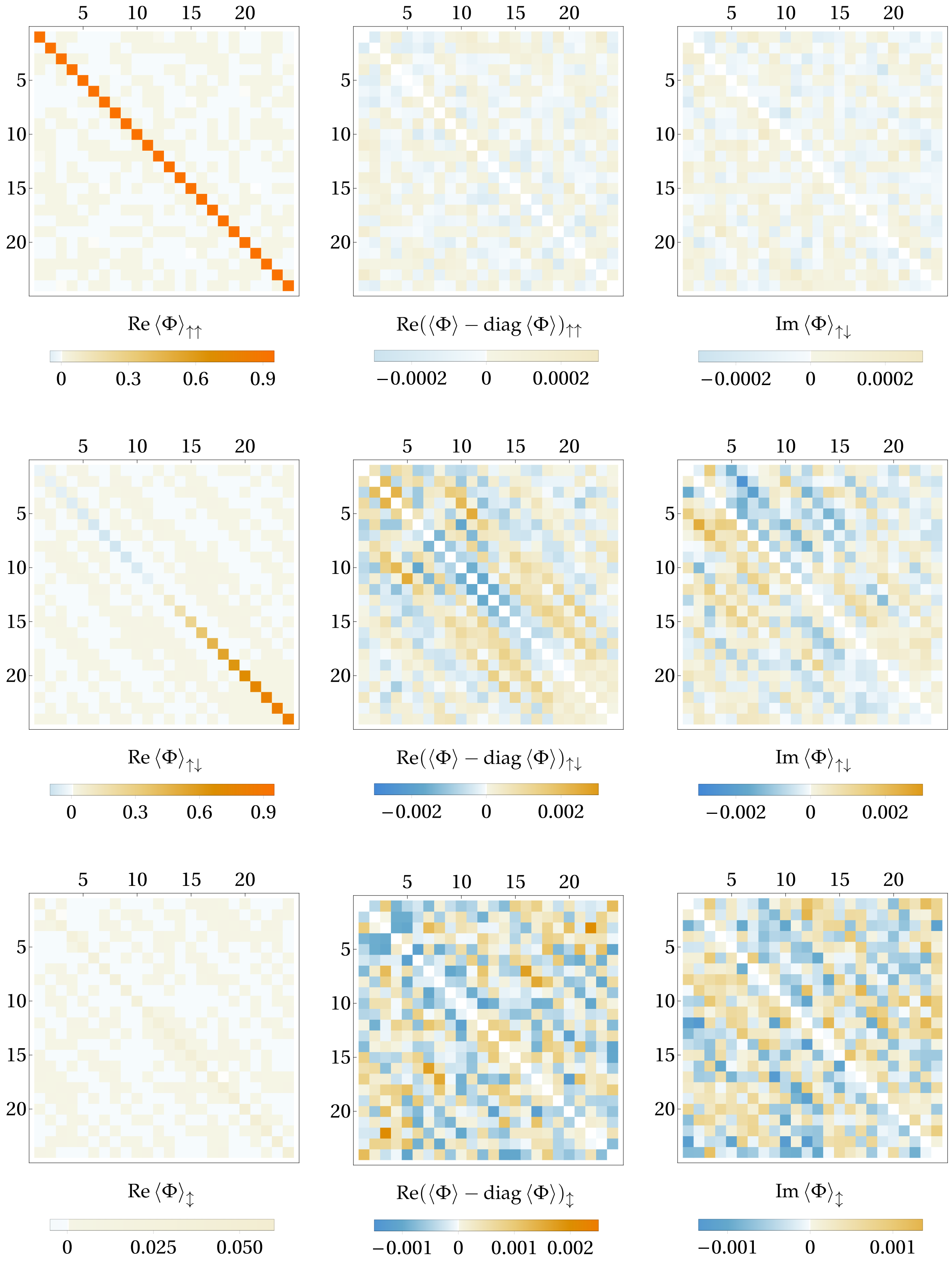

Figure 3.2: $\langle\Phi\rangle$ in three phases for $N = 24$ and $(c_r, \tilde{c}_4) = (0, 2)$. /TOP/ $\uparrow\uparrow$-phase at $\tilde{c}_2 = 7$. /MIDDLE/ $\uparrow\downarrow$-phase at $\tilde{c}_2 = 4$. /BOTTOM/ $\updownarrow$-phase at $\tilde{c}_2 = 1$. Re and Im parts of the matrix are separately shown. Averaging is performed over the $\mathrm{tr}\,\Phi > 0$ to extract one of the opposite-sign twin-vacua, however this procedure does not remove the sum over unitary rotations in the $\Phi_{\uparrow\downarrow}$ case.

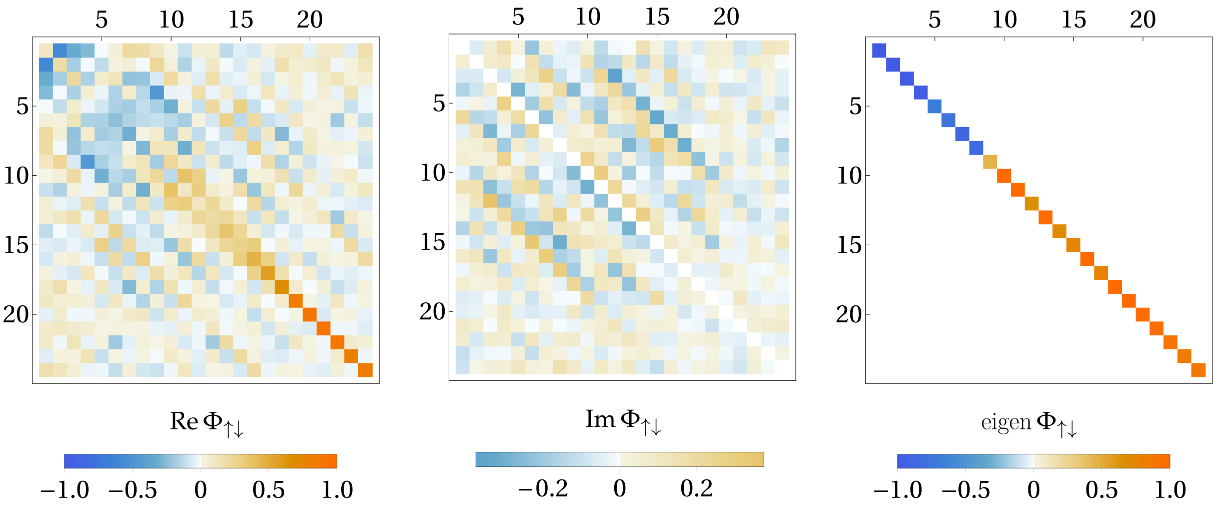

Figure 3.3: /left, middle/ Near most probable Φ configuration in the ↑↓-phase for $N = 24$ and $(\tilde{c}_4, \tilde{c}_2) = (2, 4)$. /right/ Schur decomposition of Φ into diagonal eigenvalue form, where the opposite-sign eigenvalues are now clearly visible.

accompanied by asymmetric trace distributions. Additionally, Binder cumulant changes sigmoidally with mass parameter, going from 0 in the ↕-phase to 2/3 in the ↑↑-phase, deviating into a valley in the ↑↓-phase (Figure 3.1).

For the inspected part of parameter space, the ↕→↑↓ transition is visible for $N \geq 16$ and the transition to ↑↑-phase is hard to access (similarly to [28]) for values of c_4 that allow all 3 phases to occur. The phase diagram anchoring is mostly done on the ↕→↑↑ transition line. More details about the transitions and also a discussion of transition order and critical exponents are provided in Appendix C.

Our analysis indicates a novel modification of ordered phases. Namely, when the kinetic term is negligible (e.g. field near $\propto \mathbb{1}$) and $c_2 \geq \max_i c_r |R_{ii}|$, a diagonal solution exists that combines the effects of the curvature and the potential and which deforms the vacuum of the ordered phases:

$$\Phi^2 = \frac{c_2\,\mathbb{1} + c_r R}{2c_4}. \tag{3.1.24}$$

A more detailed analysis of this configuration is left for Section 4.6.

Since we performed parallel hybrid Monte Carlo simulations to measure various thermodynamic observables, we will now discuss the used numerical method.

3.2 Hybrid Monte Carlo

In order to extract the information about the phase transitions, we must find how the expectation values of relevant observables vary as we change the parameters of the system. Monte Carlo method [62, 63, 64], in a nutshell, replaces the path integrals in expectation values by appropriate integral sums over a sufficiently large sample $\{\Phi_s\}$ of randomly generated matrix-field configurations. This turns the expectation values of the observables into

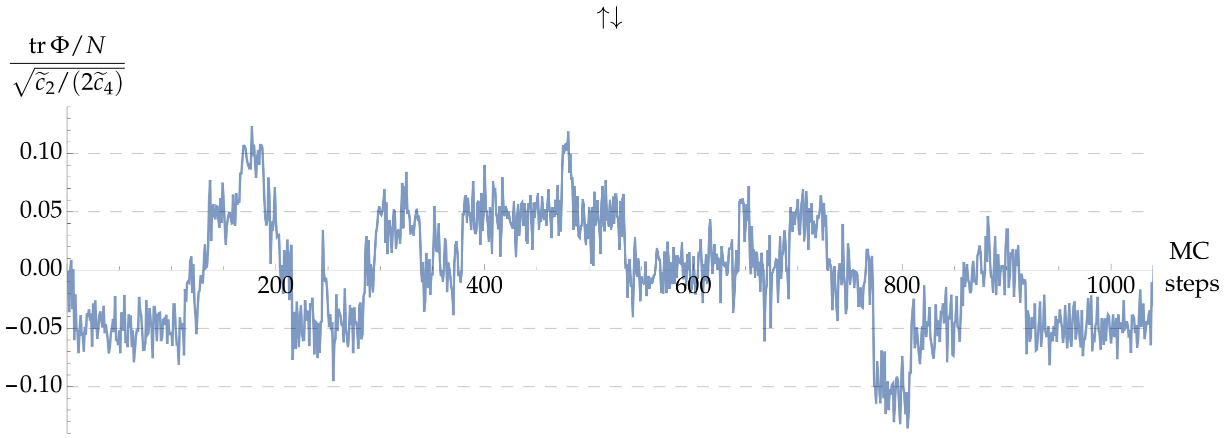

Figure 3.4: Simulation data history example for $N = 24$ at $(c_k, c_r, \tilde{c}_2, \tilde{c}_4) = (1, 0.2, 6, 3)$. We see transition between the false vacua indicated by dashed lines. Data is partially decorrelated with every 4th point shown.

averages over N_{MC} generated configurations

$$\langle \mathcal{O}(\Phi) \rangle \approx \frac{1}{N_{\mathrm{MC}}} \sum_{s=1}^{N_{\mathrm{MC}}} \mathcal{O}(\Phi_s). \tag{3.2.25}$$

We performed our simulation in C++ using *Eclipse IDE* loaded with *Armadillo* and *BLAS* libraries. Our code was also parallelized to work with *OpenMP*. The simulation is performed in 2^6 repeated copies run over 2^4 parallel threads. Each simulation gathered at least 2^{10} (somewhat) decorrelated MC steps. First derivatives of free energy and their uncertainties, as well as second derivatives, were obtained for each copy and then averaged over the copies. Second derivatives' uncertainties were gathered from the distribution of the copies of the simulation.

In order to speed up the generation of field configuration obeying the action-generated distribution $\exp(-S_N)$, we used the Hybrid Monte Carlo. The method consists of extending the system by introducing momentum Π^T conjugate to field Φ. In order to preserve ergodicity and phase volume element conservation Π is also a $N \times N$ Hermitian matrix. This way we can define a Hamiltonian for the extended system

$$H(\Phi, \Pi) = \frac{1}{2}\,\mathrm{tr}\,\Pi^2 + S_N(\Phi), \tag{3.2.26}$$

and generate field configurations by using Hamiltonian dynamics. Derivatives with respect to matrix elements of Φ and Π, which appear in the Hamilton equations

$$\frac{\mathrm{d}\Phi_{ij}}{\mathrm{d}t} \equiv \dot{\Phi}_{ij} = +\frac{\partial H}{\partial \Pi_{ji}}, \qquad \frac{\mathrm{d}\Pi_{ij}}{\mathrm{d}t} \equiv \dot{\Pi}_{ij} = -\frac{\partial H}{\partial \Phi_{ji}}, \tag{3.2.27}$$

are defined as

$$\frac{\partial \Phi_{i_1 j_1}}{\partial \Phi_{i_2 j_2}} = \delta_{i_1 i_2}\delta_{j_1 j_2}, \qquad \frac{\partial \Pi_{i_1 j_1}}{\partial \Pi_{i_2 j_2}} = \delta_{i_1 i_2}\delta_{j_1 j_2}, \tag{3.2.28}$$

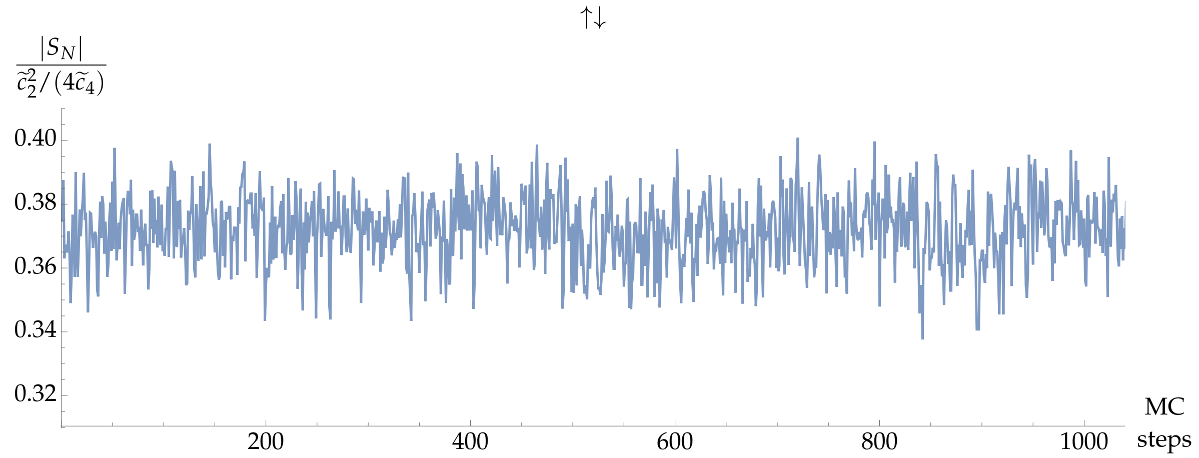

Figure 3.5: Simulation data history example for $N = 24$ at $(c_k, c_r, \tilde{c}_2, \tilde{c}_4) = (1, 0.2, 6, 3)$. Data is partially decorrelated with every 4th point shown.

and dot-derivative is with respect to Monte Carlo “time” t, which keeps track of steps in the simulation.

Momentum derivative of the added “momentum” term

$$\frac{\partial}{\partial \Pi_{ji}}\left(\frac{1}{2}\operatorname{tr}\Pi^2\right) = \Pi_{ij}, \tag{3.2.29}$$

gives the field’s time-evolution equation

$$\dot{\Phi} = \Pi. \tag{3.2.30}$$

Field derivative is somewhat more complicated due to a double commutator in the kinetic term of S_N:

$$\dot{\Pi} = 2c_k(P_\alpha \Phi P_\alpha - \{P_\alpha P_\alpha, \Phi\}) - 2c_r\{R, \Phi\} - 2c_2\Phi - 4c_4\Phi^3. \tag{3.2.31}$$

Equations (3.2.30) and (3.2.31) are then integrated using the Leapfrog integration that repeats the steps

$$\mathcal{I}_\Phi : (\Phi, \Pi) \to (\Phi + \dot{\Phi}\delta t, \Pi), \qquad \mathcal{I}_\Pi : (\Phi, \Pi) \to (\Phi, \Pi + \dot{\Pi}\delta t), \tag{3.2.32}$$

in the following order

$$\left(\mathcal{I}_\Phi({}^{\delta t}/2) \circ \mathcal{I}_\Pi(\delta t) \circ \mathcal{I}_\Phi({}^{\delta t}/2)\right)^{N_{\text{iter}}}, \tag{3.2.33}$$

where N_{iter} is the number of iterations between two accept/reject decisions. N_{iter} is chosen such that $N_{\text{iter}} \gtrsim 20$ and $N_{\text{iter}}\delta t = O(1)$. This chain of transformation leads from the old field configuration Φ_{old} to a proposed new field configuration Φ_{new} that might participate in the integral sum of the path integral.

At the end of a round of numerical integration, we perform the Metropolis test to chose whether to accept the proposed Φ_{new} field configuration or not. In order to generate the appropriate probability distribution given by

$$e^{-S_N}\mathrm{d}\Phi, \tag{3.2.34}$$

we first generate a random number r from a uniform distribution over the unit interval $r \in [0, 1]$. Then, r is compared with an energy weight ratio between the current and the new state

$$\frac{e^{-S_N(\Phi_{\text{new}})}}{e^{-S_N(\Phi_{\text{old}})}} = e^{-\Delta S_N} \tag{3.2.35}$$

and

- if $r < e^{-\Delta S_N}$, we accept the proposal,
- if $r > e^{-\Delta S_N}$, we keep the old field.

The procedure is set to guide the field towards more probable states with lower energy, since

$$\Delta S_N < 0 \quad \Rightarrow \quad e^{-\Delta S_N} > 1 > r, \tag{3.2.36}$$

in which case Φ_{new} is accepted with 100% probability. Examples of averaged and highly probable field configurations are shown in Figures 3.2 and 3.3.

We varied time step δt to achieve an optimal acceptance rate. The acceptance rate of 65% [65] is suitable for large matrices, but smaller matrices need higher values, even above 90%.

The validity of the algorithm was checked by numerical evaluation of the Schwinger-Dyson identity (SDI), and comparison to the expected theoretical value which is easy to find. Also, we repeated the results for the PP model, since it is well established in literature, both analytically and numerically. The SDI is derived from an integral over a full differential

$$\int \mathrm{d}\Phi \, \frac{\partial}{\partial \Phi_{ij}} \left(\Phi_{ij} \, e^{-S_N} \right) = 0. \tag{3.2.37}$$

It states that

$$\left\langle \mathrm{tr} \left(2c_k \Phi [P_\alpha, [P_\alpha, \Phi]] - 2c_r R \Phi^2 - 2c_2 \Phi^2 + 4c_4 \Phi^4 \right) \right\rangle = N^2, \tag{3.2.38}$$

or

$$2 \left\langle S_N^{(2)} \right\rangle + 4 \left\langle S_N^{(4)} \right\rangle = N^2, \tag{3.2.39}$$

where $S_N^{(i)}$ denotes the part of the action containing i^{th} powers of the field.

Systems with multiple false vacua tend to slowly switch between deep potential wells, causing problems with ergodicity and being stuck around the wrong potential minimum. One way to partially account for this is to start a simulation around the correct vacuum choice and then take its results as the best estimate of simulated observables (Appendix D). The true vacuum can be identified by having the lowest energy based on a short simulation run.

3.3 Autocorrelation

Since the generation of a new field proposal depends on the previous field configuration used in the simulation, we are to expect, to a lesser or greater extent, the autocorrelation between

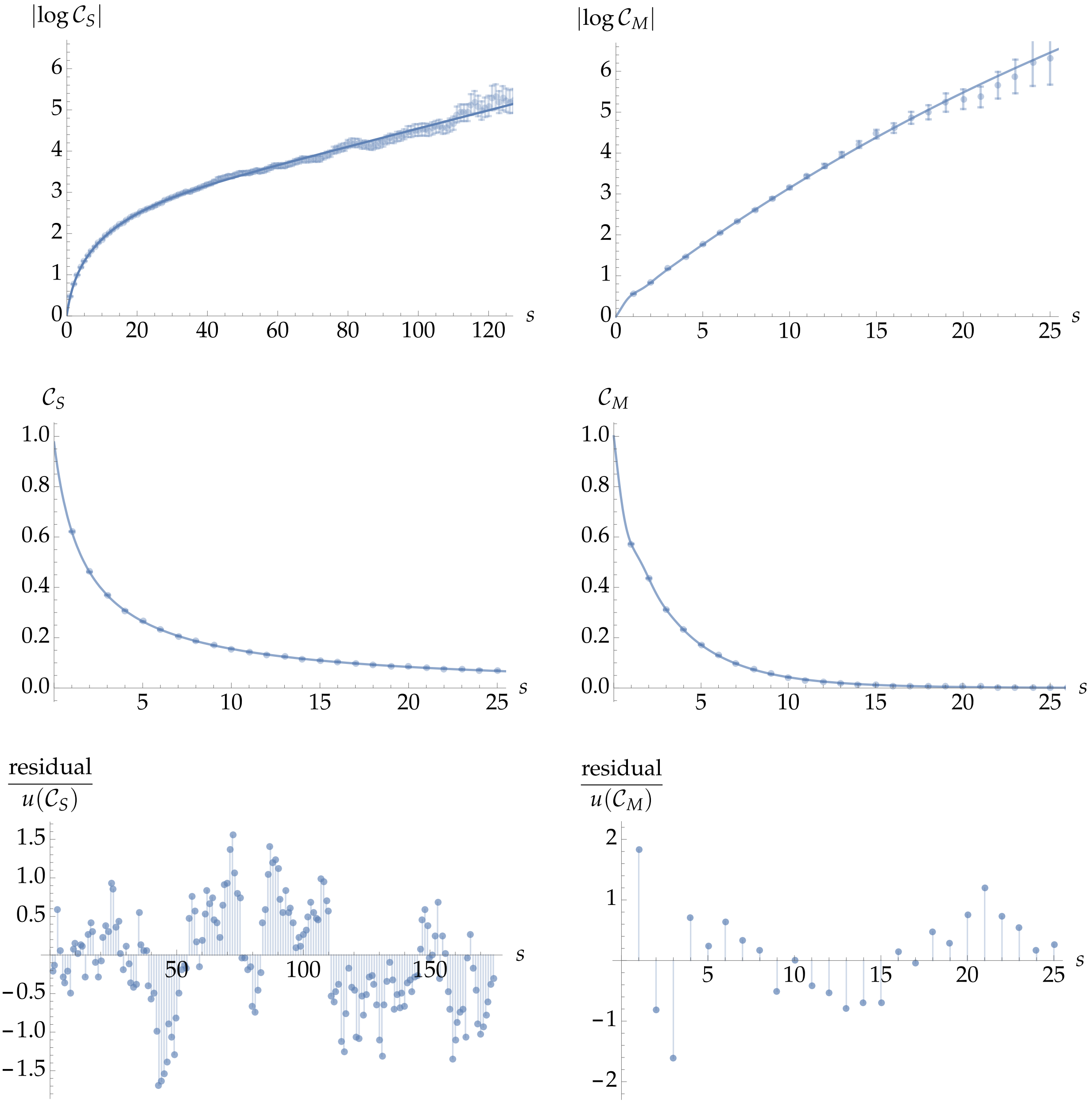

Figure 3.6: ACFs near the $\updownarrow \to \uparrow\uparrow$ transition line and their residuals. Data is gathered from susceptibility χ for $N = 24$ at $(c_k, c_r, \widetilde{c}_2, \widetilde{c}_4) = (1, 0, 0.04, 0.005)$.

those states. The autocorrelation poses a problem since it reduces an effective number of points over which the integral sum is performed, thus increasing the error in the assessed quantities. In extreme cases, it can lead to a quite biased sampling of the configuration space. Let us briefly discuss how we obtained decorrelated quantities necessary for the correct observable averaging.

The s-steps apart autocorrelation function $\mathcal{C}_{\mathcal{O}}(s)$ for the observable $\mathcal{O}$ generated in a Markov chain of the length N_{MC} is of the form

$$\mathcal{C}_{\mathcal{O}}(s) = \frac{1}{N_{\text{MC}} - s} \sum_{t=1}^{N_{\text{MC}}-s} \frac{(\mathcal{O}_t - \langle \mathcal{O} \rangle)(\mathcal{O}_{t+s} - \langle \mathcal{O} \rangle)}{\sigma_{\mathcal{O}}^2}, \tag{3.3.40}$$

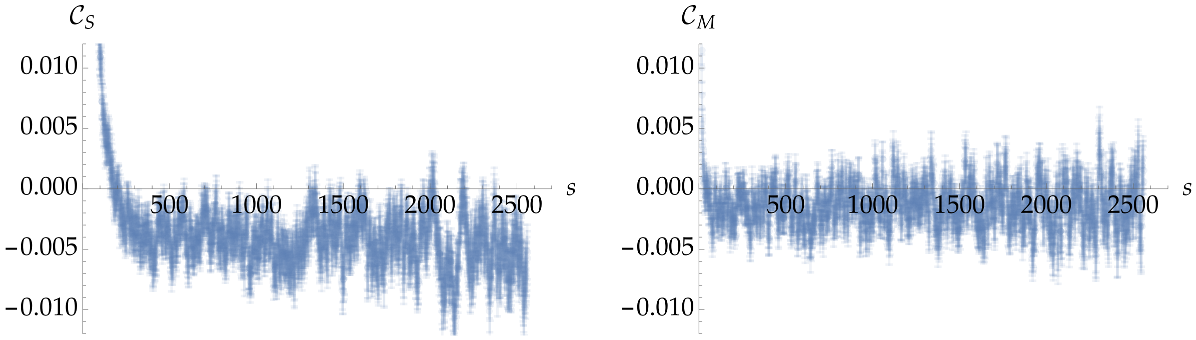

Figure 3.7: Large lag behaviour of ACFs near $\updownarrow \to \uparrow\uparrow$ transition line. Data gathered from susceptibility χ for $N = 24$ at $(c_k, c_r, \widetilde{c}_2, \widetilde{c}_4) = (1, 0, 0.04, 0.005)$.

where

$$\langle \mathcal{O} \rangle = \frac{1}{N_{\text{MC}}} \sum_{t=1}^{N_{\text{MC}}} \mathcal{O}_t, \qquad \sigma_{\mathcal{O}} = \sqrt{\frac{1}{N_{\text{MC}} - 1} \sum_{t=1}^{N_{\text{MC}}} (\mathcal{O}_t - \langle \mathcal{O} \rangle)^2}. \tag{3.3.41}$$

The function $\mathcal{C}_{\mathcal{O}}(s)$ generically drops like an exponential

$$\mathcal{C}_{\mathcal{O}}(s) \sim e^{-s/\tau_{\mathcal{O}}}, \tag{3.3.42}$$

$\tau_{\mathcal{O}}$ being the observable's $\mathcal{O}$ autocorrelation "time" (steps simultaneously measure the increase in simulation time). Each observable has its own, in principle different, autocorrelation time.

We pre-measured autocorrelation function for $N_{\text{MC}} = 2^{12}$ and found the effective $\tau_{\mathcal{O}}$ for each relevant observable as the time needed for a e-fold ACF decrease

$$\mathcal{C}_{\mathcal{O}}(\tau_{\mathcal{O}}) = \frac{1}{e}. \tag{3.3.43}$$

These times were maximized over measured observables and finally rounded up to the nearest power of 2 (since our data is organized in powers of 2) to obtain the combined effective AC time τ

$$\log_2 \tau = \left\lceil \log_2 \max_{\mathcal{O}} \tau_{\mathcal{O}} \right\rceil, \qquad \mathcal{O} \in \left\{ S, S^2, |\operatorname{tr}\Phi|, |\operatorname{tr}\Phi|^2 \right\}. \tag{3.3.44}$$

We then proceeded with at least $N_{\text{MC}} = 2^{10}\tau$ steps, taking each τ^{th} to decorrelate our data. In the critical slowdown region we limited $\tau \leq 2^5$, to make simulation times manageable.

An example of the simulated ACF is provided in Figures 3.6 and 3.7. The ACF is found by averaging 400 repeated runs of simulation. We found that ACF for S exhibits modified stretched exponential behaviour, similar to [66],

$$\mathcal{C} \sim \sum_i \frac{c_i e^{-(s/\tau_i)^{\lambda_i}}}{(1+s)^{\omega_i}}, \tag{3.3.45}$$

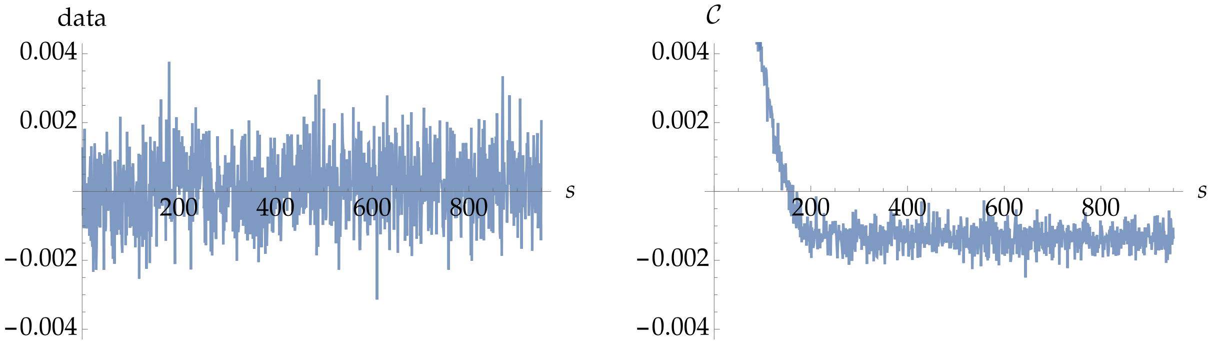

Figure 3.8: Large lag behaviour of hypothetical ACF. For $s \in [150, 850]$ the ACF is $\mathcal{C} = -0.00130(2)$.

with different coefficients for small and large lag:

$$\mathcal{C}_S = 0.88(2)e^{-s/10.0(9)}\frac{1+0.08(2)s}{1+0.62(4)s} + 0.096(4)e^{-s/45(1)}, \tag{3.3.46}$$

$$\mathcal{C}_M = 0.13(2)e^{-s/0.66(6)}\cos\pi s + 0.84(2)e^{-(s/2.81(4))^{0.92(2)}} + 0.038(4)e^{-s/7(1)}. \tag{3.3.47}$$

Such ACF are observed in glassy systems and spin glass.

In Figure 3.7 we can see an unexpected slightly negative average correlations at the large lag: $-0.00432(4)$ for S and $-0.00145(4)$ for M. Since the data are gathered near the transition line, we considered a possibility that this is caused by oscillations between two close states that are not well resolved in eigenvalue distributions, which resembles the two-state Markov mixture model [67].

Let us inspect what happens with ACF fit-residuals where multiple local minima of the potential are present. In the simplest case, the appropriate observables $\mathcal{O}$ would oscillate around the two values $\mathcal{O}_1$ and $\mathcal{O}_2$ about the same amount of time, occasionally jumping between them. Averages on the small time scales would be $\mathcal{O}_i$ but overall they would combine into $\langle\mathcal{O}\rangle = (\mathcal{O}_1 + \mathcal{O}_2)/2$. The correlator at the lag near the average time spent around the minima would therefore be

$$\left\langle(\mathcal{O}_i + \delta\mathcal{O}_i)(\mathcal{O}_j + \delta\mathcal{O}_j)\right\rangle = \mathcal{O}_i\mathcal{O}_j + \mathcal{O}_{\{i}\left\langle\delta\mathcal{O}_{j\}}\right\rangle + \left\langle\delta\mathcal{O}_i\delta\mathcal{O}_j\right\rangle \approx \mathcal{O}_i\mathcal{O}_j, \tag{3.3.48}$$

which differs from the average value by

$$(\langle\mathcal{O}\rangle \pm \Delta\mathcal{O})(\langle\mathcal{O}\rangle \mp \Delta\mathcal{O}) - \langle\mathcal{O}\rangle^2 = -\Delta^2\mathcal{O}, \tag{3.3.49a}$$

$$\Delta\mathcal{O} = \frac{|\mathcal{O}_1 - \mathcal{O}_2|}{2}. \tag{3.3.49b}$$

This would result in a negative AC coefficient starting with that lag, until reverting to oscillations around the starting state. Different time spent in each state would modify the shape of the ACF.

We tested this hypothesis on the following model. We generated normally distributed data with standard deviation 1 around two close states $\mathcal{O}_1 = -0.02$ and $\mathcal{O}_2 = +0.02$. We assumed that the $\mathcal{O}_1$ has the lower energy and that the average time spent in this state is

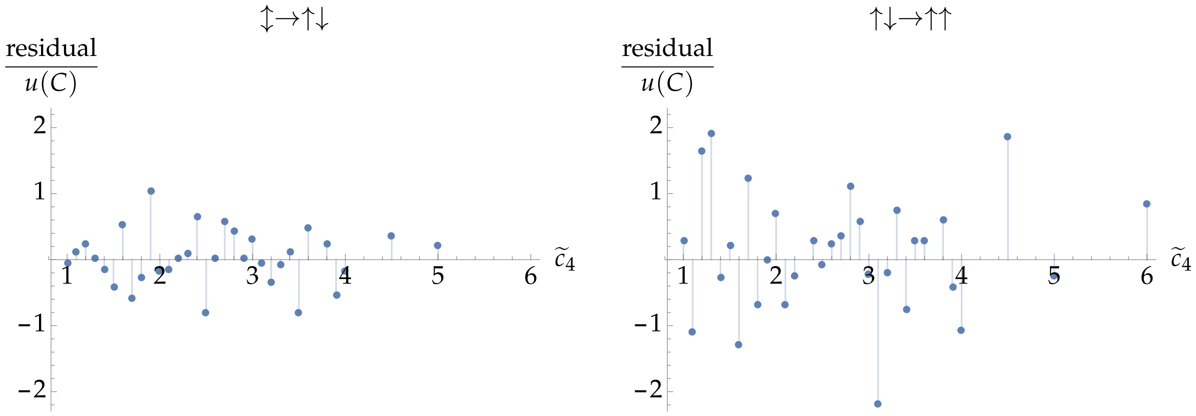

Figure 3.9: Standardized residuals of the phase transition line fits $\widetilde{c}_2 = f(\widetilde{c}_4)$. Data gathered from C for $N = 24$ at $(c_k, c_r) = (1, 0)$.

thus greater than the average time spent around $\mathcal{O}_2$. Starting from the higher energy state, we alternated between these states so that time spent around $\mathcal{O}_1$ was randomly chosen from the interval $[1000, 2000]$, and the time spent around $\mathcal{O}_2$ randomly chosen from $[100, 200]$. The ACF for this data in Figure 3.8 is negative at the shown large lag interval and correctly reproduces the characteristics of the simulation ACF.

Let us finally see how the data behaved in different phases and consider the influence of the autocorrelation on transition line fits.

For the fixed N_{MC} and time step, the uncertainty of C and χ grew larger with entering the (partly-)ordered phase. Our intuition is that this is not due to autocorrelation but due to ergodic problems, namely with simulation being trapped around a local minimum for a prolonged time, thus being unable to produce a stable eigenvalue distribution in a short time and to scan the configuration space of the field properly.

It can be seen that residuals for the $\uparrow\downarrow \to \uparrow\uparrow$ transition line fit are spread about two times wider than expected from normally distributed random error (Figure 3.9). This indicates that we underestimated our error and that the systematic error is probably significant (but at least partly canceled since we have a dispersion of the error around zero). Unfortunately, this can only be resolved by increasing the run time of the simulation. For example, the $N = 4$ model with $(c_k, c_r, \widetilde{c}_2, \widetilde{c}_4) = (1, 0, 11, 5)$, needed 2^{24} decorrelated steps (2^{26} in total) to reach a fairly symmetric distribution of traces and visit all the false vacua. Since the number of possible false vacua increases at least linearly with N, we expect the step estimate to rise to at least $O(2^{22}N)$ and possibly exponentially with N. Having in mind the naive estimate of matrix multiplication time $O(N^3)$, stemming from one sum for each of N^2 matrix entries

$$(AB)_{ij} = \sum_{k=1}^{N} A_{ik} B_{kj}, \tag{3.3.50}$$

the simulation time estimate becomes at least $O(2^{24}N^4)$. A novel approach to the problem of simulation being stuck in a false vacuum, based on the eigenvalue flipping, is presented in [68] and could perhaps dramatically reduce the required simulation times.

Chapter 4

Submodels and phase diagrams

This chapter contains the results of the original research. It is chiefly based and draws heavily on [46, 69].

We here analyze the scaling of our model term by term and construct the phase diagrams. For more details on matrix models see [70].

4.1 Parameter scaling

Phase diagram of family of models $S_N(c_k, c_r, c_2, c_4; \Phi)$ is expected to converge to a well-defined non-trivial large N limit only if we properly choose the scaling of the models' parameters. Additionally, the scaling allows us to zoom in on the characteristic features of the diagram as we increase the matrix size. The wrong choice of scaling would, instead of large N stabilization, cause the drifting of transition points either towards zero or infinite values in the parameter space. This fact can be used to identify the correct choice of scaling. It turns out, however, that discriminating between choices based on data is not trivial.

According to [53], the partition function of the Hermitian Gaussian matrix model, which contains only the mass term, is

$$Z_{\text{Gauß}}(c_2) = \int\limits_{H(N)} \mathrm{d}\Phi\, e^{-c_2 N \operatorname{tr} \Phi^2} = 2^{N/2} \left(\frac{\pi}{2c_2} \right)^{N^2/2}. \tag{4.1.1}$$

We easily find that

$$\langle S_{\text{Gauß}} \rangle = -\frac{c_2}{Z_{\text{Gauß}}} \frac{\partial Z_{\text{Gauß}}}{\partial c_2} = \frac{N^2}{2}, \tag{4.1.2}$$

which is proportional to the number of real degrees of freedom (DOF) of the Hermitian field Φ, which is N^2. This can also be seen from the SDI (3.2.39) if we turn off the kinetic term and interaction. To keep the action extensive in number of DOF, we can ask that all of the terms in S_N be $O(N^2)$. This choice also assures a comparable contribution of the action terms, and presumably preserves a maximum amount of interesting details in the phase diagram of the model.

We will denote the scaling of a quantity q with ν_q so that

$$q = \widetilde{q} N^{\nu_q},$$

where $\nu_S = 2$ stands for the scaling of the action, ν_Φ for the field/its eigenvalues, $\nu_P = 1/2$ for the momenta, $\nu_R = 1$ for the curvature and ν_k, ν_r, ν_2, ν_4 for the coefficients in front of the kinetic, curvature, mass and quartic term respectively.

Requiring each term in the action to behave as $O(N^2)$ and noting that tr increases powers by 1, leads, by power counting, to a system of equations

$$\nu_S = \nu_k + 2\nu_P + 2\nu_\Phi + 1 \tag{4.1.3a}$$
$$\nu_S = \nu_r + \nu_R + 2\nu_\Phi + 1 \tag{4.1.3b}$$
$$\nu_S = \nu_2 + 2\nu_\Phi + 1 \tag{4.1.3c}$$
$$\nu_S = \nu_4 + 4\nu_\Phi + 1 \tag{4.1.3d}$$

solved by

$$\nu_4 = 2\nu_2 - 1, \qquad \nu_r = \nu_2 - \nu_R, \qquad \nu_k = \nu_2 - 2\nu_P, \qquad 2\nu_\Phi = 1 - \nu_2. \tag{4.1.4}$$

For values of ν_2 and ν_4 used in the PP model and on the fuzzy sphere, this amounts to

$$\nu_2 = 3/2, \quad \nu_4 = 2, \quad \nu_r = 1/2, \quad \nu_k = 1/2, \quad \nu_\Phi = -1/4. \tag{4.1.5}$$

We wish to examine a simpler choice:

$$\nu_2 = 1, \quad \nu_4 = 1, \quad \nu_r = 0, \quad \nu_k = 0, \quad \nu_\Phi = 0. \tag{4.1.6}$$

Notice that parameters' original mass dimensions were

$$[c_2] = [c_4] = 2, \qquad [c_r] = 0; \tag{4.1.7}$$

therefore, (4.1.6) causes both c_2 and c_4 to scale the same way with the momentum cutoff $\Lambda \sim \sqrt{N}\mu$, whereas c_r does not scale at all. We will also, without loss of generality, set $\widetilde{c}_k = 1$ and proceed with the action

$$S_{\text{K+R+PP}}(N, \widetilde{c}_2, \widetilde{c}_4, \widetilde{c}_r) = N \operatorname{tr}\left(\Phi\widetilde{\mathcal{K}}\Phi - \widetilde{c}_r\widetilde{R}\Phi^2 - \widetilde{c}_2\Phi^2 + \widetilde{c}_4\Phi^4\right), \tag{4.1.8}$$

keeping the rescaled parameters $\widetilde{c}_2$, $\widetilde{c}_4$, $\widetilde{c}_r$ fixed while we increase the matrix size. K stands for the kinetic term, R for the curvature term and PP for the pure potential term.

We actually wish to simultaneously inspect two finite limits of our matrix model, which zoom-in on different portions of the parameter space:

$$\mathcal{S}(c_2, c_4, c_r) = \lim_{N\to\infty} \frac{\langle S_N(c_2, c_4, c_r)\rangle}{N^2}, \tag{4.1.9a}$$
$$\widetilde{\mathcal{S}}(\widetilde{c}_2, \widetilde{c}_4, c_r) = \lim_{N\to\infty} \frac{\langle S_N(\widetilde{c}_2, \widetilde{c}_4, c_r)\rangle}{N^2}. \tag{4.1.9b}$$

In a way, phase diagram of $\widetilde{\mathcal{S}}$ describes the structure of the infinity of the phase diagram of

$\mathcal{S}$. $\mathcal{S}_0$ and $\widetilde{\mathcal{S}}_0$ will refer to $c_r = 0$. We analyze $\mathcal{S}$ because it closely relates to S_{GW} up to a light adjustment of coefficients (Appendix A), while $\widetilde{\mathcal{S}}$ tells us about the scaling properties of the 3rd order ↕→↑↓ transition line.

We will first look at the PP term and then see how the kinetic and the curvature terms behave against this well-established background.

4.2 Potential term scaling

The PP model

$$S_{\mathrm{PP}} = N \operatorname{tr}\left(-\widetilde{c}_2\Phi^2 + \widetilde{c}_4\Phi^4\right) \tag{4.2.10}$$

is well studied both analytically and numerically [71, 72], so it can provide a basic calibration of the method. As it can be seen in Figure 4.1, it features a 3rd order transition from ↕ to ↑↓ phase in the large N limit at

$$\widetilde{c}_2 = 2\sqrt{\widetilde{c}_4} \qquad \Leftrightarrow \qquad c_2 = 2\sqrt{Nc_4}, \tag{4.2.11}$$

with a sharp-edged kink in specific heat. Both C and χ remain finite and continuous across the transition. At the transition point, C reaches the value 1/4 and remains constant for larger $\widetilde{c}_2$.

To confirm the transition order, let us look at the exact formula for C found in [72]:

$$C = \begin{cases} \dfrac{1}{4} + \dfrac{\widetilde{c}_2^4 + \widetilde{c}_2(\widetilde{c}_2^2 - 6\widetilde{c}_4)\sqrt{\widetilde{c}_2^2 + 12\widetilde{c}_4}}{216\widetilde{c}_4^2} & \text{for } \widetilde{c}_2 < 2\sqrt{\widetilde{c}_4}, \\[2ex] \dfrac{1}{4} & \text{for } \widetilde{c}_2 \geq 2\sqrt{\widetilde{c}_4}. \end{cases} \tag{4.2.12}$$

For $\widetilde{c}_2 < 2\sqrt{\widetilde{c}_4}$, the derivatives of C are given by

$$\frac{\partial C}{\partial \widetilde{c}_2} = \frac{\widetilde{c}_2^4 + \widetilde{c}_2^3\sqrt{\widetilde{c}_2^2 + 12\widetilde{c}_4} + 6\widetilde{c}_2^2\widetilde{c}_4 - 18\widetilde{c}_4^2}{54\widetilde{c}_4^2\sqrt{\widetilde{c}_2^2 + 12\widetilde{c}_4}}, \qquad \frac{\partial C}{\partial \widetilde{c}_4} = -\frac{\widetilde{c}_2}{2\widetilde{c}_4}\frac{\partial C}{\partial \widetilde{c}_2}. \tag{4.2.13}$$

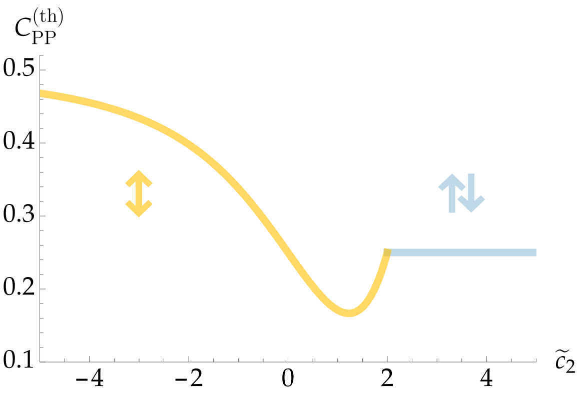

Figure 4.1: Specific heat in the infinite matrix limit of the PP model with $\widetilde{c}_4 = 1$. Derivative of the specific heat has a discontinuity at $\widetilde{c}_2 = 2\sqrt{\widetilde{c}_4} = 2$, where a 3rd order ↕→↑↓ transition occurs. The plateau in the striped phase lies at the value $C = 1/4$.

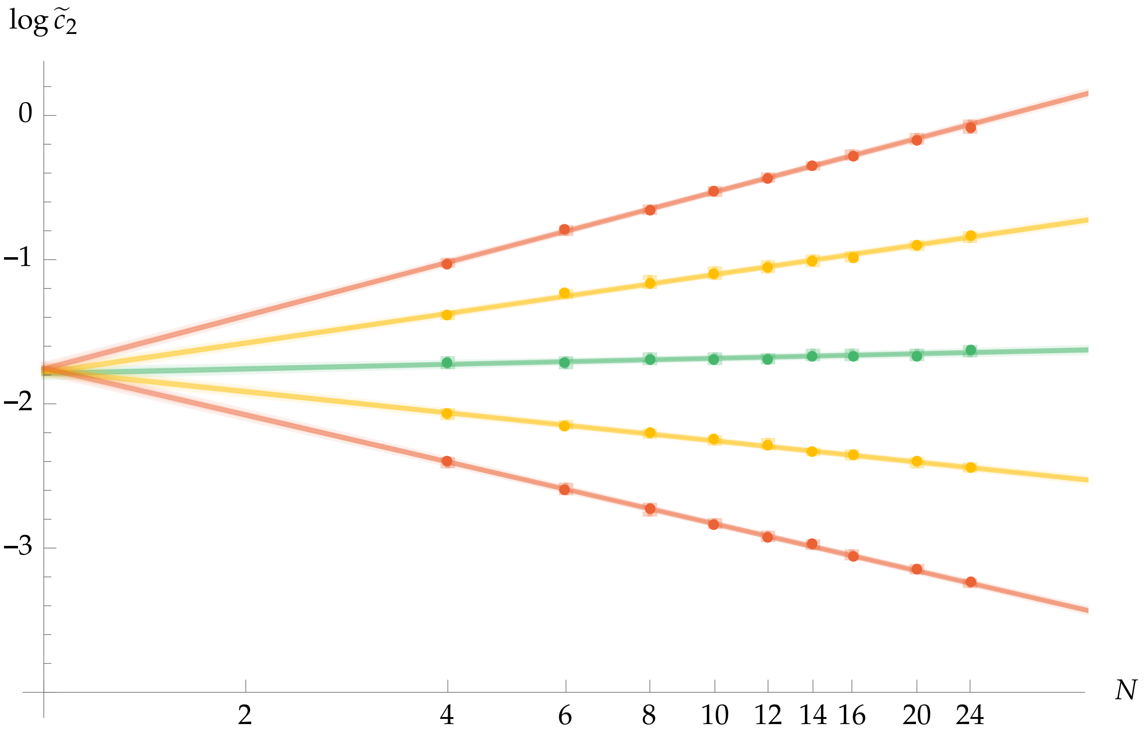

Figure 4.2: ↕→↑↓ transition in the PP model for $\widetilde{c}_4 = 0.01$, $4 \leq N \leq 24$ and fixed $\nu_2 = 1$, observed as peaks in χ. The green/center data represents the desired choice of scaling $\nu_4 = \nu_2 = 1$, the orange/inner sloped lines represent $\Delta\nu_4 = \pm 0.5$ and the red/outer sloped lines represent $\Delta\nu_4 = \pm 1$. Pale-coloured stripes are the 68% confidence intervals. Errorbars are mostly covered by data markers.

At the transition point they become

$$\frac{\partial C}{\partial \widetilde{c}_2} = \frac{1}{4\sqrt{\widetilde{c}_4}}, \qquad \frac{\partial C}{\partial \widetilde{c}_4} = -\frac{1}{4\widetilde{c}_4}, \tag{4.2.14}$$

and then both jump to 0, so the transition is clearly the 3rd order. More details about the derivation of the expressions for C are given in the Appendix B.

For an arbitrary choice of scaling, the transition line equation (4.2.11) translates to

$$\widetilde{c}_2 = 2\sqrt{\widetilde{c}_4 N^{1+\nu_4-2\nu_2}}. \tag{4.2.15}$$

Since for the desired scaling ν_i^* phase transition occurs at $\widetilde{c}_2$ and $\widetilde{c}_4$ which do not depend on N, it must hold

$$1 + \nu_4^* - 2\nu_2^* = 0. \tag{4.2.16}$$

Our choice from the previous section satisfies this equality. Subtracting this 0 from the exponent in (4.2.15), we get

$$\widetilde{c}_2 = 2\sqrt{\widetilde{c}_4 N^{\Delta\nu_4-2\Delta\nu_2}}, \tag{4.2.17}$$

where Δ marks the deviation from the desired scaling. The slope of the logarithmic plot of the transition line equation

$$\log \widetilde{c}_2 = \frac{\Delta\nu_4 - 2\Delta\nu_2}{2}\log N + \frac{\log 4\widetilde{c}_4}{2} \tag{4.2.18}$$

Table 4.1: $\log \widetilde{c}_2$ vs. $\log N$ linear fits for χ-transitions for $\widetilde{c}_4 = 0.01$, $\nu_2 = 1$ and various ν_4. Differences between expected and measured values are due to finite-size effects.

ν_4	intercept		slope	
	expected	measured	expected	measured
0.0		$-1.75(4)$	-0.50	$-0.47(2)$
0.5		$-1.77(4)$	-0.25	$-0.21(2)$
1.0	-1.61	$-1.79(4)$	0.00	$+0.05(2)$
1.5		$-1.78(3)$	$+0.25$	$+0.30(2)$
2.0		$-1.76(4)$	$+0.50$	$+0.53(2)$

is therefore changed from zero (up to $O(1/N)$ effects) to $\Delta\nu_4/2 - \Delta\nu_2$, and Figure 4.2 and Table 4.1 show how it is affected by different choices of scaling. Both $(\nu_2, \nu_4) = (3/2, 2)$ and $(\nu_2, \nu_4) = (1, 1)$ lead to the correct zero slope and therefore to matrix size independent phase diagram.

That both peak positions of χ and C converge to the same value is demonstrated for $\widetilde{c}_4 = 0.01$, where the large N limit of the transition $\widetilde{c}_2$ gives respective values $0.201(8)$ and $0.215(7)$; the theoretical value is 0.2.

There is a slight systematic difference (+0.04 on average) between measured and theoretical slopes in Table 4.1. It can be explained as a finite-size effect, that disappears for large enough matrices. Namely, since the equation (4.2.11) is based on the infinite matrix limit, we could account for the finite matrix size by using a perturbative ansatz

$$\widetilde{c}_2 = 2\sqrt{\widetilde{c}_4 \left(1 + \frac{\delta}{\sqrt{N}} + \cdots\right)}, \tag{4.2.19}$$

which modifies (4.2.18) into

$$\log \widetilde{c}_2 = \frac{\Delta\nu_4 - 2\Delta\nu_2}{2} \log N + \frac{\log 4\widetilde{c}_4}{2} + \frac{\delta}{2\sqrt{N}}. \tag{4.2.20}$$

The modified plot is indiscernible from the linear one on the data points, but the intercept and the slope of $\log \widetilde{c}_2 - \delta/(2\sqrt{N})$ are perfectly aligned with the theoretical value.

The results in this section justify the assumption that both conventional and tested choices of scaling are valid and that there are, in fact, infinitely many possible ones. A similar but more nuanced strategy was applied to the curvature term in Section 4.4 confirming the chosen parameter scalings.

4.3 Kinetic term scaling

Let us now turn on the kinetic term on top of the PP model and consider $S_{\text{K+PP}}$. As far as transitions go, the action with $(\widetilde{c}_k N^{\Delta\nu_k}, \widetilde{c}_2, \widetilde{c}_4)$ is equivalent, via absorption of $N^{\Delta\nu_k}$ into the field, to the one with $(\widetilde{c}_k, \widetilde{c}_2 N^{-\Delta\nu_k}, \widetilde{c}_4 N^{-2\Delta\nu_k})$. As a result, the wrong choice of scaling would force the transition points to drift towards zero or infinity. However, due to the lack of analytical prediction for the transition line, the exact rate of this drift is unknown.

To complicate the situation further, discrimination of different scalings based on the data is not clear-cut. For example, although Figure 4.3 shows a convincing large N convergence, looking at the transition plots for $\nu_k = 0$ and $\nu_k = 0.5$ in Figure 4.4, it is not immediately clear which represents the correct choice. At first glance, the wrong choice $\nu_k = 0.5$ appears to converge to a non-trivial finite value instead of zero, and the correct choice $\nu_k = 0$ to ever increase, possibly towards infinity. One reason for this could be the convergence of the position of the triple point with increasing N closer to the origin — the effect demonstrated in [45]. The system with fixed $\widetilde{c}_4$ would thus change from the 2-phase to the 3-phase regime as N increases, as in the top plot in Figure 4.4.

The other explanation could be the anomalous negative scaling of the kinetic term, causing the shift towards infinity. Unfortunately, using our data makes it impossible to rule out the second option and fix the scaling to precision less than ± 0.5, as this would require inspecting much larger matrices. However, we can strengthen the case for the choice $\nu_k = 0$.

Firstly, the top plot in Figure 4.4 allows finite near-linear extrapolation for $1/N \to 0$ (in green and blue). Secondly, the change from the 2-phase to the 3-phase regime for smaller examined $\widetilde{c}_4$ happens at larger N, which is consistent with the triple point converging towards smaller $\widetilde{c}_4$. Thirdly, as we will see, extrapolation of the data for $N < 16$ (in red and orange) converges to a value consistent with a stable linear transition line passing through other smaller values of $\widetilde{c}_4$. This line would also have passed through $\widetilde{c}_4 = 0.01$ at this extrapolated value of $\widetilde{c}_2$, had the system not entered the 3-phase regime with increasing N.

The model on the fuzzy sphere [45] exhibits linear $\updownarrow\to\uparrow\uparrow$ transition line in the large N limit:

$$\widetilde{c}_2 \propto \widetilde{c}_4. \tag{4.3.21}$$

In comparison, in our model, transition for $\nu_k = 0$ and fixed N appears to follow the empirical law

$$\widetilde{c}_2 = a(N)\sqrt{\widetilde{c}_4} + b(N)\,\widetilde{c}_4, \tag{4.3.22}$$

where $a(N)$ decreases for larger matrices (Figure 4.5). The coefficients $a(N)$ and $b(N)$ remain stable when higher power of $\widetilde{c}_4$ is added, while the uncertainty makes the additional term indistinguishable from zero. Perhaps the RG approach [49, 50, 73] could replicate this form of the transition line.

Let us here present a heuristic argument for (4.3.22). We will first consider the PP model where the kinetic term is absent. Suppose we travel along the transition line following the maximum of C, starting at $(\widetilde{c}_2, \widetilde{c}_4)$ and arriving at $(\widetilde{c}_2{}', \widetilde{c}_4{}')$. If $\widetilde{c}_2$ increased κ-times

$$\widetilde{c}_2{}' = \kappa \widetilde{c}_2, \tag{4.3.23}$$

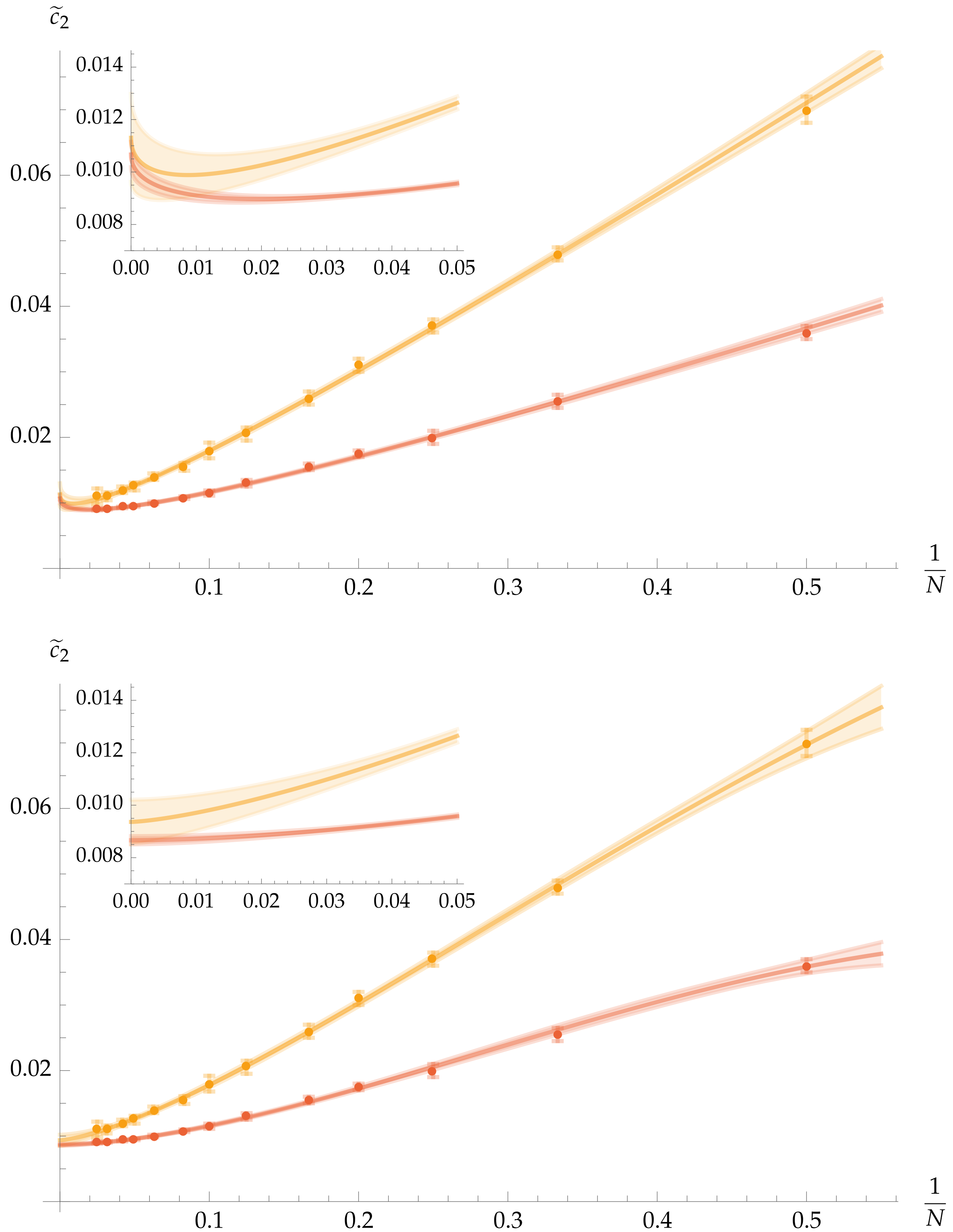

Figure 4.3: Two fits of the ↕→↑↑ transition for $\widetilde{c}_4 = 0.001$, $\nu_k = 0$ and $N \leq 40$, observed as peaks in C (orange/top) and χ (red/bottom). Pale-coloured stripes represent the 68% confidence intervals. The large N limit is zoomed-in. /TOP/ Square-root series fit: $\widetilde{c}_{2,C} = 0.011(2) - 0.3(1)\sqrt{N} + 0.16(2)N$ and $\widetilde{c}_{2,\chi} = 0.0112(5) - 0.024(4)\sqrt{N} + 0.086(6)N$. /BOTTOM/ Modified power-law fit: $\widetilde{c}_{2,C} = 0.0094(9) + 0.23(8)(1 - 0.6(4)/N)/N^{1.4(2)}$ and $\widetilde{c}_{2,\chi} = 0.0087(2) + 0.17(6)(1 - 0.9(3)/N)/N^{1.7(2)}$.

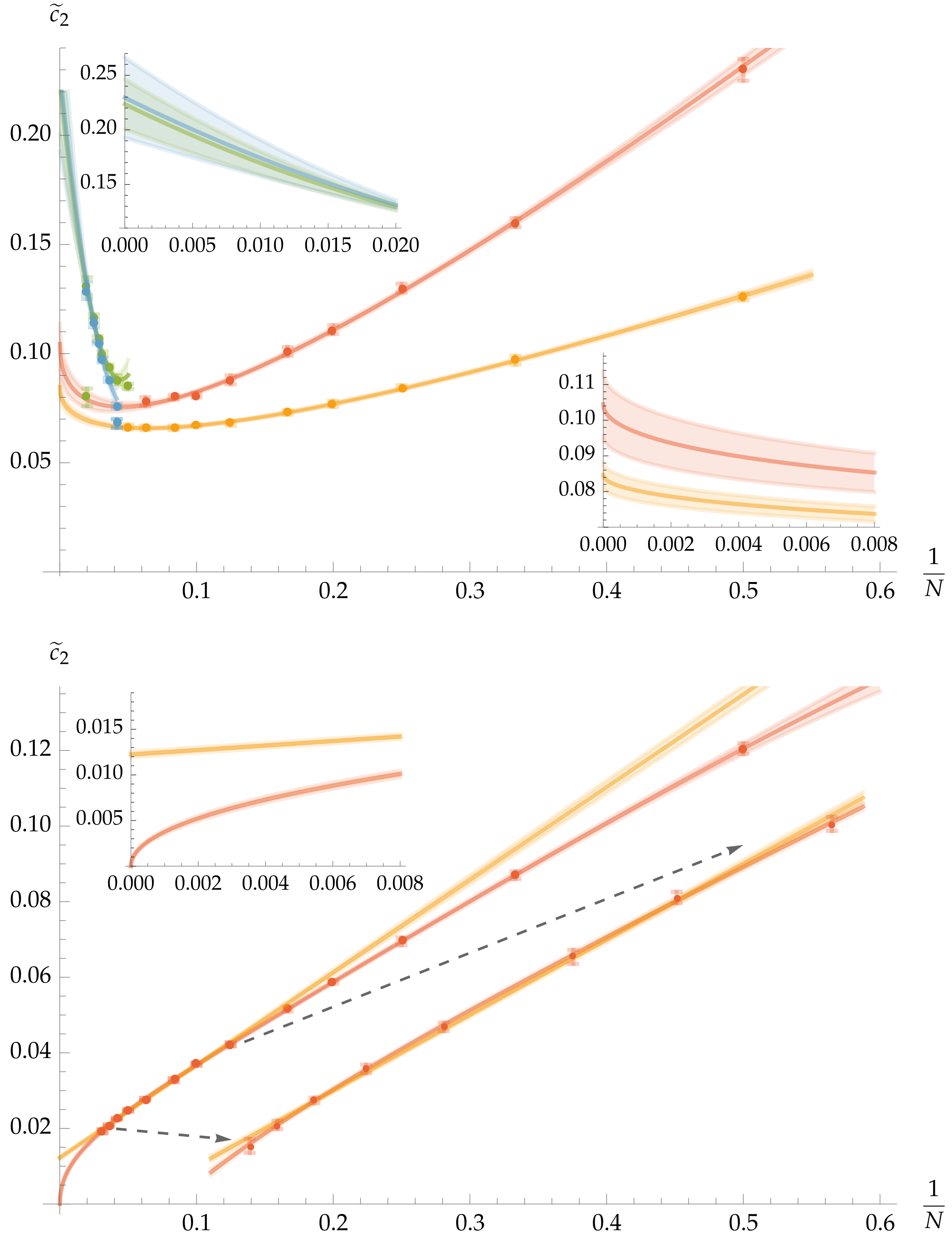

Figure 4.4: /TOP/ Transitions for $\widetilde{c}_4 = 0.01$, $\nu_k = 0$, $N \leq 50$ with zoomed-in large N limit. Top plots represent C (red and green) and the bottom ones χ (orange and blue). $N < 16$ is the 2-phase regime (red and orange) and $N > 16$ is the 3-phase regime (blue and green). The ↕→↑↓ transition peak fully separates from ↑↓→↑↑ peak for $N \geq 50$. Pale-coloured stripes represent the 68% confidence intervals. /BOTTOM/ Transitions for $\widetilde{c}_4 = 0.01$, $\nu_k = 0.5$, $N \leq 32$ with two zoomed-in regions. The orange/top line represents the linear fit for $N \geq 8$, the red/bottom one is our model's prediction. Pale-coloured stripes represent the 68% confidence intervals.

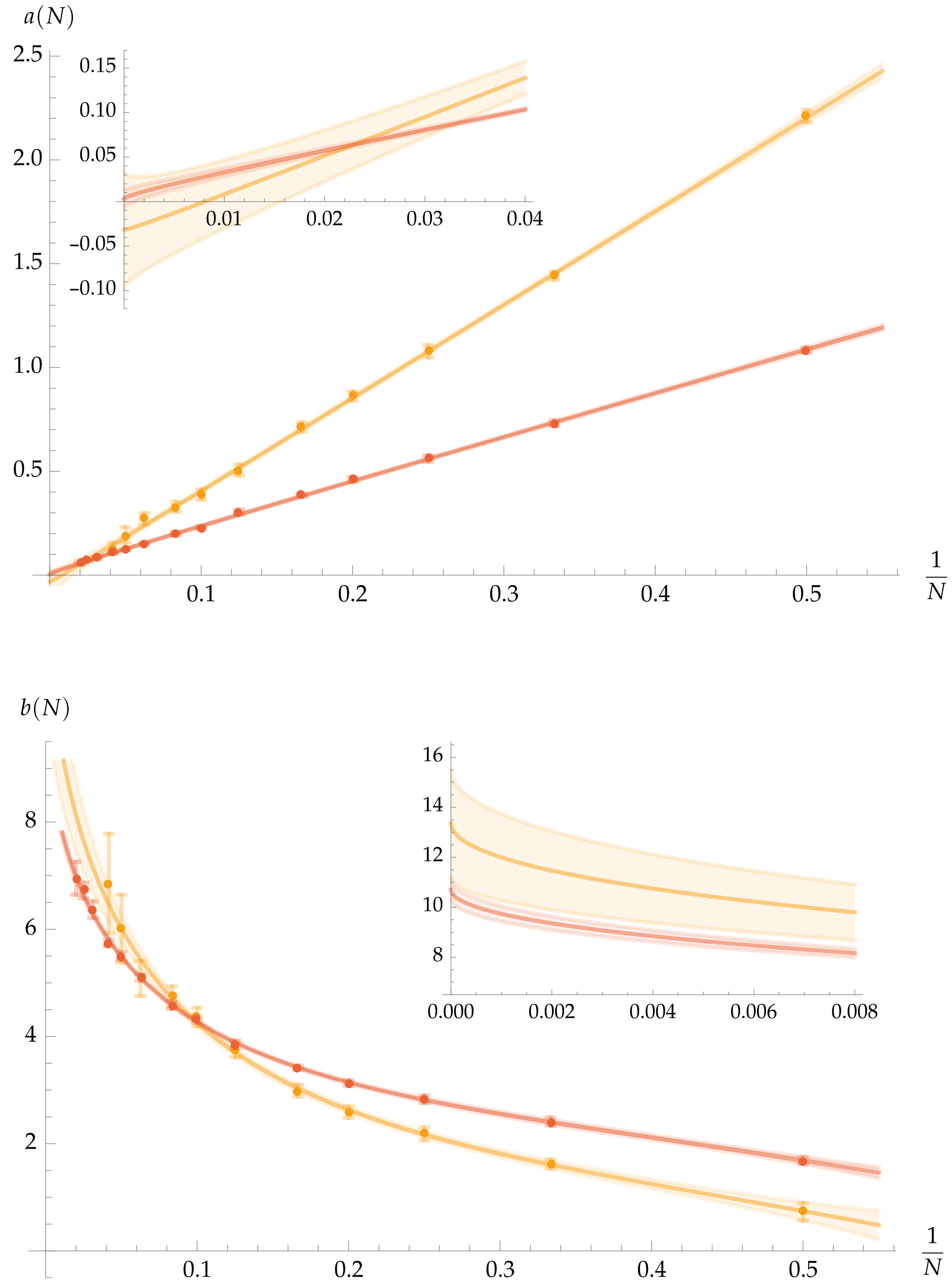

Figure 4.5: $a(N)$ and $b(N)$ coefficients of the ↕→↑↑ transition line constructed from peaks in C (orange/larger errors) and χ (red/smaller errors) for $N \leq 50$. Pale-coloured stripes represent the 68% confidence intervals. The large N limits are zoomed-in. As we can see, the square root behaviour of the transition line, governed by $a(N)$, completely disappears in the infinite matrix limit, leaving only the linear one.

we can compensate this by redefining the field during the integration $\Phi \to \Phi/\sqrt{\kappa}$, which reduces $\widetilde{c}_4{}'$ by factor κ^2. The specific heat now effectively sees the action with $\widetilde{c}_2$, and since we are still at the line connecting the maxima of C, it must hold

$$\frac{\widetilde{c}_4{}'}{\kappa^2} = \widetilde{c}_4 \qquad \Leftrightarrow \qquad \widetilde{c}_4{}' = \kappa^2 \widetilde{c}_4, \tag{4.3.24}$$

as if we returned to the starting point. This means that along the transition line $\widetilde{c}_2^2/\widetilde{c}_4$ must remain constant, which gives the square-root behaviour in (4.2.11) and which is just a reflection of the universal scaling properties of the phase transition. The situation complicates when we include kinetic term, since it is not accompanied by a variable coupling constant, and since we expect branching of the transition line. In the ↑↓ and ↑↑ phases, we expect the main action contribution to come from

$$\Phi^2 = \frac{\widetilde{c}_2}{2\widetilde{c}_4}\,\mathbb{1}, \tag{4.3.25}$$

where the classical potential is

$$S_{\mathrm{PP}} = -\frac{N^2 \widetilde{c}_2^2}{4\widetilde{c}_4}, \tag{4.3.26}$$

and the kinetic term

$$S_{\mathrm{K}} = \frac{\widetilde{c}_2}{2\widetilde{c}_4}\,\mathrm{tr}\left[iP_\alpha, \mathbb{1}_\pm\right]^2 \sim \frac{N^2 \widetilde{c}_2}{2\widetilde{c}_4}. \tag{4.3.27}$$

For large $\widetilde{c}_2$, the potential term will dominate, and we should expect the near square root behavior like in the PP model. In contrast, the kinetic term will dominate for small $\widetilde{c}_2$. Applying to it the similar logic of traveling along the transition line, this time towards the origin, we conclude that in order to preserve the form of the action, we require the ratio $\widetilde{c}_2/\widetilde{c}_4$ to remain constant, which translates into a linear transition line. The easiest way to reconcile these two limits is to assume a combination of the square root and linear behavior, or simply an expansion in square roots of $\widetilde{c}_4$, that contains these two as the leading terms.

The wrong choice of scaling would transform (4.3.22) into

$$\widetilde{c}_2 N^{-\Delta\nu_k} = a(N)\sqrt{\widetilde{c}_4 N^{-2\Delta\nu_k}} + b(N)\,\widetilde{c}_4\, N^{-2\Delta\nu_k}, \tag{4.3.28}$$

giving

$$\widetilde{c}_2 = a(N)\sqrt{\widetilde{c}_4} + b(N)\,\widetilde{c}_4 \left(\frac{1}{N}\right)^{\Delta\nu_k}. \tag{4.3.29}$$

We examined several variants of perturbative expansion of $a(N)$ and $b(N)$ as well as a few non-perturbative ones; we did not examine the more complicated possibility that they contain a residual dependence on $\widetilde{c}_4$. The ansatz series in $1/\sqrt{N}$ showed excellent agreement with the collected data:

$$a(N) = \sum_{k=0}^{\infty} \frac{a_i}{\sqrt{N}^k} = 0.01(1) + \frac{0.07(7)}{\sqrt{N}} + \frac{2.06(9)}{N}, \tag{4.3.30a}$$

$$b(N) = \sum_{k=0}^{\infty} \frac{b_i}{\sqrt{N}^k} = 10.5(5) - \frac{31(4)}{\sqrt{N}} + \frac{43(9)}{N} - \frac{24(8)}{N\sqrt{N}}. \tag{4.3.30b}$$

The series coefficients are confirmed by analyzing the transition point shifts for different choices of scaling $\Delta\nu_k$ (Appendix E). We also confirmed that the choice of $\nu_k = 0$ leads to a stable large N limit. In contrast, with an increase in matrix size, $\Delta\nu_k > 0$ transition points collapse to zero in the predicted manner, which is for $\Delta\nu_k \geq 1$ practically linear.

We can now explain peculiar behaviour of the $\nu_k = 0.5$ plot in Figure 4.4. Combining (4.3.29) and (4.3.30), we expect it to change as

$$\frac{a_1\sqrt{\widetilde{c}_4} + b_0\widetilde{c}_4}{\sqrt{N}} + \frac{a_2\sqrt{\widetilde{c}_4} + b_1\widetilde{c}_4}{N} + \frac{a_3\sqrt{\widetilde{c}_4} + b_2\widetilde{c}_4}{N\sqrt{N}}, \tag{4.3.31}$$

having near-constant slope around

$$N = 3 \cdot \frac{a_3\sqrt{\widetilde{c}_4} + b_2\widetilde{c}_4}{a_1\sqrt{\widetilde{c}_4} + b_0\widetilde{c}_4} \approx 3 \cdot \frac{b_2}{b_0} = 12(3), \tag{4.3.32}$$

which falls right in the middle of the observed flat region $8 \leq N \leq 32$ on $1/N$-axis. However, the slope would ultimately behave as $1/\sqrt{N}$ for large enough matrices.

Upon the publication of [46], we discovered a nice 3-parameter non-perturbative fit:

$$C: \quad b(N) = 11(5) - 14(4)e^{-0.23(13)\sqrt{N}}, \tag{4.3.33a}$$

$$\chi: \quad b(N) = 8.7(6) - 9.6(3)e^{-0.25(3)\sqrt{N}}. \tag{4.3.33b}$$

It would be interesting to reanalyze $\nu_k \neq 0$ data having such functional dependence of parameters in mind, as well as adding higher c_4-terms to the transition line equation. Interestingly, the perturbative estimate (4.3.30) for the large N limit of b is similar to the non-pertrubative one.

4.4 Curvature term scaling

Next, we wish to examine the scaling of the curvature term by looking at its effects on top of the PP model without complications of the kinetic term. We will thus consider $S_{\mathrm{R+PP}}$ in the relevant case where $c_r > 0$.

The NC curvature of the model is a negative diagonal matrix

$$R_{jj} = \mathcal{R} + 8 - \begin{cases} 16j, & 1 \leq j \leq N-1, \\ 8N, & j = N, \end{cases} \tag{4.4.34}$$

where $\mathcal{R} = {}^{15}/_{2}$. In this (and only this) section's simulation, we erroneously used $\mathcal{R} = {}^{15}/_{4}$, but that does not change the conclusions of the section because they depend on the $\mathcal{O}(N)$ part of the curvature. Diagonality of R yields $\mathrm{tr}\,(R\Phi^2) = R_{jj}(\Phi^2)_{jj}$, bounding the curvature term in the action by

$$\mathrm{tr}\left(c_r \min_j |R_{jj}|\Phi^2\right) \leq \mathrm{tr}\left(c_r|R|\Phi^2\right) \leq \mathrm{tr}\left(c_r \max_j |R_{jj}|\Phi^2\right), \tag{4.4.35}$$

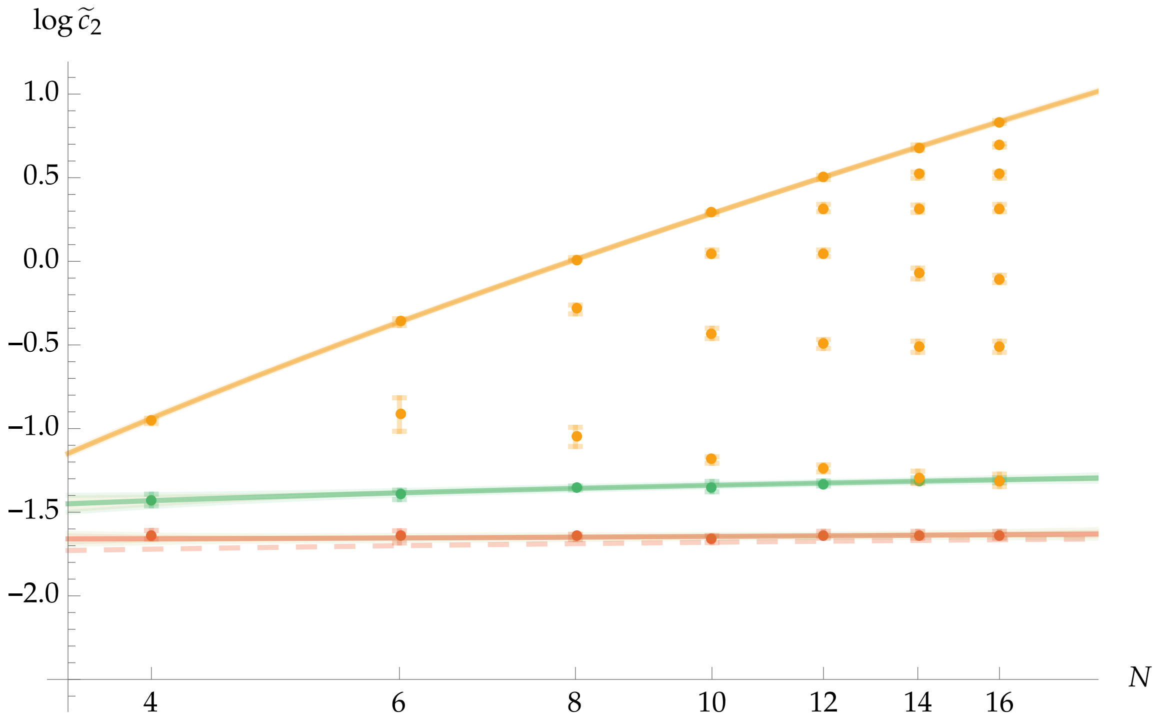

Figure 4.6: ↕→↑↓ transition in the PP model with curvature for $(c_r, \widetilde{c}_4) = (0.01, 0.01)$, $4 \leq N \leq 16$ and fixed $(\nu_2, \nu_4) = (1, 1)$, observed as peaks in χ and M. The green/center data represents the correct choice of scaling $\nu_r = 0$, the orange/top $\Delta\nu_r = +1$, the red/bottom $\Delta\nu_r = -1$ and the pale-red dashed line the PP model. For $\Delta\nu_r = +1$ and fixed N, magnetization peaks $N/2 - 1$ times (unconnected orange dots) with increasing $\widetilde{c}_2$ until χ reaches its maximum and eigenvalue distribution splits in two, causing the phase transition (connected orange dots). Errorbars are mostly covered by data markers and pale-coloured stripes represent the 68% confidence intervals.

which translates to

$$\operatorname{tr}\left((8-\mathcal{R})\widetilde{c}_r\Phi^2\right) \leq \operatorname{tr}\left(c_r|R|\Phi^2\right) \leq \operatorname{tr}\left((16N-(24+\mathcal{R}))\,\widetilde{c}_r\Phi^2\right). \tag{4.4.36}$$

Treating this as a bounded contribution to the mass term, we could naively expect it to be reflected in a deformation of the transition line $\widetilde{c}_2 \to \widetilde{c}_{2,r}$

$$\widetilde{c}_2 + \frac{8-\mathcal{R}}{N}\widetilde{c}_r \leq \widetilde{c}_{2,r} \leq \widetilde{c}_2 + \left(16 - \frac{24+\mathcal{R}}{N}\right)\widetilde{c}_r. \tag{4.4.37}$$

The wrong choice of scaling would change the previous formula into

$$\widetilde{c}_2 + \frac{8-\mathcal{R}}{N}\widetilde{c}_r N^{\Delta\nu_r} \leq \widetilde{c}_{2,r} \leq \widetilde{c}_2 + \left(16 - \frac{24+\mathcal{R}}{N}\right)\widetilde{c}_r N^{\Delta\nu_r}. \tag{4.4.38}$$

In other words, there is a shift of transition lines by $\delta\widetilde{c}_2 = \widetilde{c}_{2,r} - \widetilde{c}_2$ relative to the R-off case. The shift $\delta\widetilde{c}_2$ is proportional to the c_r, and their ratio is bounded by

$$\frac{1}{2N} \leq \frac{\delta\widetilde{c}_2}{c_r} \leq 16 - \frac{63}{2N}. \tag{4.4.39}$$

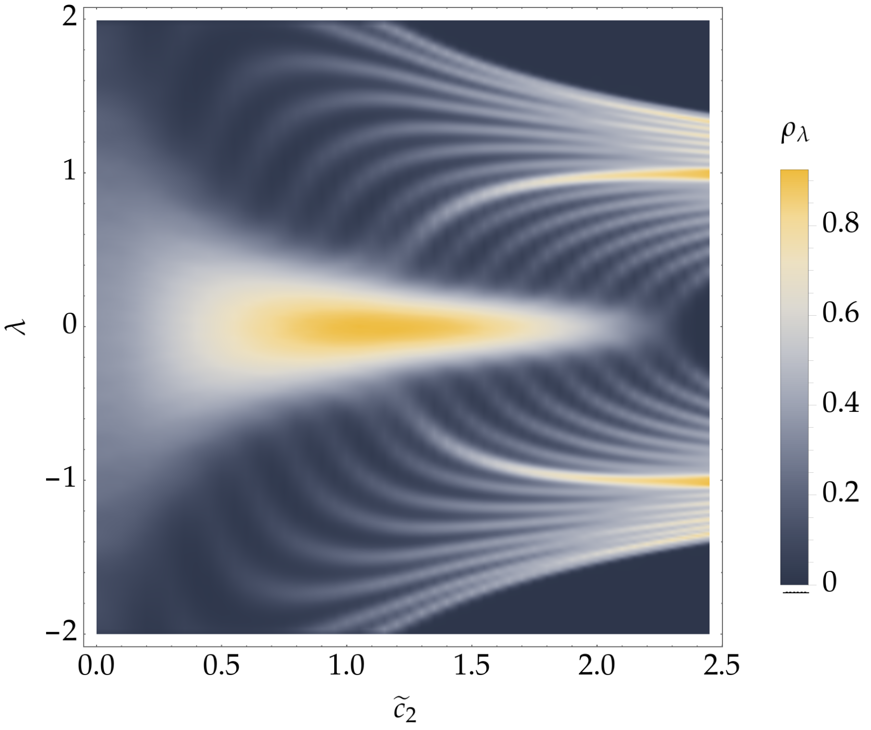

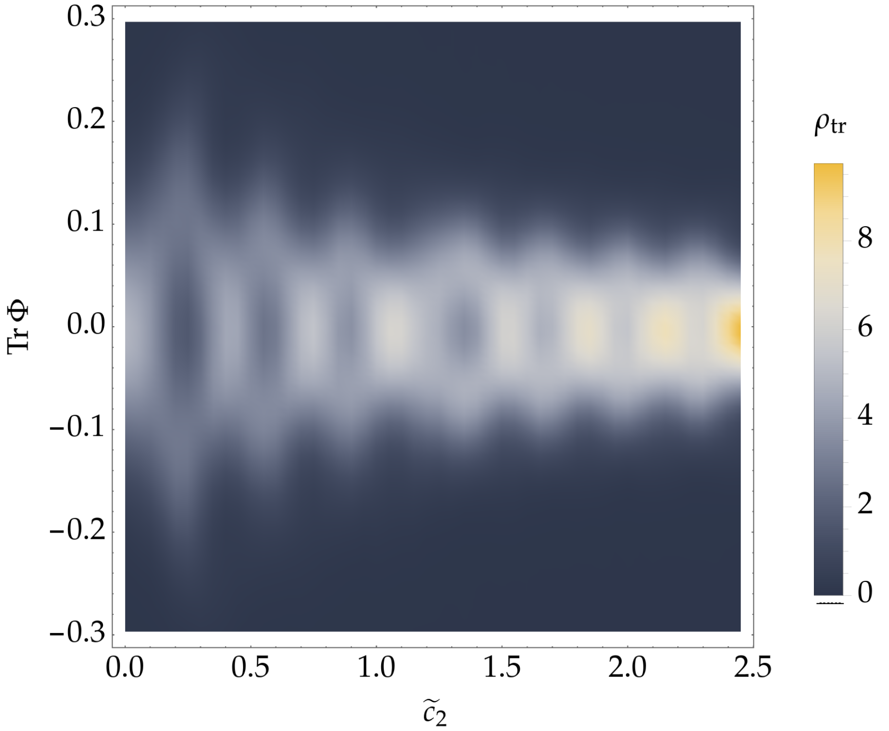

Figure 4.7: Eigenvalue (top) and trace (bottom) distributions of the PP model with $\Delta\nu_r = +1$ curvature for $N = 16$, $(c_r, \widetilde{c}_4) = (0.01, 0.01)$, $(\nu_2, \nu_4) = (1, 1)$ and varying values of $\widetilde{c}_2$. Brighter regions correspond to larger values and peaks of distributions. Central bright region in the left plot, which dims and widens to the left, depicts the $\updownarrow$-phase which at around $\widetilde{c}_2 \approx 2.3$ completely splits into two cuts of the $\uparrow\downarrow$-phase. Two thicker bright lines in the eigenvalue distribution plot are due to degenerate eigenvalues of the curvature matrix. Eigenvalues are expressed in units of $\sqrt{\operatorname{tr}\Phi^2/N}$ and traces in units of $\sqrt{N \operatorname{tr}\Phi^2}$.

In this section, we demonstrate the shift by numerical simulation at a token value of quartic coupling and with the absent kinetic term. We expose this effect in full in Figures 4.12 and 4.13 later in the text. Similar shifting is in the meantime also reported on the fuzzy sphere after adding a modification to the kinetic term [48].

In the case where $\Delta\nu_r < 0$, we would practically see the PP model. In contrast, $\Delta\nu_r > 0$ would lead to the $N^{\Delta\nu_r}$ runaway effect toward large values of the mass parameter. This is exactly what happens in Figure 4.6 to the slanted orange line

$$1.01(3)\log N - 1.83(9) - \frac{2.0(2)}{N}, \tag{4.4.40}$$

which, upon the substitution of (4.2.11), fits very well with the expansion of the right-hand side of (4.4.38)

$$\log N - 1.83 - \frac{0.48}{N}, \tag{4.4.41}$$

and its slope $1.01(3)$ with $\Delta\nu_r = 1$.

There are multiple peaks of M for $\Delta\nu_r = 1$, fixed N and varying $\widetilde{c}_2$, marked by unconnected orange dots in Figure 4.6, which complicates identification of the phase transition. However, only the topmost dots coincide with the peaks of χ, which we use as the indicator of the phase transition.

The identification is further confirmed by examining the eigenvalue distribution in Figure 4.7. One by one, peaks break off the edge of the shrinking deformed Wigner semi-circle as the mass parameter increases. Meanwhile, the trace distribution stays centered at zero. We interpret this as curvature eigenvalues activating with alternating signs, causing the magnetization to fluctuate and form peaks. This activation also causes the trace distribution to expand and contract around the zero mean. The oscillations continue until all eigenvalues separate from the bulk, susceptibility peaks, and the system transitions into a modified matrix phase around $\widetilde{c}_2 \approx 2.3$.

The right-hand side of (4.4.38) also predicts the shift between the $\Delta\nu_r = 0$ and the PP-line to be less than $16\,\widetilde{c}_r = 0.16$ and the actual difference at $N = 16$ is $0.15(4)$. As for the $\Delta\nu_r = -1$ line, it is practically indiscernible from the PP-line, as expected.

4.5 *R*-off diagram

Having inspected and fixed all the scalings, we can finally see how the phase diagram of $S_{\mathrm{K+PP}}$ model looks like. Figure 4.8 depicts the phase structure for $N = 24$ obtained from peaks in C. From $\widetilde{c}_4 = 0$ to $\widetilde{c}_4 \approx 0.015$, stretches the ↕→↑↑ transition line which can be approximated as

$$L_1: \quad \widetilde{c}_2 = 0.0015(4) + 8.8(1)\widetilde{c}_4, \tag{4.5.42}$$

followed by the ↑↓→↑↑ transition line

$$L_3: \quad \widetilde{c}_2 = -0.009(3) + 9.4(1)\widetilde{c}_4. \tag{4.5.43}$$

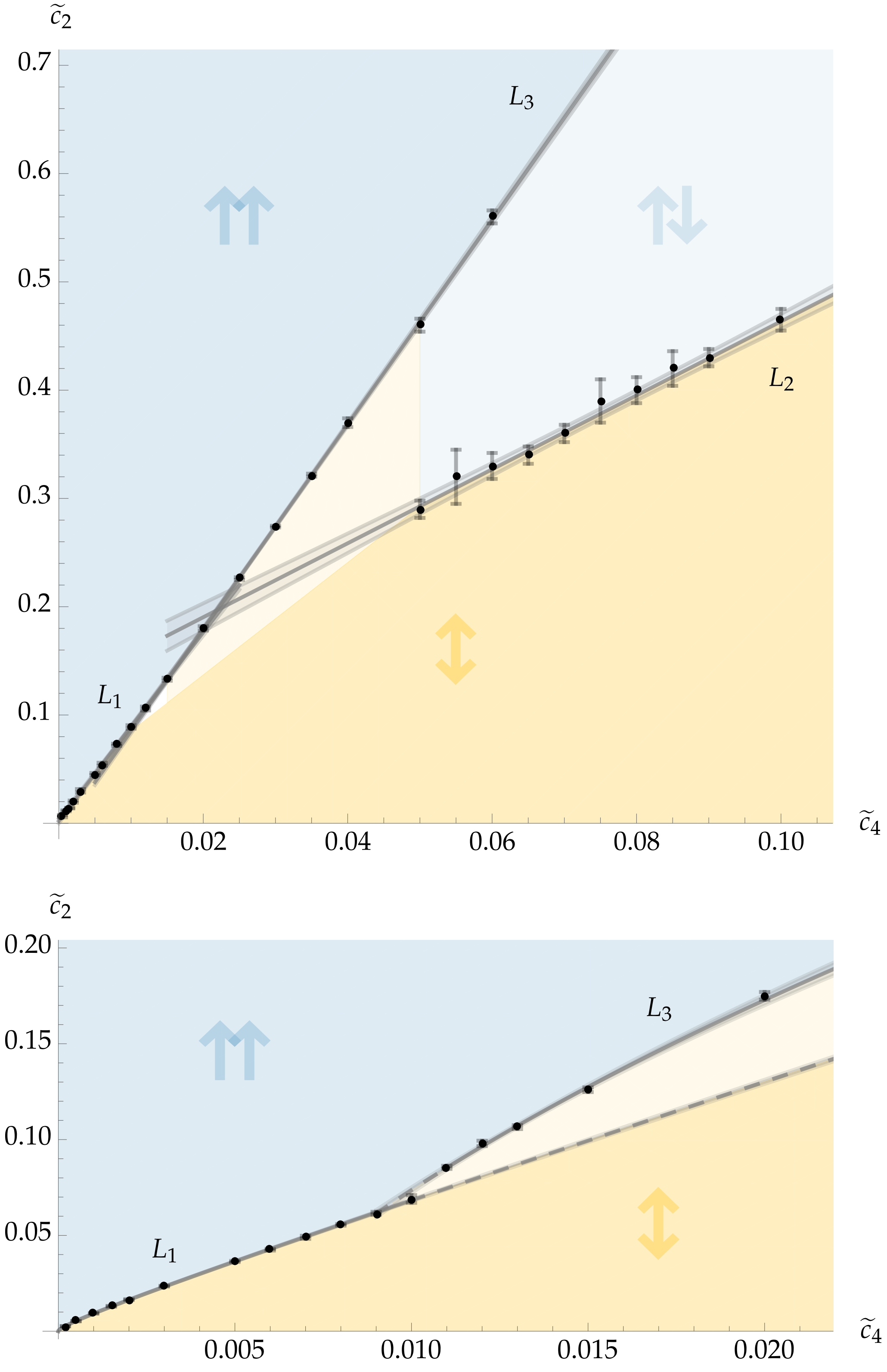

Figure 4.8: Phase diagram for $N = 24$. Pale-gray stripes represent 68% confidence intervals. The top diagram is constructed from peaks in C and the bottom one from peaks in χ. The bottom plot shows a zoomed-in region around the origin of the top plot. A pale yellow wedge between ↕ and ↑↑ phases represents the phase coexistence region, which shrinks with an increase in matrix size and presumably collapses into a triple point.

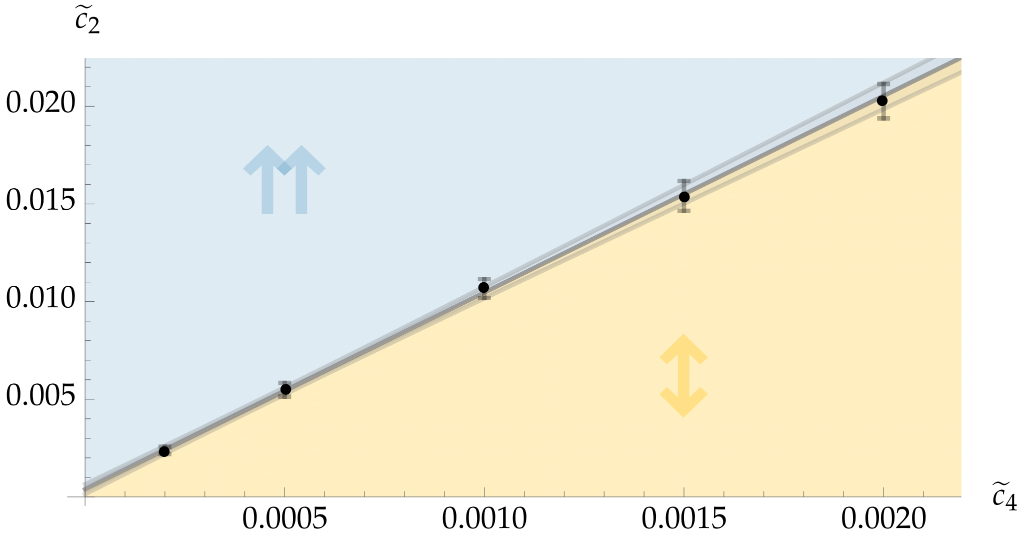

Figure 4.9: Large N extrapolation of the ↕→↑↑ transition line. Pale-gray stripes represent 68% confidence intervals.

The slopes of these lines are very similar, making it difficult to determine which points belong to which line; here comes to aid the χ-data in Figure 4.8, clearly showing the transition from L_1 to L_3. Near $\widetilde{c}_4 \approx 0.05$, C-diagram enters a 3-phase regime and ↕→↑↓ transition line appears, which is linear for smaller $\widetilde{c}_4$

$$L_2: \quad \widetilde{c}_2 = 0.12(3) + 3.5(3)\widetilde{c}_4, \tag{4.5.44}$$

and for larger values of $\widetilde{c}_4$ exhibits square root behaviour characteristic for the limiting PP model

$$L_2: \quad \widetilde{c}_2 = 2.62(5)\sqrt{\widetilde{c}_4} - 0.48(5) + \frac{0.039(9)}{\sqrt{\widetilde{c}_4}}. \tag{4.5.45}$$

This can also be seen on the fuzzy sphere [43], where it holds

$$\widetilde{c}_2 = 2.5\sqrt{\widetilde{c}_4} + \frac{0.5}{1 - \exp(1/\sqrt{\widetilde{c}_4})} \approx 2\sqrt{\widetilde{c}_4} + 0.25 - \frac{0.042}{\sqrt{\widetilde{c}_4}}. \tag{4.5.46}$$

It would be interesting to compare these two once the large N extrapolation of the L_2 is obtained. A very crude linear extrapolation of $N = 16, 20, 24$ gives promising $2.0(4)$ for the square root coefficient.

The extrapolation of L_2 intersects $L_{1/3}$ at $\widetilde{c}_4 \approx 0.02$, which is in the vicinity of the meeting point of L_1 and L_3 at $\widetilde{c}_4 \approx 0.015$ ($\widetilde{c}_4 \approx 0.01$ for χ-data), placing the would-be triple point nearby. The pale yellow triangle formed by the meeting point of L_1 and L_3 and the starting point of L_2 should collapse into a triple point when $N \to \infty$. This effect is demonstrated on the fuzzy sphere [45]. In this region, the two transition peaks are still convoluted into a single one, similarly to the peaks of χ in Figure 3.1.

Expression for L_3 should be taken with a grain of salt. Near this transition, the ergodicity of the algorithm starts to falter, contributing to an unknown systematic error.

Based on the analysis of $a(N)$ and $b(N)$ from Figure 4.5, the ↕→↑↑ transition line in the large N limit extrapolates to

$$\mathrm{C}: \quad \widetilde{c}_2 = -0.03(7)\sqrt{\widetilde{c}_4} + 13(3)\widetilde{c}_4, \tag{4.5.47a}$$

$$\chi: \quad \widetilde{c}_2 = +0.01(1)\sqrt{\widetilde{c}_4} + 10.5(5)\widetilde{c}_4, \tag{4.5.47b}$$

These two expressions agree, as they should, or we could otherwise conclude that the triple point is located at the origin, and that 3-phase regime exists throughout the parameter space. Apparently, the $\sqrt{\widetilde{c}_4}$ effect completely disappears, since both square root coefficients are indistinguishable from zero.

On the other hand, the equation of the ↕→↑↑ line in Figure 4.9, obtained from linear fit through large N limits at fixed $\widetilde{c}_4$, reads

$$\chi: \quad \widetilde{c}_2 = +0.0004(3) + 10.1(5)\widetilde{c}_4, \tag{4.5.48}$$

which agrees with estimates in (4.5.47) and Table E.1. Based on the extrapolation estimates of points that with increasing matrix size switch from the 2-phase to the 3-phase regime, it is possible that a systematic error from such still unidentified points could yield a lower true slope in (4.5.48). Namely, as triple point slides towards zero, it deforms the about-to-be-shortened end of the ↕→↑↑ transition line towards the less slanted ↕→↑↓ transition line. Also, the inclusion of the $\widetilde{c}_4^{3/2}$ term into (4.3.22) gives somewhat higher estimates for the linear term, although still consistent with the reported ones.

The smallest $\widetilde{c}_4$ for which we detected change from the 2-phase to the 3-phase regime in [46] is $\widetilde{c}_4 = 0.005$ at $N = 28$. In contrast, for all $\widetilde{c}_4 < 0.005$ and $N \leq 50$ we saw only two phases, implying that ↕→↑↑ transition line ends in the triple point at $\widetilde{c}_4(T) \leq 0.005$. This estimate is refined in [69] and Section 5.2

4.6 *R*-on diagram

Let us now turn on the curvature term. We will first explore what happens under a fixed curvature coupling. Then we will slowly turn it off as a part of the GW-mediated renormalization of the $\lambda\phi_\star^4$ model.

In Figure 4.10, we see examples of measured thermodynamic observables of the full model. Once again, we hunt for characteristic changes in their shapes as we vary the mass parameter.

As already stated, there is now the new relevant quasi-solution of the classical EOM, namely Φ_r. Let us analyze positions of eigenvalue-distribution peaks to convince ourselves that Φ_r is a good candidate for the true vacuum configuration. For large enough $\widetilde{c}_2 \gg c_r > 0$, which lies in the far ↑↑-phase, we can expand

$$\Phi_r^{\uparrow\uparrow} = \sqrt{\frac{c_2\,\mathbb{1} + c_r R}{2c_4}} \approx \sqrt{\frac{c_2}{2c_4}}\left(\mathbb{1} - \frac{c_r|R|}{2c_2}\right), \tag{4.6.49}$$

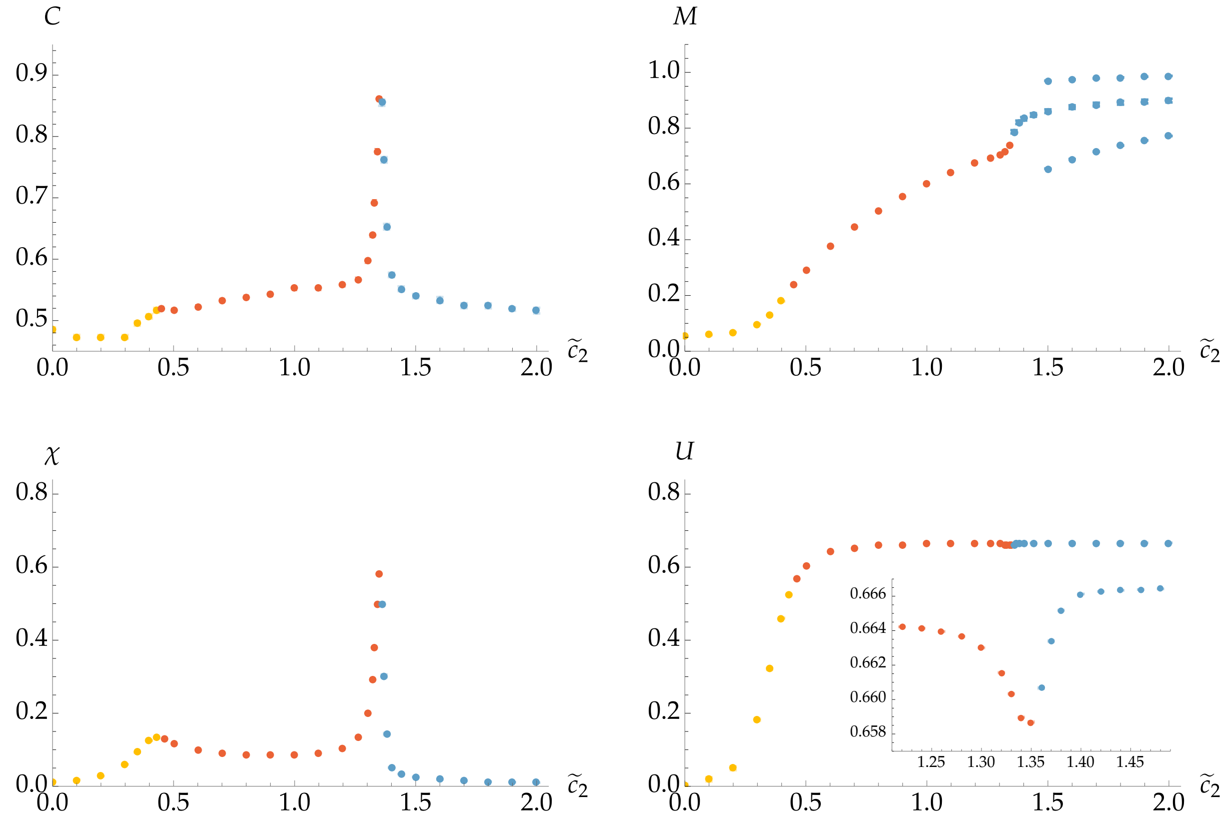

Figure 4.10: Thermodynamic observables for $N = 24$, $(c_k, c_r, \widetilde{c}_4) = (1, 0.1, 0.05)$, as functions of $\widetilde{c}_2$. Errorbars are mostly covered by data markers. Central magnetization data is given in units of $\sqrt{N \langle \operatorname{tr} \Phi^2 \rangle}$. The top and bottom data on the right-hand side of the M-plot are the same as the central, only expressed respectively in units of $\operatorname{tr} \Phi_r$ and $\operatorname{tr} \Phi_{\text{PP}}$, where $\Phi_r = \sqrt{(c_2 \mathbb{1} + c_r R)/(2c_4)}$ and $\Phi_{\text{PP}} = \sqrt{c_2 \mathbb{1} / (2c_4)}$. Based on these, the oscillations around Φ_r better describe the uniformly-ordered phase than oscillations around Φ_{PP}. There are apparently two transitions corresponding to the two peaks in C and χ. Two of the three phases corresponding to these transitions are clearly visible in plots of M and U, while the third one is indicated by dents in their slope profiles. The disordered phase is colored in orange and the ordered phase in blue, while the possible intermediary phase is colored red.

leading to eigenvalue separation $\Delta\lambda$ of

$$\frac{\Delta\lambda}{\lambda_{\text{PP}}} = \frac{8c_r}{\widetilde{c}_2}, \qquad \lambda_{\text{PP}} = \sqrt{\frac{\widetilde{c}_2}{2\widetilde{c}_4}}. \tag{4.6.50}$$

This is exactly what we see in Figure 4.11. Average eigenvalue separation for 9 rightmost peaks is 0.0227(3), whereas the separation predicted by (4.6.50) is 0.02. We can even see the degenerate R_{NN} eigenvalue giving irregular 6th and 7th peak from the left, traveling towards its expected middle position. A similar exact analysis is not available for less extreme values of c_2, but the same qualitative behavior of the eigenvalue-distribution shape holds.

Let us try to analytically compare the energies of Φ_r and the other three classical vacua. We have

$$S_N(\Phi_r^{\uparrow\uparrow}) = \operatorname{tr}\left(\Phi_r^{\uparrow\uparrow} \mathcal{K} \Phi_r^{\uparrow\uparrow} - \frac{(c_2 \mathbb{1} + c_r R)^2}{4c_4} \right). \tag{4.6.51}$$

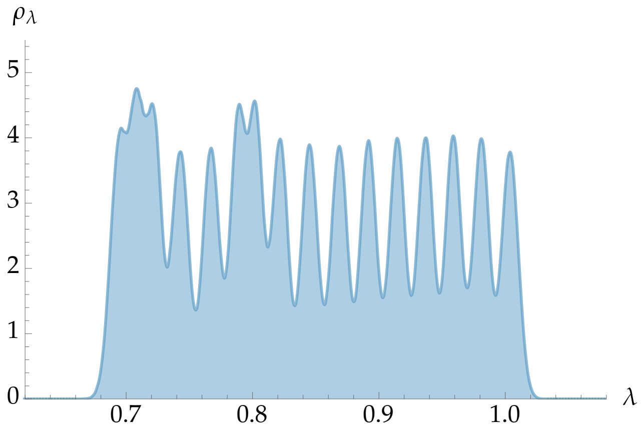

Figure 4.11: Distribution ρ_λ of eigenvalues λ for $N = 16$ and $(\widetilde{c}_k, \widetilde{c}_r, \widetilde{c}_2, \widetilde{c}_4) = (1, 0.1, 2.5, 0.01)$. λ is given in units of λ_{PP}. Average eigenvalue separation for 9 rightmost peaks is 0.0227(3) and predicted by (4.6.50) is 0.02. We can even see the R_{NN} eigenvalue giving irregular 6th and 7th peak from the left, traveling towards its expected middle position.

Using the expansion (4.6.49) and noting that $\mathcal{K}\,\mathbb{1} = 0$, we immediately find

$$\operatorname{tr}\Phi_r^{\uparrow\uparrow}\mathcal{K}\Phi_r^{\uparrow\uparrow} = \frac{c_r}{2c_2}\sqrt{\frac{c_2}{2c_4}}\operatorname{tr}\mathcal{K}R + O(c_r^2). \tag{4.6.52}$$

But since $\mathcal{K}$ is just a commutator and trace of a commutator is zero, we have

$$\operatorname{tr}\Phi_r^{\uparrow\uparrow}\mathcal{K}\Phi_r^{\uparrow\uparrow} = 0 + O(c_r^2). \tag{4.6.53}$$

Interestingly, for $c_r < 0$, the R-off solutions to the EOM are not the minima of the action:

$$\begin{aligned} S_N(\Phi_r^{\uparrow\uparrow}) &= \operatorname{tr}\left(\Phi_r^{\uparrow\uparrow}\mathcal{K}\Phi_r^{\uparrow\uparrow} - \frac{(c_2\,\mathbb{1} + c_r R)^2}{4c_4}\right) \\ &= \operatorname{tr}\left(-\frac{(c_2\,\mathbb{1} + c_r R)^2}{4c_4} + O(c_r^2)\right) = -\operatorname{tr}\left(\frac{c_2^2\,\mathbb{1} + 2c_2|c_r R|}{4c_4} + O(c_r^2)\right) \\ &< -\operatorname{tr}\frac{c_2^2\,\mathbb{1}}{4c_4} = S_N(\Phi^{\uparrow\uparrow}) < S_N(\Phi^{\uparrow\downarrow}) < S_N(\Phi^{\updownarrow}) = 0. \end{aligned} \tag{4.6.54}$$

In addition, since $S_N(\Phi^{\uparrow\downarrow})$ has a positive kinetic term independent of c_r, it follows that even for the small enough $c_r > 0$ still holds $S_N(\Phi_r^{\uparrow\uparrow}) < S_N(\Phi^{\uparrow\downarrow})$.

This is a good place to give more details on the structure of the phase diagrams and to compare the R-off and the R-on case. Three phases of the model are depicted[*] in Figures 4.12 and 4.13. Both transitions out of the stripe phase follow the square root behavior for larger quartic coupling. For $N = 24$ and $\widetilde{c}_4 > 1$, they are well approximated by expressions given in Table 4.3. For comparison, a pure potential model would show only a $\updownarrow \to \uparrow\downarrow$ transition line $\widetilde{c}_2 = 2\sqrt{\widetilde{c}_4}$ in the infinite N limit. As it can be seen from the Table 4.3, in the $\widetilde{c}_4 \geq 1$ regime, the curvature-induced shifts of the transition lines are significantly smaller than the maximal value $16c_r$ predicted by the arguments of Section 4.4, unlike for the small-$\widetilde{c}_4$ regime in Section 4.4.

We could try to apply the approach from the Appendix B for the PP model to predict the form of the R-on transition line. We will first discard the kinetic term, since Figure 3.1 indicates that it stays fairly constant throughout the $\uparrow\downarrow$-phase. Next, we need to integrate

---

[*] Throughout the rest of this text, we will use *Wolfram Mathematica* bluish *StarryNightColors* scheme for R-off plots and reddish *SunsetColors* scheme for R-on plots.

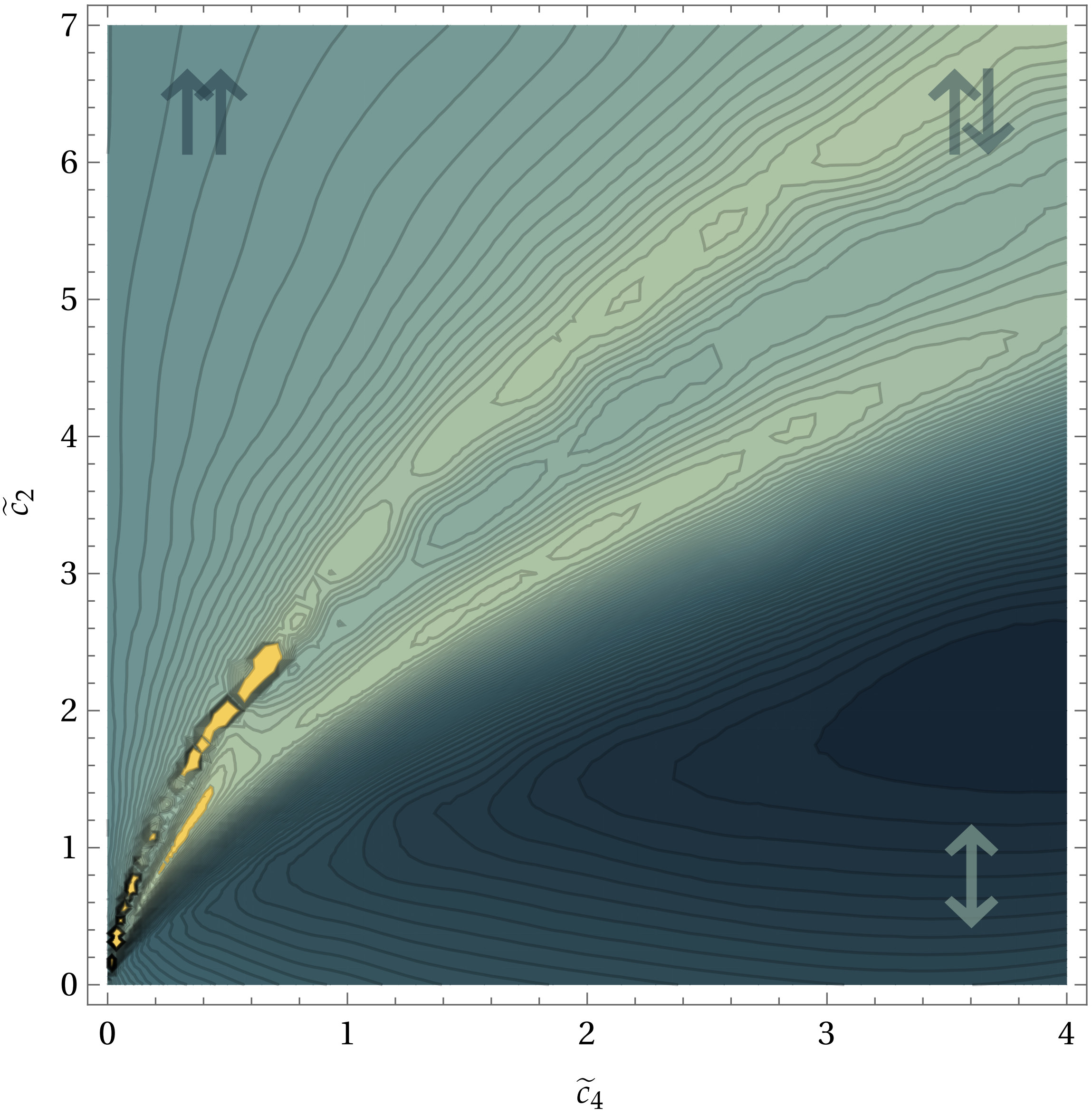

Figure 4.12: /*R*-OFF/ Contour plot of $N = 24$ phase diagram for $c_r = 0$. Darker colors depict lower and lighter colors higher values of specific heat, bright stripes being the transition lines. Semi-transparent arrows in the corners of the plot denote phases: ↕-phase occupies the bottom right, ↑↑-phase the upper left, while the ↑↓-phase is sandwiched in between, extending towards the upper right corner. The diagram is constructed based on more than 6000 points.

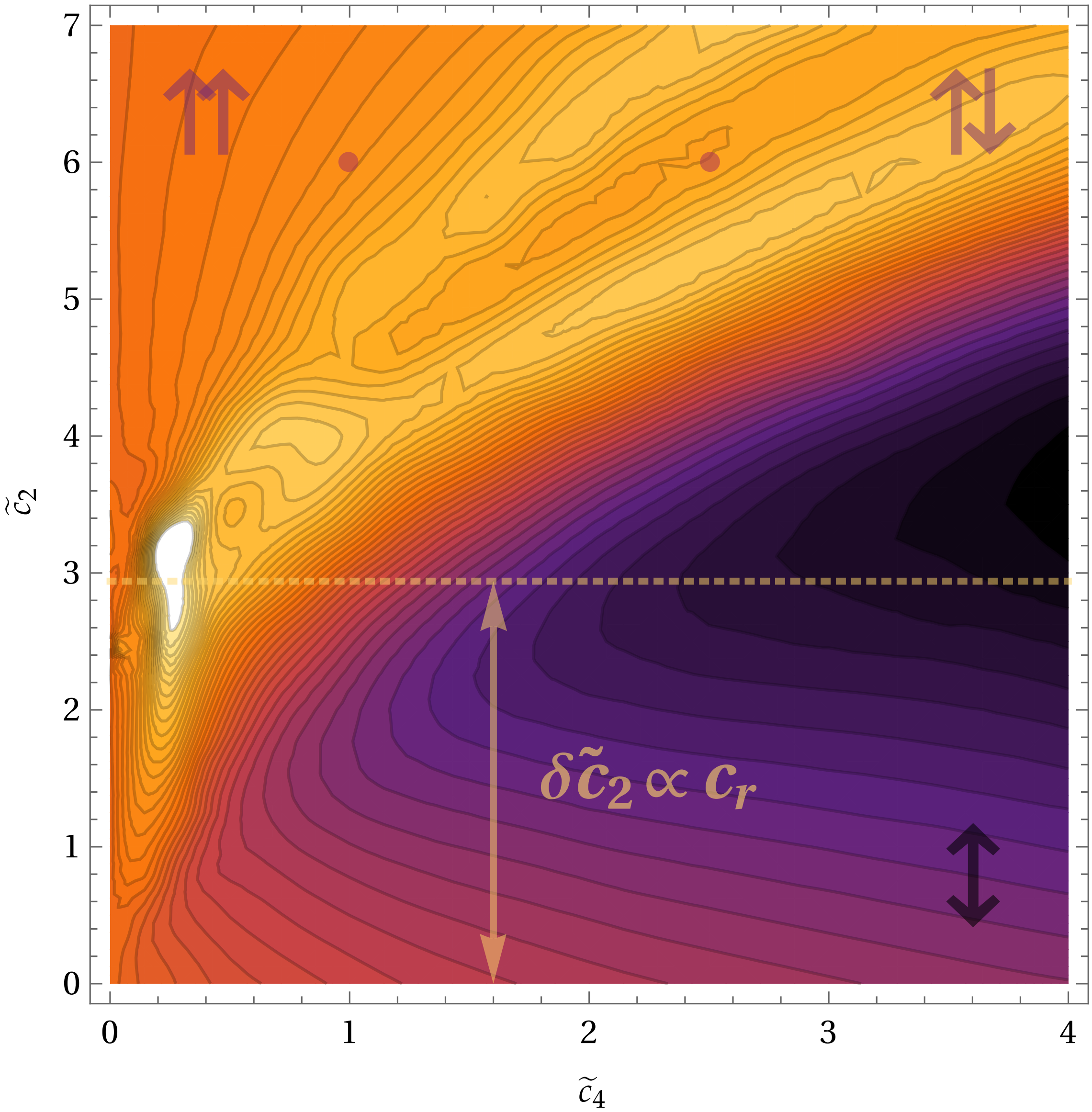

Figure 4.13: /*R*-ON/ Contour plot of $N = 24$ phase diagram for $c_r = 0.2$. Darker colors depict lower and lighter colors higher values of specific heat, bright stripes being the transition lines. The dotted line indicates a diagram shift $\delta\tilde{c}_2$ relative to the *R*-off case, which is proportional to c_r. Semi-transparent arrows in the corners of the plot denote phases: ↕-phase occupies the bottom right, ↑↑-phase the upper left, while the ↑↓-phase is sandwiched in between, extending towards the upper right corner. The diagram is constructed based on more than 1700 points. At two red points (1, 6) and (2.5, 6), phases are confirmed by detailed inspection of the available false vacuum solutions (see Appendix D).

Table 4.2: The ↕→↑↓ transition in the $S_{\mathrm{R+PP}}$ sub-model for $N = 24$ and $c_r = 0.1$. Difference between C- and χ-data is due to finite N effects and it gets smaller as we increase N.

$\widetilde{c}_2$ @ data	for $\widetilde{c}_4 =$	1.00	2.00	3.00
C		3.00(9)	3.80(2)	4.45(7)
χ		2.80(9)	3.60(10)	4.20(18)
C/χ-midpoint		2.90(6)	3.70(6)	4.32(10)
expected		2.91	3.70	4.33

out the unitary degrees of freedom and obtain the effective action that depends only on eigenvalues λ_i of the field. This is done via HCIZ formula [52, 53]

$$\int\limits_{U(N)} dU\, e^{t\,\mathrm{tr}\,AUBU^\dagger} = \frac{c_N}{t^{N(N-1)/2}} \frac{\det \mathring{e}^{\,t|a\rangle\langle b|}}{\Delta(A)\Delta(B)}, \tag{4.6.55}$$

where A and B are Hermitian matrices whose respective eigenvalues a_i and b_j are arranged in vectors

$$|a\rangle = \mathrm{col}\, a_i, \qquad \langle b| = \mathrm{row}\, b_j, \tag{4.6.56}$$

$\mathring{e}$ is the Hadamard element-wise matrix exponential

$$\left(\mathring{e}^{\,M}\right)_{ij} = e^{M_{ij}}, \qquad \left(\mathring{e}^{\,t|a\rangle\langle b|}\right)_{ij} = e^{ta_i b_j}, \tag{4.6.57}$$

and

$$c_N = \prod_{k=1}^{N-1} k!, \qquad \Delta(A) = \prod_{1\le i<j\le N} (a_j - a_i). \tag{4.6.58}$$

Using the formulas from Appendix G, it is easy to check that for our curvature term† holds

$$A = \mathrm{diag}(1, 2, \ldots, N) \approx \frac{|R|}{16}, \qquad B = \Lambda = \mathrm{diag}\, \lambda_i^2, \qquad t = -16c_r, \tag{4.6.59}$$

so the HCIZ integral (4.6.55) equals

$$\exp\left(-\sum_{i>0} (16c_r)^i S_N^{(i)}\right), \qquad S_N^{(i)} = O(N^2) \tag{4.6.60}$$

where the first three terms are

$$S_N^{(1)} = -\frac{N+1}{2}\,\mathrm{tr}\,\Lambda^2, \qquad S_N^{(2)} = -\frac{N}{24}\,\mathrm{tr}\,\Lambda^4 + \frac{1}{24}\,\mathrm{tr}^2\,\Lambda^2, \qquad S_N^{(3)} = 0. \tag{4.6.61}$$

As a sanity check, these formulas can be directly verified for $N \le 6$ using *Mathematica*.

If we denote the action without the curvature term by $S_N^{(0)}$, we can write the effective

---

†For simplicity, in A, we dropped the constant part of R irrelevant in the large N limit.

Table 4.3: Comparison of the full model transition line equations for $\widetilde{c}_4 \geq 1$ in the *R*-off and the *R*-on case.

transition	$\updownarrow \to \uparrow\downarrow$	$\uparrow\downarrow \to \uparrow\uparrow$
$c_r = 0.0$	$\widetilde{c}_2 = 2.67(5)\sqrt{\widetilde{c}_4} - 0.55(7)$	$\widetilde{c}_2 = 3.99(4)\sqrt{\widetilde{c}_4} - 0.90(5)$
$c_r = 0.1$	$\widetilde{c}_2 = 2.60(4)\sqrt{\widetilde{c}_4} + 0.32(6)$	$\widetilde{c}_2 = 3.95(6)\sqrt{\widetilde{c}_4} - 0.3(1)$
shift	$0.87(9) = 8.7(9)c_r$	$0.6(1) = 6(1)c_r$
expected	$8c_r + O(c_r^2)$	$8c_r + O(c_r^2)$

action as

$$S_N^{\text{eff}} = S_N^{(0)} + \sum_{i>0} (16c_r)^i S_N^{(i)} - \log \Delta^2(\Lambda). \tag{4.6.62}$$

At the level of distributions, the effects up to $O(c_r^3)$ only shift the parameters of the PP model

$$\widetilde{c}_2 \to \widetilde{c}_2 - 8c_r - \Delta\widetilde{c}_2, \qquad \widetilde{c}_4 \to \widetilde{c}_4 - \frac{32}{3}c_r^2, \tag{4.6.63}$$

where $\Delta\widetilde{c}_2 \propto c_r^2$ comes from the $\operatorname{tr}^2 \Phi^2$ term and can be determined from a Hartree-Fock-like self-consistency condition for $\langle \operatorname{tr} \Phi^2 \rangle$ [74]. Heuristically, this can be viewed as a factorization replacement

$$\operatorname{tr}^2 \Phi^2 \to \left\langle \operatorname{tr} \Phi^2 \right\rangle \operatorname{tr} \Phi^2 \tag{4.6.64}$$

in the large N limit. With these replacements, the transition line equation becomes

$$\widetilde{c}_2 = 2\sqrt{\widetilde{c}_4 - \frac{32}{3}c_r^2} + 8c_r + \frac{\frac{64}{3}c_r^2}{\sqrt{\widetilde{c}_4 - \frac{32}{3}c_r^2}}. \tag{4.6.65}$$

For large $\widetilde{c}_4 \gg {}^{32}/_{3}\, c_r^2$, it is approximated by

$$\widetilde{c}_2 \approx 2\sqrt{\widetilde{c}_4} + 8c_r + \frac{32}{3}\frac{c_r^2}{\sqrt{\widetilde{c}_4}}. \tag{4.6.66}$$

A quick simulation of the $S_{\text{R+PP}}$ model for $N = 24$ at $c_r = 0.1$ for larger values of $\widetilde{c}_4$ gave excellent agreement with the expected results, as it can be seen from Table 4.2. The full model transition line shift in Table 4.3 also agrees nicely with the first order shift $8c_r$ in (4.6.66).

Chapter 5

Renormalization footprints

This chapter inspects the connection between renormalization and the stripe phase.

The triple point controls the extension of the ↑↓-phase at its lower border. Therefore, we analyze its position, both in the *R*-on and the *R*-off case. First, we elaborate on detection of the triple-point position. Then we proceed to find its large *N* limit and connect it to the GW model-mediated renormalization. Finally, we speculate how to transplant the conclusions from the scalar model to the gauge model case.

This chapter is based on our published works [69, 23].

5.1 Triple point proxies

Let us start by discussing the triple-point proxies used to find the large *N* limit of the phase diagram. Unlike the phase transition points, the location of the triple point in the parameter space is not that easy to pinpoint, and χ- and C-data require different approaches.

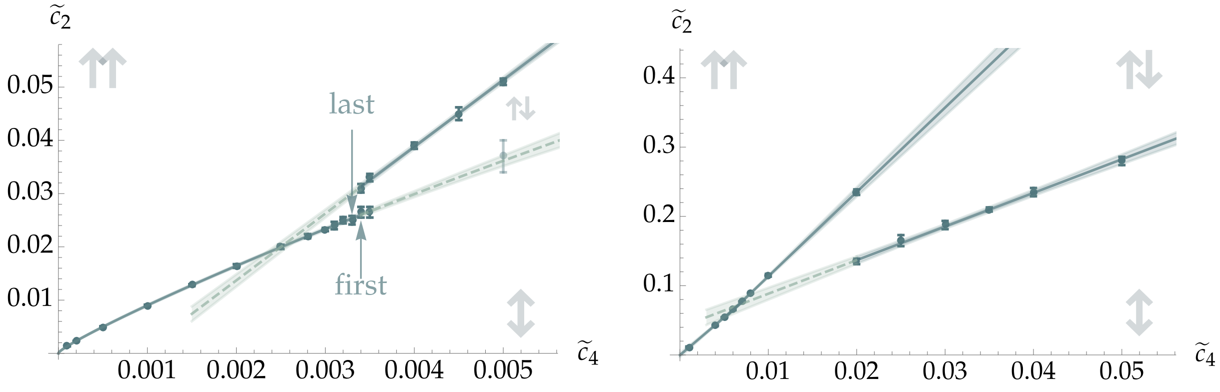

Figure 5.1: Phase diagrams for $N = 40$ in the vicinity of the triple point. /LEFT/ Change in slope of the ↑↑-phase border indicates a triple point. Arrows mark the last point on ↕→↑↑ and the first point on ↕→↑↓ lines. Constructed from the χ-data. /RIGHT/ Extrapolated transition lines with 83% confidence intervals. Constructed from the C-data.

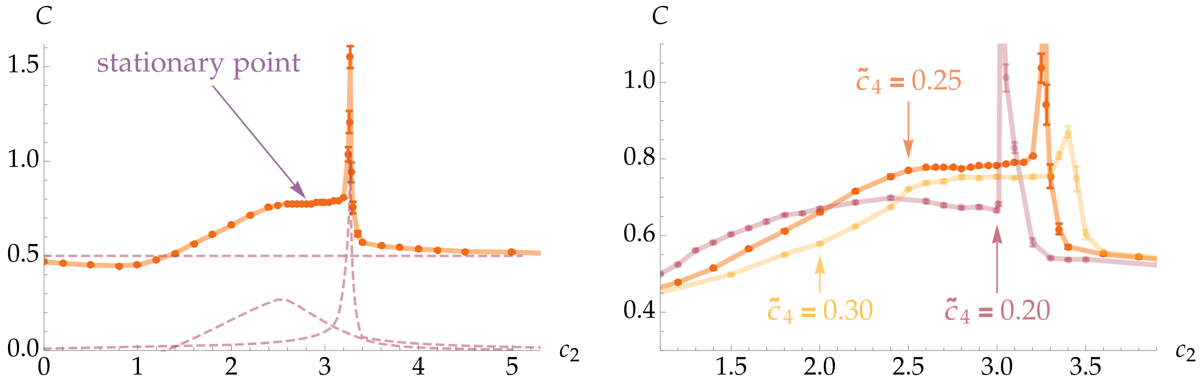

Figure 5.2: /LEFT/ Triple point region for $N = 24$, $c_r = 0.2$ at $\tilde{c}_4 = 0.25$ resolved into two peaks. The stationary point at the plateau is chosen as the triple point proxy. /RIGHT/ Plateau at $\tilde{c}_4 = 0.25$ mounts above plateaus at $\tilde{c}_4 = 0.20$ and $\tilde{c}_4 = 0.30$, building a wall between phases.

Figure 5.1 shows that as the $\updownarrow\to\uparrow\uparrow$ line bifurcates into $\updownarrow\to\uparrow\downarrow$ and $\uparrow\downarrow\to\uparrow\uparrow$, the split of the profile of χ into two separate peaks (similar to C in Figure 5.2)) changes the slope of the $\uparrow\uparrow$-phase border $\partial_{\uparrow\uparrow}$. Therefore, the midpoint between the last point in the one-peak and the first point in the two-peak regime served as the triple point proxy for Figure 5.3. We used the standard deviation of the triangular distribution ending at these two points as the triple point position uncertainty. For $N \leq 24$, the two peaks are not completely separated in the triple point region, so we instead took the intersection of extrapolated transition lines.

For consistency, we also checked the C-data, which has less predictive power due to larger uncertainties and distance from the triple point region. We there extrapolated $\updownarrow\to\uparrow\downarrow$ transition line to its intersection with $\partial_{\uparrow\uparrow}$. To get 68% confidence intervals of the intersection point coordinates, we used 83% confidence intervals of transition line fits since the probability of triple point belonging to their intersection is given by

$$P(\updownarrow\to\uparrow\downarrow \cap \partial_{\uparrow\uparrow}) = P(\updownarrow\to\uparrow\downarrow)P(\partial_{\uparrow\uparrow}) \tag{5.1.1}$$

and $0.68 \approx 0.83^2$.

In the R-on case, we used contour diagrams (e.g. Figure 4.13) to detect the beginning of the $\uparrow\downarrow$-phase from the C-data. We looked at the position of a bright triple-point peak and then checked the neighboring raw data to pinpoint its exact location. As shown in Figure 5.2, the peak resolves into two very closely spaced convoluted peaks—which presumably coincide when matrix size increases—joined by a wall that separates phases. For Figure 5.4, we used the position of the protruding peak shown in Figure 5.2, which gave a slightly higher estimate for the slope of the $c_2(T|r) = f(c_r)$ line than (5.3.7). The stationary point on this wall seems a more realistic estimator of the triple point position, but it is also more difficult to measure. A rough estimate using the stationary point

$$\tilde{c}_2(T|r) = 13.2(11)c_r + 0.24(9), \tag{5.1.2}$$

fits within the interval (4.4.39) and is close to its upper bound. For comparison, the slope calculated from the smaller peaks is around 12.

Looking at Figure 4.13, we see a small oval local minimum region with a bright triple point peak at its lower left edge. Eigenvalue distribution there has the characteristics of the ↑↓-phase. We do not believe this to be a separate phase but instead a finite-size effect that collapses into a triple point as the matrix size increases. This should be, of course, checked at larger N. In addition, between the triple point and origin in the R-on case, there is a transitional region where curvature eigenvalues in (3.1.24) slowly activate as we go from the ↕ to the ↑↑-phase. This region might constitute a separate partially-ordered phase but requires more data and further analysis.

Different extrapolations of the triple point position as a function of the inverse matrix size are collected in Table F.1.

5.2 *R*-off triple point

In the spirit of Bayesian probability notation, we will write the coordinates c_i of the triple point T in the R-on and R-off case as $c_i(T|r)$ and $c_i(T|\not r)$, respectively.

In [46], we found that the triple point of $\widetilde{\mathcal{S}}_0$ lies at $\widetilde{c}_4(T|\not r) \lesssim 0.005$ (alternatively: $c_4(T|\not r) \lesssim 0.14$ from $N = 28$ data) and established the descending trend of $\widetilde{c}_4(T|\not r)$ with increase in matrix size. In the meantime, we collected more data for matrix sizes up to $N = 70$, allowing us to track the shrinking rate of the ↕→↑↑ transition line. Unexpectedly, this transition disappears entirely and the triple point collapses into the origin (Figure 5.3).

Appendix 5.1 provides details on locating the triple point from raw data as well as different attempted data fits (Table F.1). We modeled small aberrations from the linear trend set by larger matrices by quadratic and power-law functions of $1/N$. All the estimates agree with a triple point lying at the origin in the large N limit, and the best one bounds its coordinates to

$$(c_2,\, c_4)_T \leq (0.16,\, 0.018) \tag{5.2.3}$$

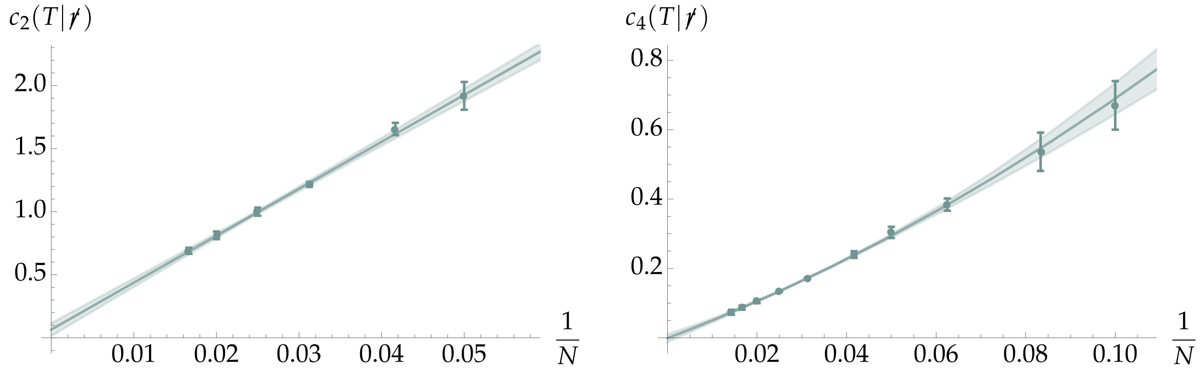

Figure 5.3: Coordinates of the triple point in the R-off case as a function of the inverse matrix size. /LEFT/ Linear fit of the c_2-coordinate: $c_2(T|\not r) = +0.07(5) + 37(2)/N$. /RIGHT/ Quadratic fit of the c_4-coordinate: $c_4(T|\not r) = -0.000(12) + 4.9(7)/N + 20(10)/N^2$. Data gathered from susceptibility χ for $N \leq 70$. The ↕→↑↑ transition line ending in T shrinks with an increase in matrix size, and eventually disappears.

with the 95% confidence level each, which is an order of magnitude improvement in precision compared to [46].

In addition, linear extrapolation of the slopes of transition lines for $N = 24, 32, 40, 50$ shows that they radiate from the triple point/origin as

$$\updownarrow\rightarrow\uparrow\downarrow: \qquad c_2 = 7.1(8)c_4, \tag{5.2.4a}$$

$$\uparrow\downarrow\rightarrow\uparrow\uparrow: \qquad c_2 = 17(1)c_4. \tag{5.2.4b}$$

This is also how the phase diagram of $\widetilde{\mathcal{S}}_0$ looks like close to the origin, while away from it, its transition lines bend into $\sim \sqrt{\widetilde{c}_4}$.

It is important to notice that even if the triple point of $\mathcal{S}_0$ does not lie precisely at the origin, the triple point of $\widetilde{\mathcal{S}}_0$ will, due to $\widetilde{c}_i(T) = c_i(T)/N$. In fact, this holds for any alternate parameter rescaling c_i/N^{ν_i} by the positive power of the cutoff. This behavior is in contrast with the $\lambda\phi^4$-model on the fuzzy sphere [45, 43]. The culprit could be in differing forms of the kinetic term, whose presence allows the $\updownarrow\rightarrow\uparrow\uparrow$ transition to develop in the first place, or in different parameter scalings.

5.3 *R*-on triple point

Coupling with curvature pushes the triple point—and with it the stripe phase—away from the origin proportionally to its strength (Figure 5.4). The simulated shift of the triple point in the $N = 24$, R-on case

$$\widetilde{c}_2(T|r) = 0.18(8) + 15.5(7)c_r \tag{5.3.5}$$

relative to the R-off value

$$\widetilde{c}_2(T|\not{r}) = 0.14(5), \tag{5.3.6}$$

agrees well with the maximal prediction allowed by (4.4.39):

$$\max \delta\widetilde{c}_2 = \left(16 - \frac{63}{2N}\right) c_r \approx 14.7c_r. \tag{5.3.7}$$

The slight overshoot due to the choice of the triple-point proxy was discussed in Section 5.1. Figure 5.3 shows that the small intercept of the $\widetilde{c}_2(T|r)$-line in Figure 5.4 (which represents the R-off triple point) goes to zero with the increase in matrix size. It is, therefore, safe to assume that proportionality to c_r becomes exact in the infinite size limit.

As we already mentioned, in the GW approach [13], renormalizability of the two-dimensional $\lambda\phi^4_\star$-model is assured by defining it as a $\Omega \to 0$ limit of the series of super-renormalizable models in which Ω itself does not renormalize and serves as a series label [61]. The Ω is chosen as

$$\frac{1-\Omega^2}{1+\Omega^2} = \sqrt{1 - \frac{1}{(1+\log(\Lambda/\Lambda_{\text{ren}}))^2}}, \tag{5.3.8}$$

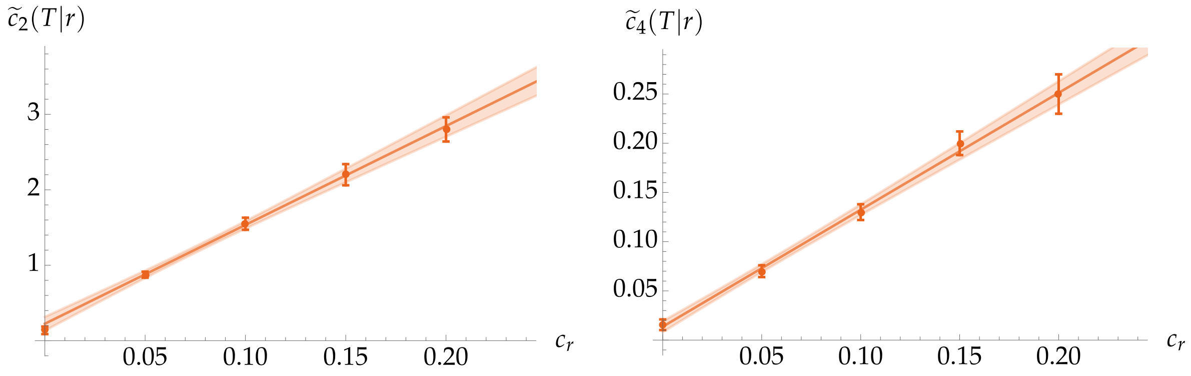

Figure 5.4: Coordinates of the triple point in the R-on case as a function of the curvature coupling: /LEFT/ $\widetilde{c}_2(T|r) = 0.18(8) + 15.5(7)c_r$, /RIGHT/ $\widetilde{c}_4(T|r) = 0.014(6) + 1.19(8)c_r$. Data gathered from specific heat C for $N = 24$.

which for large cutoff $\Lambda \sim \sqrt{N}$ switches off as

$$\Omega \sim \frac{1}{\log N}. \tag{5.3.9}$$

Since Appendix A connects Ω and c_r as

$$c_r = \frac{\Omega^2/8}{1-\Omega^2/2}, \tag{5.3.10}$$

we consider the limit where c_r decreases as

$$c_r \sim \frac{1}{\log^2 N}. \tag{5.3.11}$$

Combining this with $\delta\widetilde{c}_2 \propto c_r$ (that is: $\delta c_2 \propto N c_r$), effectively swipes the stripe phase off to infinity as

$$c_2(T) \sim \frac{N}{\log^2 N}, \tag{5.3.12}$$

leaving the limiting model with a completely different phase diagram from the one obtained by simply setting $c_r = 0$.

Looking back at the equation of motion (3.1.22) and its solutions (3.1.23), we see that the curvature term prefers the trivial over the striped vacuum. The action (3.1.2) also shows that the curvature itself compensates the attenuation of the coupling. Namely, for nearly ordered field configurations $\Phi^2 \propto \mathbb{1}$, the curvature term dominates the potential by factor

$$\frac{\operatorname{tr} R\Phi^2}{\operatorname{tr}\Phi^{2n}} \approx \frac{\operatorname{tr} R}{\operatorname{tr}\mathbb{1}} = -8N\left(1-\frac{31}{16N}\right) \sim N, \tag{5.3.13}$$

which multiplied by the coupling leads once more to the ratio

$$\frac{N}{\log^2 N}. \tag{5.3.14}$$

It is instructive to also track the behaviour of the renormalized mass parameter as we turn off the curvature coupling. As we already stated in (2.3.41), the divergent part of the mass renormalization in the R-on case is found to be:

$$\delta m^2_{\text{ren}} = \frac{\lambda}{12\pi(1+\Omega^2)} \log\frac{\Lambda^2\theta}{\Omega}, \tag{5.3.15}$$

which, adapted to our notation, gives the leading logarithmic mass divergence

$$\delta c_2^{\text{ren}} \sim -\log N. \tag{5.3.16}$$

Bare c_2 has to compensate this, and increase itself by $\left|\delta c_2^{\text{ren}}\right|$. Since this shift grows slower than (5.3.12), the bare c_2 required for the renormalization is located outside of the stripe phase—apparently, in the disordered phase.

This differs from the R-off case with T at the origin. Although we cannot directly set $\Omega = 0$ in (5.3.15), we could try to turn off Ω much faster than in the GW approach. Taking, for example,

$$\Omega \sim e^{-N}, \tag{5.3.17}$$

would give the leading divergence

$$\delta m^2_{\text{ren}} \sim \lambda N, \tag{5.3.18}$$

and

$$\delta c_2(T) \sim N e^{-2N} \to 0, \tag{5.3.19}$$

as expected in the R-off case. Thus, a suitably chosen infinitesimal $\lambda \sim 1/N$ would make the renormalization finite, leaving the bare mass inside the near-origin portion of the stripe phase for a range of physical mass choices in the perturbative regime.

5.4 Gauge model

In [23] we analyzed renormalizability of a GW-ispired gauge model on the $\mathfrak{h}^{\text{tr}}_{\epsilon}$ defined in [21, 22]. Its 3-dimensional Yang-Mills action is given by

$$S_{\text{YM}} = \frac{1}{16\text{g}^2}\,\text{tr}(\mathsf{F}(*\mathsf{F}) + (*\mathsf{F})\mathsf{F}), \tag{5.4.20}$$

where $*\mathsf{F}$ is a Hodge dual of the field strength F. After Kaluza-Klein-like reduction to $z = 0$ subspace and transition to 2-dimensional coupling g and fields A_α, the action reads,

$$\begin{aligned} S_{\text{YM}} = \frac{1}{2}\text{tr}\Big(&(1-\epsilon^2)(F_{12})^2 + (D_1\phi)^2 + (D_2\phi)^2 + (5-\epsilon^2)\mu^2\phi^2 \\ &- 2(1-\epsilon^2)\mu F_{12}\phi - 4\epsilon F_{12}\phi^2 - \epsilon^2\{p_1 + igA_1, \phi\}^2 - \epsilon^2\{p_2 + igA_2, \phi\}^2\Big) \end{aligned} \tag{5.4.21}$$

or expressed in terms of covariant coordinates

$$\mathsf{X}_\alpha = p_\alpha + ig\mathsf{A}_\alpha = p_\alpha + igA_\alpha, \tag{5.4.22}$$

it becomes

$$S_{\mathrm{YM}} = \frac{1}{2}\mathrm{tr}\Big((1-\epsilon^2)[\mathsf{X}_1,\mathsf{X}_2]^2 + (1-\epsilon^2)\mu^2\phi^2 - 2(1-\epsilon^2)\mu^3\phi + 2i(1-\epsilon^2)\mu[\mathsf{X}_1,\mathsf{X}_2]\phi$$
$$+ 4i\epsilon[\mathsf{X}_1,\mathsf{X}_2]\phi^2 + [\mathsf{X}_1,\phi]^2 + [\mathsf{X}_2,\phi]^2 - \epsilon\{\mathsf{X}_1,\phi\}^2 - \epsilon\{\mathsf{X}_2,\phi\}^2\Big). \tag{5.4.23}$$

Covariant derivatives D_α and field strength F_{12} are given by:

$$D_\alpha\phi = [\mathsf{X}_\alpha,\phi], \qquad F_{12} = [p_1, A_2] - [p_2, A_1] + ig[A_1, A_2]. \tag{5.4.24}$$

The compactification turned the z-component of the gauge field A_3 into a scalar field ϕ. Apart from the interaction with A_1 and A_2, there is a coupling of the scalar field and the curvature, hidden within the $\{p_\alpha,\cdot\}$-term:

$$-\frac{\epsilon^2}{2}\,\mathrm{tr}\,\{p_\alpha + igA_\alpha,\phi\}^2 \to -\epsilon^2\,\mathrm{tr}\Big(p_\alpha^2\phi^2\Big) = -\frac{1}{8}\,\mathrm{tr}\left(\left(R - \frac{11}{2}\mu^2\right)\phi^2\right). \tag{5.4.25}$$

This also shifts the mass of the field, however the total mass term for the scalar field stays positive:

$$\frac{1}{2}\,\mathrm{tr}\left(\left(\frac{51}{8}-\epsilon^2\right)\mu^2\phi^2\right) > \frac{1}{2}\,\mathrm{tr}\left(\left(\frac{51}{8}-1\right)\mu^2\phi^2\right) = \frac{43}{16}\mu^2\,\mathrm{tr}\,\phi^2. \tag{5.4.26}$$

At first glance, the model looks like a gauged version of the GW model.

Equations of motion for this action, $\delta S_{\mathrm{YM}}/\delta\phi = 0$ and $\delta S_{\mathrm{YM}}/\delta A_\alpha = 0$ are respectively [21]:

$$-(1-\epsilon^2)\mu F_{12} + (5-\epsilon^2)\mu^2\phi + 2i\epsilon g\{F_{12},\phi\} - D^\alpha D_\alpha\phi - \epsilon^2\{\mathsf{X}^\alpha,\{\mathsf{X}_\alpha,\phi\}\} = 0, \tag{5.4.27a}$$

$$(1-\epsilon^2)\epsilon^{\alpha\beta}D_\beta(F_{12}-\mu\phi) + 2i\epsilon g\epsilon^{\alpha\beta}\{D_\beta\phi,\phi\} - g[D^\alpha\phi,\phi] - \epsilon^2 g\{\{\mathsf{X}^\alpha,\phi\},\phi\} = 0. \tag{5.4.27b}$$

They lead to two classical vacua, the trivial one,

$$A_1 = 0, \qquad A_2 = 0, \qquad \phi = 0, \tag{5.4.28}$$

and the one that breaks the translational invariance

$$A_1 = -\frac{\mu^2 y}{\epsilon g}, \qquad A_2 = +\frac{\mu^2 x}{\epsilon g}, \qquad \phi = \frac{\mu}{\epsilon g}; \tag{5.4.29}$$

the latter corresponds to zero values of covariant coordinates X_α. Classically, both vacua have the same energy and correspond to $S_{\mathrm{YM}} = 0$.

In the matrix variant of the model, coordinates x and y would once more become the matrices X and Y of the truncated Heisenberg algebra, whose eigenspectrum consists of pairs of opposite-signed eigenvalues, thus constituting a modified version of the stripe phase, similar to the situation in Figure 4.7. As we can see, vacuum (5.4.29) transforms into (5.4.28) when we let $g \to \infty$. This implies a possible structure of the phase diagram of the gauge model: the stripe phase for weak interaction and the disordered phase for strong interaction. Such a structure agrees with the phase diagrams in Figures 4.12 and 4.13, where ordered phases lie at smaller quartic coupling than the disordered phase.

In [23] we calculated the one-loop divergent corrections to the $\phi\phi$ and AA propagators and found the following additional non-local derivative terms

$$\int \phi \Box^{-2} \phi, \quad \int \phi \Box^{-1} \phi, \quad \int A_\mu \Box^{-2} A^\mu. \tag{5.4.30}$$

We have not calculated the ϕA one-loop divergences, but from symmetry, we expect that there are non-vanishing non-local corrections in this sector too. Unfortunately, these divergences render the model nonrenormalizable. It would be interesting to connect the nonrenormalizability to the retention of the stripe phase in the bare coupling phase diagram of the model, which could be a topic for future research.

Upon a closer look, g can enter the definition of the field and, by setting $g = 1$, completely disappear from the equations in this section. This removal leads to another possible conclusion: the entire model lies in the striped phase for all values of g.

Using the same convention, we can also add the topological Chern-Simons term to the YM action [21]:

$$S_{\mathrm{CS}} = \frac{\alpha\mu}{3} \operatorname{tr} \left(-i(3-\epsilon^2) \left(F_{12} - \frac{\mu^2}{\epsilon} \right) + \frac{2\epsilon}{3} \mathrm{X}^\alpha \mathrm{X}_\alpha \left(\phi - \frac{\mu}{2\epsilon} \right) \right). \tag{5.4.31}$$

After inclusion of this term, the trivial vacuum solution disappears, leaving generically just the striped vacuum (5.4.28) with $S_{\mathrm{CS}} = 0$. However, for a special choice of parameters $\epsilon = 1$, $\alpha = 6$, another solution of EOM appears:

$$A_1 = A_2 = 0, \qquad \phi = \mu. \tag{5.4.32}$$

This one restores the translational invariance and it has a lower energy than the striped vacuum:

$$S_{\mathrm{YM}} + S_{\mathrm{CS}} = 2\mu^4 \operatorname{tr} \left(\mathbb{1} - \frac{2\mu^2}{3}(X^2 + Y^2) \right) \sim -N^2 < 0, \tag{5.4.33}$$

so it is possible that it represents the true vacuum of the system. Its one downside is non-propagating kinetic term. It would be interesting to see if the system goes through a phase transition around this particular value of α, and whether the CS-term helps with renormalization.

Chapter 6

Conclusions and outlook

This thesis explores the phase structure of matrix models that regularize quantum field theories on NC spaces. It was guided by the hypothesis that the renormalizability of NC models is connected to the existence and the extension of the NC striped phase. More specifically, we showed that the renormalizability of the two-dimensional $\lambda\phi^4_{\mathrm{GW}}$ model obtained as a limit of GW models with slowly decaying harmonic potential/curvature coupling is correlated to the absence of the striped phase in its phase diagram.

In order to make use of numerical simulations, we worked with a matrix model where the Hermitian field is coupled to the curvature of $\mathfrak{h}^{\mathrm{tr}}$. We compared the behavior of this matrix model with and without the curvature term. In the large N limit, these cases respectively represent the $\lambda\phi^4_\star$ model on $\mathbb{R}^2_\theta$ (Figure 4.12), which is not renormalizable due to UV/IR mixing, and the GW model (Figure 4.13) which is renormalizable.

We found that the curvature term shifts the phase transition lines towards larger values of the mass parameter proportionally to the product of the curvature coupling c_r and the matrix size N. Since the GW model turns off c_r as $1/\log^2 N$, their combined effect is that the striped phase is pushed into infinity and removed from the phase diagram. At the same time, the bare mass parameter necessary for the renormalization stays in the disordered phase. The nonrenormalizable $\lambda\phi^4_\star$ model with the stripe phase tethered to the origin of the parameter space is thus replaced by the $\lambda\phi^4_{\mathrm{GW}}$ model without the striped phase.

While inspecting the scaling of the curvature term, we confirmed that it alters both eigenvalue distribution and the border of the $\uparrow\downarrow$-phase. This is particularly apparent for small values of the quartic coupling. In this regime, there seems to exist a new "phase" located between $\updownarrow$ and $\uparrow\uparrow$ phases, in which the curvature eigenvalues activate one by one with the increase of the mass parameter. It remains for future research to inspect its properties more closely and to determine whether or not it survives the large N limit.

To reach the conclusions about the large N limit of the phase diagrams, it was important to compare and connect the variants of the model both with the original and the scaled parameters. The original parameters essentially correspond to the GW model, and the scaled parameters give the infinity of the phase diagram and are related to the renormalization group flow. As for determining the extent of the stripe phase connected to the UV/IR mixing, we tracked the position of the triple point. It is where the stripe phase starts,

Table 6.1: Comparison of the renormalizability and the phase structure across models. The mass renormalization shift and the triple point shift are given for the unscaled model parameters.

space	model	mass shift	triple point shift	starting phase	renormalizable
$\mathbb{R}^2_\theta$, $\mathfrak{h}^{\mathrm{tr}}$	$\lambda\phi^4_\star$	UV/IR	0	↑↓	no
$\mathbb{R}^2_\theta$, $\mathfrak{h}^{\mathrm{tr}}$	GW	$\log N$	N	↕	yes
$\mathbb{R}^2_\theta$, $\mathfrak{h}^{\mathrm{tr}}$	$\lambda\phi^4_{\mathrm{GW}}$	$\log N$	$N/\log^2 N$	↕	yes
$\mathfrak{h}^{\mathrm{tr}}_\epsilon$	$U(1)$		one phase?	↑↓?	no
S^2_N	$\lambda\phi^4_\star$	$\log N$	$N^{3/2}$	↕	yes

spreading towards larger values of the mass and quartic parameters. The triple point was also crucial for the unambiguous identification of regions of the scaled and unscaled phase diagrams.

In the course of our research, we have shown that the existing numerical methods are sufficient to draw meaningful conclusions about the qualitative and quantitative aspects of the phase transitions in the GW model. The Hybrid Monte Carlo method fared particularly well in the ↕-phase and near the ↕ → ↑↓ transition line but showed limitations for large matrices in ↑↓ and ↑↑ phases, where the simulation showed a tendency for being trapped in deep potential wells around the false vacua. These limitations can be overcome either by drastically increasing the available computing resources and the simulation times or by devising new algorithms. Throughout the simulations, we worked with matrices of sizes up to $N = 70$, but the most detailed phase diagrams were produced for $N = 24$. It would be nice to confirm the behavior of our model for larger matrix sizes, possibly by exploiting the computing powers of GPUs.

On the analytical side, we have used HCIZ integral to obtain the effective action for a sub-model without the kinetic term and then successfully solved the eigenvalue distribution equation to predict the position of the ↕ → ↑↓ transition line. However, the analytical treatment of the kinetic term remains a challenge.

There are several promising lines of future investigation. First, there is the numerical simulation of the mentioned GW-inspired gauge model on $\mathfrak{h}^{\mathrm{tr}}_\epsilon$, in the hope of confirming its nonrenormalizability is due to the presence of the stripe phase that comes from its additional stripe-like vacuum. Then, there is a simulation of the renormalizable spinor model on $\mathfrak{h}^{\mathrm{tr}}$ [75] in the context of fermionic matrix models [76, 77]. Finally, we could repeat the analysis of the GW model in 4 dimensions.

Table 6.1 lists the unscaled mass renormalization shifts and the triple point shifts for the models investigated in this thesis, as well as for the gauge model on $\mathfrak{h}^{\mathrm{tr}}_\epsilon$ and the scalar model on S^2_N. Among the numbered models, the nonrenormalizable feature or indicate the presence of the ↑↓-phase. On the other hand, the ↑↓-phase is absent in the renormalizable models, where the renormalization starts in the ↕-phase. The list supports our view that the correlation between the ↑↓-phase and the renormalizability is a more general phenomenon and not just confined to our specific model. If this correspondence persists across more models, it would even be helpful for the construction of new ones. A simulation of a sparse phase diagram would then assess the new model's renormalizability potential before embarking on an involved and time-consuming analytical exploration.

Appendix A

Model correspondence

According to [41], mapping

$$\phi \longleftrightarrow \Phi, \qquad \int \longleftrightarrow \sqrt{\det 2\pi\theta}\,\mathrm{tr} \tag{A.1}$$

connects field theory on Moyal space and matrix field theory with the same parameters. Also, [16] provides a correspondence between S_{GW} and $S_{\mathfrak{h}}$:

$$S_{\mathrm{GW}} = \left(1 - \frac{\Omega^2}{2}\right) S_{\mathfrak{h}}, \tag{A.2a}$$

$$m^2 = \left(1 - \frac{\Omega^2}{2}\right) \left(m_{\mathfrak{h}}^2 - \frac{15}{2}\xi\mu^2\right), \tag{A.2b}$$

$$\lambda = \left(1 - \frac{\Omega^2}{2}\right) \lambda_{\mathfrak{h}}, \tag{A.2c}$$

$$\Omega^2 = 8\epsilon^2 \left(1 - \frac{\Omega^2}{2}\right) \xi. \tag{A.2d}$$

From these, by comparing (2.3.44) and (3.1.2), it is easy to conclude that S_{GW} and S_N are connected by

$$S_{\mathrm{GW}} = \pi \left(1 - \frac{\Omega^2}{2}\right) S_N, \tag{A.3a}$$

$$m^2 = -\left(1 - \frac{\Omega^2}{2}\right) \left(c_2 + \frac{15}{2}c_r\right), \tag{A.3b}$$

$$\lambda = 12 \left(1 - \frac{\Omega^2}{2}\right) c_4, \tag{A.3c}$$

$$\Omega^2 = 8 \left(1 - \frac{\Omega^2}{2}\right) c_r, \tag{A.3d}$$

in the large N limit ($\theta^{12} = 1/\mu^2$, units: $\mu = 1$).

Furthermore, action multiplier can be absorbed into the field during expectation value integration of the observable $\mathcal{O}$

$$\langle \mathcal{O} \rangle_S = \frac{\displaystyle\int \mathrm{d}\Phi \, \mathcal{O} \, e^{-S}}{\displaystyle\int \mathrm{d}\Phi \, e^{-S}}, \tag{A.4}$$

and will affect only c_4:

$$\langle \kappa S(c_2, c_4, c_r) \rangle_{\kappa S} = \langle S(c_2, c_4/\kappa, c_r) \rangle_S \,, \tag{A.5a}$$

$$\sqrt{\kappa} \, \langle \Phi \rangle_{\kappa S} \, (c_2, c_4, c_r) = \langle \Phi \rangle_S \, (c_2, c_4/\kappa, c_r), \tag{A.5b}$$

yielding

$$C_{\kappa S}(c_2, c_4, c_r) = C_S(c_2, c_4/\kappa, c_r), \tag{A.6a}$$

$$\kappa \chi_{\kappa S}(c_2, c_4, c_r) = \chi_S(c_2, c_4/\kappa, c_r). \tag{A.6b}$$

Since we are interested in the position of peaks of C and χ, this means that phase transition diagrams for κS and S will be the same up to a reparametrization

$$(c_2, c_4, c_r) \longleftrightarrow (c_2, c_4/\kappa, c_r). \tag{A.7}$$

For phase diagrams of S_{GW} and $\mathcal{S}$ in the $\Omega \to 0$ limit ($c_r \to 0$), this means:

$$(m^2, \lambda) \longleftrightarrow (-c_2, {}^{12}/_{\pi} \, c_4). \tag{A.8}$$

Appendix B

Eigenvalue distributions

As already mentioned, the shape of the field eigenvalues distribution is intimately connected with the phases of the model. Namely, one-cut symmetric distribution corresponds to the disordered phase, two-cut (a)symmetric to the striped phase, and one-cut asymmetric to the ordered phase. The change in the connectedness of the distribution support indicates the point of phase transition. The switch from the one-cut to two-cut regimes determines the transition boundary between the disordered and ordered phases.

We will now explore the analytical aspects of finding the eigenvalue distributions on the well-studied example of the PP model.

First, let us take another look at the more general GW model

$$S_{\mathrm{GW}}(\Phi) = N\ \mathrm{tr}\Big(\Phi\widetilde{\mathcal{K}}\Phi - c_r\widetilde{R}\Phi^2 - \widetilde{c}_2\Phi^2 + \widetilde{c}_4\Phi^4\Big)\,, \tag{B.1}$$

where tildes denote the necessary scaling of the operators and parameters that (mostly) removes their N-dependence so that each term's $O(N^2)$ contribution comes from the trace and the prefactor N. If we are interested in expectation values and probability distributions of eigenvalue-dependent observables $\mathcal{O}$

$$\langle\mathcal{O}(\Lambda)\rangle = Z^{-1}\int \mathrm{d}\Phi\,\mathcal{O}(\Lambda)\,e^{-S_N(\Phi)}, \qquad Z = \int \mathrm{d}\Phi\,e^{-S_N(\Phi)}, \tag{B.2}$$

we should integrate out the non-eigenvalue degrees of freedom in the path integral. Since all hermitian matrices can be written in an radial-angular decomposition

$$\Phi = U\Lambda U^\dagger, \qquad \Lambda = \mathrm{diag}\,\lambda_i, \qquad UU^\dagger = U^\dagger U = \mathbb{1}, \tag{B.3}$$

where Λ is matrix of eigenvalues of Φ and U some unitary matrix, the action becomes

$$S_N(\Lambda, U) = N\ \mathrm{tr}\Big((U\Lambda U^\dagger)\widetilde{\mathcal{K}}(U\Lambda U^\dagger) - c_r\widetilde{R}U\Lambda^2U^\dagger - \widetilde{c}_2\Lambda^2 + \widetilde{c}_4\Lambda^4\Big)\,. \tag{B.4}$$

We can define an effective eigenvalue action $S_N(\Lambda)$ as

$$Z = \int \mathrm{d}\Phi\,e^{-S_N(\Phi)} = \int \mathrm{d}U\mathrm{d}\Lambda\,\Delta^2(\Lambda)\,e^{-S_N(\Lambda,U)} = \int \mathrm{d}\Lambda\,e^{-S_N(\Lambda)}, \tag{B.5}$$

where Vandermonde determinant $\Delta(\Lambda)$

$$\Delta(\Lambda) = \prod_{1 \leq i < j \leq N} (\lambda_j - \lambda_i) \tag{B.6}$$

appears as Jacobian due to the change of variables $\Phi \to (\Lambda, U)$ and adds a logarithmic eigenvalue repulsion term to the effective action. The exponential integrand now represents the probability distribution $\rho(\Lambda)$ of the field's eigenvalues

$$\rho(\Lambda) = \frac{e^{-S_N(\Lambda)}}{Z}, \tag{B.7}$$

which can be easily measured during the simulation. The expectation values can now be rewritten as

$$\langle \mathcal{O}(\Lambda) \rangle = \int \mathrm{d}\Lambda \, \mathcal{O}(\Lambda) \, \rho(\Lambda). \tag{B.8}$$

We can find the equation for ρ using the saddle-point approximation:

$$\frac{\partial S(\Lambda)}{\partial \lambda_i} = 0. \tag{B.9}$$

This can be rewritten as

$$\frac{\partial V_N(\Lambda)}{\partial \lambda_i} = \frac{2}{N} \sum_{j \neq i} \frac{1}{\lambda_i - \lambda_j}, \tag{B.10}$$

where $V_N(\Lambda)$ is $S_N(\Lambda)$ without the Vandermonde contribution which ends up on the right-hand side of the equation. Since, due to trace,

$$V_N(\Lambda) = \sum_i V(\lambda_i), \tag{B.11}$$

in the large N continuous limit

$$\lambda_i \to \lambda, \qquad \lambda_j \to \lambda', \qquad \frac{1}{N} \sum \to \int, \tag{B.12}$$

(B.10) becomes

$$\frac{V'(\lambda)}{2} = \underset{\text{support}}{⨍} \mathrm{d}\lambda' \, \frac{\rho(\lambda')}{\lambda - \lambda'}, \tag{B.13}$$

If we look at the (B.4), we see that integration of the PP part of the action is trivial since it depends only on λ,

$$V_{\mathrm{PP}}(\lambda) = -\widetilde{c}_2 \lambda^2 + \widetilde{c}_4 \lambda^4, \tag{B.14}$$

while kinetic and curvature terms in general present a challenge. One possible approach for the kinetic term on the fuzzy sphere can be found in [33]. We can now try to solve (B.13) for the PP model

$$-\widetilde{c}_2 \lambda + 2\widetilde{c}_4 \lambda^3 = \int_{\text{support}} \mathrm{d}\lambda' \, \frac{\rho(\lambda')}{\lambda - \lambda'}, \tag{B.15}$$

closely following the approach outlaid in [72]. From this point on, we will write $\int$ instead of $⨍$ and invoke the principal value where necessary.

One-cut symmetric distribution

If we chose even distribution on $[-R, R]$ to match the even potential, we can write

$$\begin{aligned}-\widetilde{c}_2\lambda + 2\widetilde{c}_4\lambda^3 &= \int\limits_{-R}^{0} \mathrm{d}\lambda' \frac{\rho(\lambda')}{\lambda-\lambda'} + \int\limits_{0}^{R} \mathrm{d}\lambda' \frac{\rho(\lambda')}{\lambda-\lambda'} = -\int\limits_{R}^{0} \mathrm{d}\lambda' \frac{\rho(-\lambda')}{\lambda+\lambda'} + \int\limits_{0}^{R} \mathrm{d}\lambda' \frac{\rho(\lambda')}{\lambda-\lambda'} \\ &= \int\limits_{0}^{R} \mathrm{d}\lambda' \frac{\rho(\lambda')}{\lambda+\lambda'} + \int\limits_{0}^{R} \mathrm{d}\lambda' \frac{\rho(\lambda')}{\lambda-\lambda'} = \int\limits_{0}^{R} \mathrm{d}\lambda' \frac{2\lambda\rho(\lambda')}{\lambda^2-\lambda'^2}, \qquad \text{(B.16)}\end{aligned}$$

or, for $\lambda \neq 0$,

$$2\widetilde{c}_4\lambda^2 - \widetilde{c}_2 = 2\int\limits_{0}^{R} \mathrm{d}\lambda' \frac{\rho(\lambda')}{\lambda^2-\lambda'^2}. \qquad \text{(B.17)}$$

Using reparametrization

$$t = 2\widetilde{c}_4\lambda^2 - \widetilde{c}_2, \qquad f(t') = \frac{\rho(\lambda'(t'))}{\lambda'(t')}, \qquad \text{(B.18)}$$

we directly obtain

$$t = \int\limits_{t_-}^{t_+} \mathrm{d}t' \frac{f(t')}{t-t'}, \qquad \text{(B.19)}$$

integral limits being

$$t_\pm = 2\widetilde{c}_4 R_\pm^2 - \widetilde{c}_2, \qquad \text{(B.20)}$$

where $(R_-, R_+) = (0, R)$ for distribution with connected support, and $R_+ > R_- > 0$ for disconnected support.

For the connected distribution, the solution of this equation takes the form

$$f(t) = \frac{1}{\pi}\sqrt{\left|\frac{t-t_+}{t-t_-}\right|}\left(t + \frac{t_+-t_-}{2}\right), \qquad \text{(B.21)}$$

that is

$$\rho_{\updownarrow}(\lambda) = \frac{\widetilde{c}_4(R^2+2\lambda^2) - \widetilde{c}_2}{\pi}\sqrt{R^2-\lambda^2}, \qquad \text{(B.22)}$$

where radius R,

$$R^2 = \frac{\widetilde{c}_2 + \sqrt{\widetilde{c}_2^2 + 12\widetilde{c}_4}}{3\widetilde{c}_4}, \qquad \text{(B.23)}$$

is obtained from the probability normalization

$$\int\limits_{-R}^{+R} \rho(\lambda)\mathrm{d}\lambda = 1. \qquad \text{(B.24)}$$

It can be easily checked that the height of the distribution's midpoint at $\lambda = 0$ decreases as

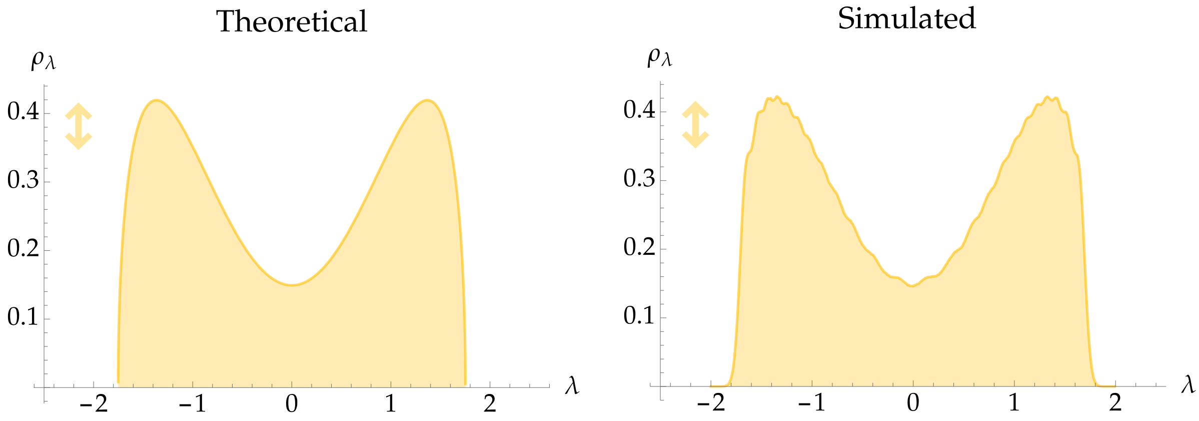

Figure B.1: Theoretical vs. simulated ($N = 24$) eigenvalue distribution for the PP model at $(\widetilde{c}_2, \widetilde{c}_4) = (0.10, 0.01)$. Eigenvalues are expressed in units of $\sqrt{\widetilde{c}_2/(2\widetilde{c}_4)}$.

we increase $\widetilde{c}_2$. The condition that distribution is positive at its minimum at $\lambda = 0$, gives the constraint

$$\widetilde{c}_2 < 2\sqrt{\widetilde{c}_4}, \tag{B.25}$$

the critical value $\widetilde{c}_2 = 2\sqrt{\widetilde{c}_4}$ corresponding to a phase transition from the one-cut to the two-cut phase.

The maximum probability eigenvalues are not always 0, as we might naively expect, since the distribution has a local minimum at this value for $\widetilde{c}_2 > 0$. Instead, they lie at $\lambda = 0$ or at

$$\lambda^2 = \frac{2\widetilde{c}_2 + \sqrt{\widetilde{c}_2^2 + 12\widetilde{c}_4}}{6\widetilde{c}_4} = R^2 - \frac{\sqrt{\widetilde{c}_2^2 + 12\widetilde{c}_4}}{6\widetilde{c}_4} < R^2. \tag{B.26}$$

The second derivative condition for the distribution's maximum is

$$\rho''(\lambda) < 0 \;\Rightarrow\; 4\lambda^4 - 6R^2\lambda^2 + R^2\left(R^2 + \frac{\widetilde{c}_2}{3\widetilde{c}_4}\right) < 0, \tag{B.27}$$

and we see that $\lambda = 0$ solves it only when

$$R^2 + \frac{\widetilde{c}_2}{3\widetilde{c}_4} < 0 \;\Leftrightarrow\; 2\widetilde{c}_2 + \sqrt{\widetilde{c}_2^2 + 12\widetilde{c}_4} < 0, \tag{B.28}$$

that is

$$\widetilde{c}_2 < -2\sqrt{\widetilde{c}_4}. \tag{B.29}$$

Only then the field truly oscillates around $\mathbb{0}$ value.

Two-cut symmetric distribution

For the disconnected distribution, a solution symmetric around the origin is

$$f(t) = \frac{1}{2\pi}\sqrt{(t_+ - t_-)^2 - 4t^2}, \tag{B.30}$$

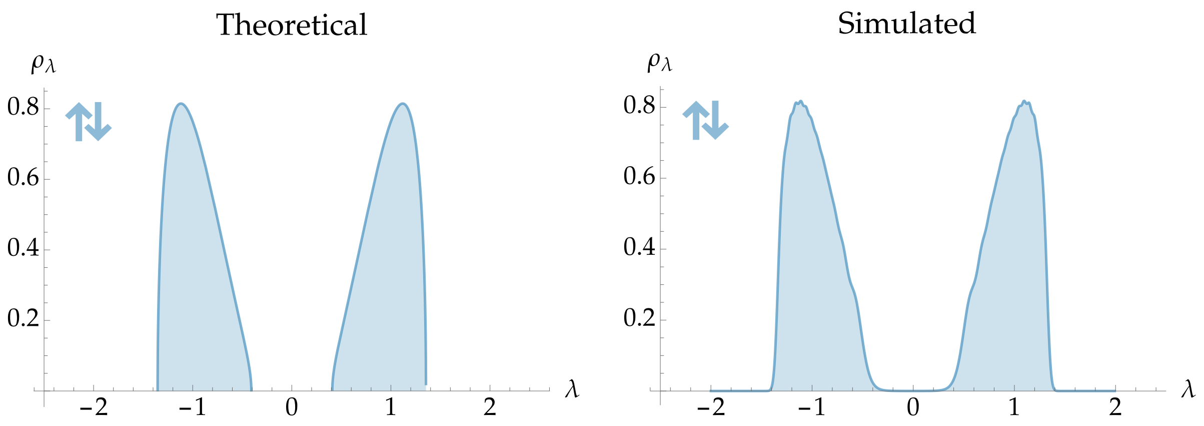

Figure B.2: Theoretical vs. simulated ($N = 24$) eigenvalue distribution for the PP model at $(\tilde{c}_2, \tilde{c}_4) = (0.24, 0.01)$. Eigenvalues are expressed in units of $\sqrt{\tilde{c}_2/(2\tilde{c}_4)}$.

that is

$$\rho_{\uparrow\downarrow}(\lambda) = \frac{2\tilde{c}_4|\lambda|}{\pi}\sqrt{(R_+^2-\lambda^2)(\lambda^2-R_-^2)}. \tag{B.31}$$

Normalization once more leads to expressions for radii

$$R_\pm^2 = \frac{\tilde{c}_2 \pm 2\sqrt{\tilde{c}_4}}{2\tilde{c}_4}. \tag{B.32}$$

We see that for $\tilde{c}_2 = 2\sqrt{\tilde{c}_4}$, the inner radius R_- collapses to zero, as it should.

The distribution's maximum lies at

$$\lambda^2 = \frac{R_+^2 + R_-^2 + \sqrt{(R_+^2 - R_-^2)^2 + R_+^2 R_-^2}}{3}. \tag{B.33}$$

For $R_+/R_- \gg 1$, which happens near the phase transition where $R_- = 0$, this yields

$$\lambda \approx \sqrt{\frac{2}{3}}R_+ \approx 0.82R_+. \tag{B.34}$$

Far away from it, for large $\tilde{c}_2$, radii become nearly equal, and distribution centers tightly around $\tilde{c}_2/(2\tilde{c}_4)$, which is a trace of square of the non-trivial EOM solution divided by N.

We can use the derived expressions for eigenvalue distributions to calculate the thermodynamical quantities and compare them with their simulated counterparts. Let us calculate C from these distributions. Since C involves the variance of S, we should start with $\langle S\rangle$

$$\langle S\rangle = \int \mathrm{d}\lambda\, \rho(\lambda)S(\lambda). \tag{B.35}$$

Using *Mathematica*, it is simple to obtain the action averages

$$\langle S\rangle_\updownarrow = \frac{R^4}{64}\left(8\tilde{c}_2^2 - 20\tilde{c}_2\tilde{c}_4R^2 + 9\tilde{c}_4^2R^4\right), \qquad \langle S\rangle_{\uparrow\downarrow} = \frac{1}{4} - \frac{\tilde{c}_2^2}{4\tilde{c}_4}. \tag{B.36}$$

However, $\left\langle S^2 \right\rangle$ is not equal to

$$\langle S^2 \rangle \neq \int \mathrm{d}\lambda\, \rho(\lambda)(S(\lambda))^2, \tag{B.37}$$

since S^2 includes powers and products of traces, so it does not have the form

$$\sum_i S^2(\lambda_i). \tag{B.38}$$

This prevents us from directly finding $\operatorname{Var} S$, but can be circumvented if we introduce a "temperature" T

$$\langle S(T) \rangle = \frac{1}{Z} \int \mathrm{d}\Phi\, S e^{-S/T}, \tag{B.39}$$

find $C(T)$ as its derivative,

$$C(T) = \frac{\partial \langle S(T) \rangle}{\partial T} = \frac{\operatorname{Var} S}{T^2}, \tag{B.40}$$

and then set $T = 1$. In order to exploit (B.36), we can absorb the temperature into the parameters, $c_i \to c_i/T$, calculate the expectation value with respect to the new parameters, and then multiply the result with T:

$$\langle S(T) \rangle = \langle S(c_i) \rangle_{S(c_i/T)} = \langle T S(c_i/T) \rangle_{S(c_i/T)} = T \langle S(c_i/T) \rangle . \tag{B.41}$$

We now easily obtain the expressions (4.2.12) for specific heat.

One-cut asymmetric distribution

There is a third, one-cut asymmetric solution [43, 47] which corresponds to the $\uparrow\uparrow$-phase:

$$\rho_{\uparrow\uparrow}(\lambda) = \frac{8\widetilde{c}_4\lambda^2 + 4\widetilde{c}_4(r_+ + r_-)\lambda + \widetilde{c}_4(3r_+^2 + 2r_+r_- + 3r_-^2) - 4\widetilde{c}_2}{4\pi} \times \\ \times \sqrt{(r_+ - \lambda)(\lambda - r_-)}. \tag{B.42}$$

Its radii $r_\pm$ are given by

$$r_\pm = \sqrt{\frac{3\widetilde{c}_2 + 2\sqrt{\widetilde{c}_2^2 - 15\widetilde{c}_4}}{10\widetilde{c}_4}} \pm \sqrt{\frac{2\widetilde{c}_2 - 2\sqrt{\widetilde{c}_2^2 - 15\widetilde{c}_4}}{15\widetilde{c}_4}}, \tag{B.43}$$

where the first term represents the center of the distribution support and the second term its half-width. There is also a mirror solution for negative eigenvalues. Obviously, this solution only exists when

$$\widetilde{c}_2 > \sqrt{15\widetilde{c}_4}, \tag{B.44}$$

but it is not realized since it is energetically unfavorable compared to the other two. The explicit expressions for free energies of all three solutions can be found in [43, 47]. Addition of the kinetic term, however, raises the energies of the other two solutions, allowing the $\uparrow\uparrow$-phase to appear.

Appendix C

Critical exponents and transition order

R-off case

We performed more detailed analysis of the large matrix transition limit at 3 points, corresponding to the clear two-phase regime* ($\widetilde{c}_4 = 0.0001$), to the clear three-phase regime ($\widetilde{c}_4 = 1.0$) and to the phase coexistence regime near the triple point ($\widetilde{c}_4 = 0.01$).

To determine the universality class of our model's transitions we used the standard technique of finite-size scaling. Mass parameter played the role of temperature and we defined reduced temperature t near the critical $\widetilde{c}_2^*$ as

$$t = 1 - \frac{\widetilde{c}_2}{\widetilde{c}_2^*}. \tag{C.1}$$

In a nutshell, near the transition, we consider the scalable part Q_s of quantity Q to change as

$$Q_s(t) = N^{\epsilon_Q/\nu} \widetilde{Q}_s(tN^{1/\nu}), \tag{C.2}$$

ϵ_Q being its critical exponent, and ν the critical exponent of the correlation length. Unknown functions $\widetilde{Q}_s$ can be determined by varying $\widetilde{c}_2^*$, ν and exponents ϵ_Q until data for different N collapse onto the same curve in some vicinity of the critical point. Also, if Q peaks at the critical point, we can fit

$$Q_{\max} \sim N^{\epsilon_Q/\nu}, \tag{C.3}$$

while the position of the maximum $\widetilde{c}_2^*(N)$ approaches the true critical point as

$$\widetilde{c}_2^*(N) - \widetilde{c}_2^* \sim 1/N^{1/\nu}. \tag{C.4}$$

Following the convention, we denote the exponents of C, M and χ as α, $-\beta$ and γ, respectively.

In [78], mixed order transitions are considered. They are classified as (m, m') by the

---

*Although not visible for the largest N we used at $\widetilde{c}_4 = 0.0001$, the triple-point tracking in Section 5.2 and Appendix F predicts that this $\updownarrow \to \uparrow\uparrow$ regime disappears in the large N limit.

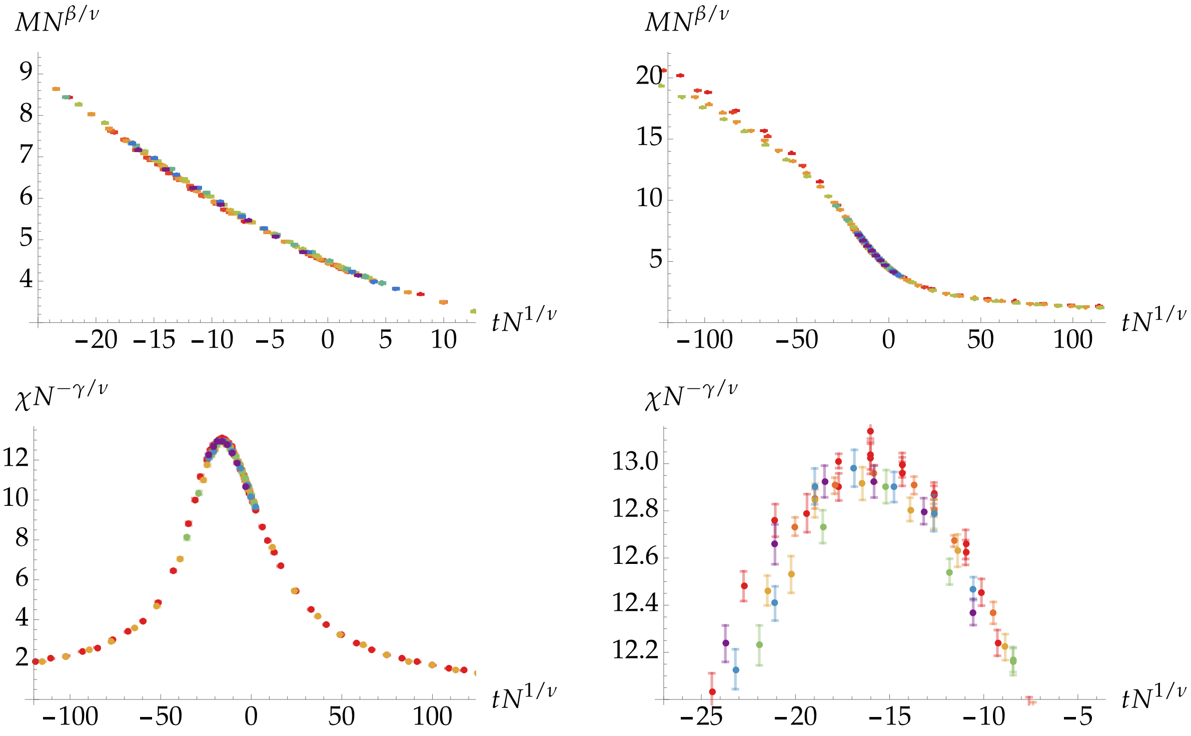

Figure C.1: Collapsed diagrams for $\updownarrow \to \uparrow\uparrow$ transition at $\tilde{c}_4 = 0.0001$. Critical exponents are $\nu = 1.00(2)$, $\beta = 0.40(2)$ and $\gamma = 0.05(1)$. Different colors represent different matrix sizes up to $N = 50$.

lowest order temperature and magnetic field derivatives

$$\frac{\partial^m}{\partial T^m}, \qquad \frac{\partial^{m'}}{\partial M^{m'}} \tag{C.5}$$

of free energy that exhibit singular behavior. In general, m and m' can differ. Let A and G be generalizations of the critical exponents α and γ. In a space of dimension d, the $m = m'$ transition satisfies [78]

$$(m-1)A + m\beta + G = m(m-1), \qquad m - A = \nu d. \tag{C.6}$$

In the case of 2nd order transition, the first relation reduces to a familiar constraint

$$\alpha + 2\beta + \gamma = 2. \tag{C.7}$$

The second relation implies that when there is a discontinuity in derivative ($A = 0$), it must hold

$$\nu = \frac{m}{d}. \tag{C.8}$$

In Figure C.1, we see collapsed data for $\updownarrow \to \uparrow\uparrow$ transition at $\tilde{c}_4 = 0.0001$. One might expect it to belong to the Ising universality class, and indeed shapes of χ and M look promising. However, as we can see in Table C.1, their critical exponents differ. The transition appears to be weakly of $(3,2)$-order, since C remains finite and χ weakly diverges. Specific heat exhibits the familiar kink around its asymptotic value 0.5. For larger matrices even this is hidden by errorbars and C appears constant $C \approx 0.50(1)$. In the infinite limit it could develop

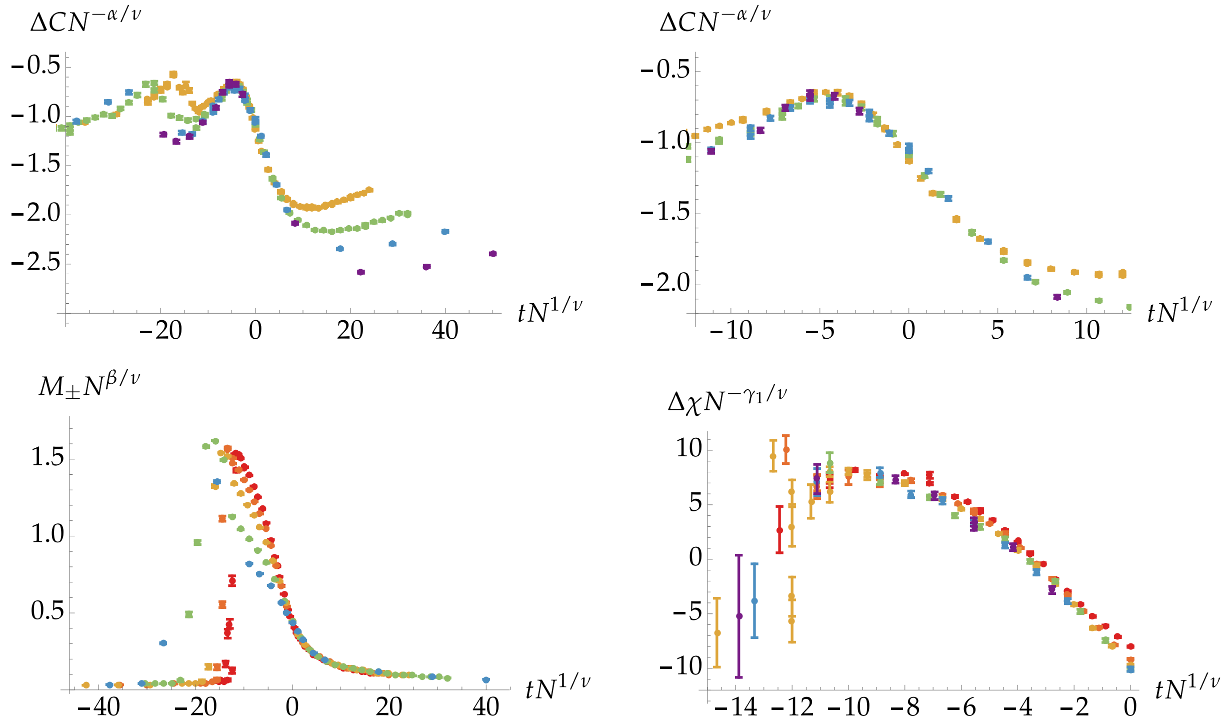

Figure C.2: Collapsed diagrams for $\updownarrow \to \uparrow\downarrow$ transition at $\widetilde{c}_4 = 1$. Critical exponents are $\nu = 1.00(15)$, $\alpha = -0.41(6)$, $\beta = 0.42(2)$ and $\gamma = -0.99(7)$. $\Delta C = C - 0.84(6) = -0.67(14) \cdot N^{\alpha/\nu}$ and γ_1 is the exponent of the correction to the scaling behaviour of susceptibility $\Delta\chi = \chi - 1.13(2) \cdot N^{\gamma/\nu} = 7.5(4) \cdot N^{-2.00(6)}$. Different colors represent different matrix sizes up to $N = 50$.

discontinuity or a sharp edge, leading to either 2nd or 3rd order transition. That this transition cannot be 2nd order can be illustrated by analyzing critical exponents. Even if we assume non-diverging $\alpha = 0$ discontinuity in C masked by errors, our exponents (Table C.1) cannot satisfy (C.7), adding up to 0.85(3) instead of 2. However, a 3rd order transition could explain both this discrepancy and the value $\nu = 1$, assuming that transition sees the compactified 3rd dimension of the $\mathfrak{h}^{\mathrm{tr}}$ space:

$$\nu = \frac{m}{d} = \frac{3}{3} = 1. \tag{C.9}$$

In Figure C.2, we see collapsed data for the $\updownarrow \to \uparrow\downarrow$ transition at $\widetilde{c}_4 = 1$. Both C and χ remain finite, and the transition governed by the split in eigenvalue distribution is 3rd order, the same type as in the PP model. The $\uparrow\downarrow \to \uparrow\uparrow$ transition at this $\widetilde{c}_4$ shows nearly identical peak in C as the $\updownarrow \to \uparrow\downarrow$ transition (nicely seen in green data of the top left plot in Figure C.2) and it also appears to be 3rd order.

Near the triple point, at $\widetilde{c}_4 = 0.01$, $\updownarrow + \uparrow\downarrow \to \uparrow\uparrow$ transition is 1st order and both C and χ diverge with

$$\frac{\alpha}{\nu} = 3.07(3), \qquad \frac{\gamma}{\nu} = 3.47(8). \tag{C.10}$$

We have detected both 1st and 2nd order transitions for different matrix sizes in different parts of parameter space. For small $\widetilde{c}_4$ we have well-separated $\updownarrow$ and $\uparrow\uparrow$ phases. For large $\widetilde{c}_4$ all three phases are well separated. For the intermediary values of $\widetilde{c}_4$ we encounter phase coexistence region which grows smaller with increasing matrix size and hopefully collapses

Table C.1: Comparison of critical exponents between our model and the Ising model [51].

model	α	β	γ	ν
↕→↑↑ @ $\tilde{c}_4 = 0.0001$	≤ 0	0.40(2)	0.05(1)	1.00(2)
↕→↑↓ @ $\tilde{c}_4 = 1.0000$	−0.41(6)	0.42(2)	−0.99(7)	1.00(15)
Ising 2D	0 (log)	1/8	7/4	1
Ising 3D	0.110(1)	0.3265(3)	1.2372(5)	0.6301(4)

into a triple point in the infinite limit. In that region smaller $\tilde{c}_4$ show ↕+↑↓ mixture of phases, while larger $\tilde{c}_4$ show ↑↓′+↑↓″ mixture of phases (bottom center plot in Figure 3.1). The former is more symmetric and apparently produces 2nd order transitions, while latter is less symmetric and leads to 1st order transitions.

R-on case

For small values of $\tilde{c}_2$ and $\tilde{c}_4$ in the R-on case, the EOM solution

$$\Phi^2 = \frac{c_2\,\mathbb{1} - c_r|R|}{2c_4} \tag{C.11}$$

is not possible since not all eigenvalues of Φ^2 are positive. In this regime, there is a gradual activation of curvature eigenvalues, as shown in Figure 4.7. This is followed by an appearance of peaks in χ, which begs the question whether this region represents a new kind of ↕↑-phase.

As we see in Figure C.3, the total susceptibility at these peaks does not scale with N, unlike what we would expect from a phase transition. Also, the $N = 50, 60$ data for $(c_k, c_r, \tilde{c}_2) = (1, 0.1, 0.5)$ seem to indicate that the border of this regime for $\tilde{\mathcal{S}}$ recedes towards $\tilde{c}_4 = 0$ and likely disappears in the large N limit. The disappearance would be consistent with apparently identical limit of the peaks' maximums (the right-hand plot in Figure C.3). However, even if

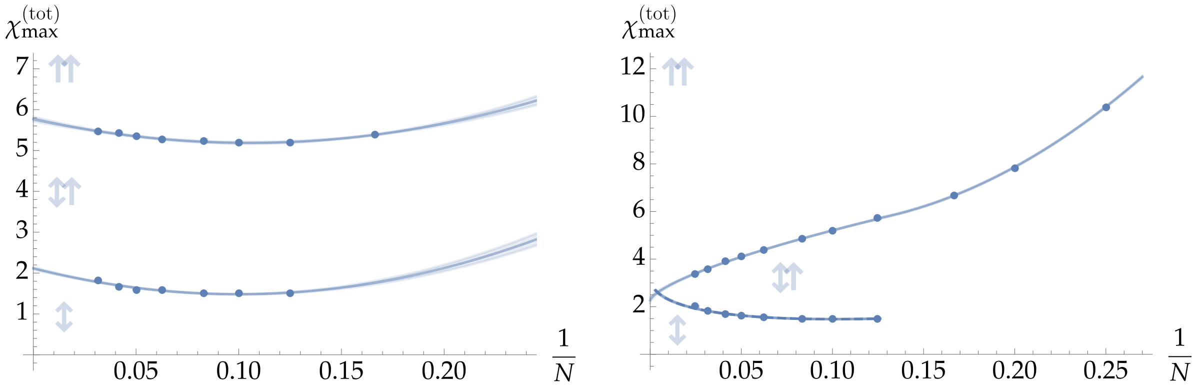

Figure C.3: $\chi^{(\text{tot})}_{\text{max}}$ scaling for ↕→↕↑ and ↕↑→↑↑ transition in the model with a kinetic term. /LEFT/ $(c_r, c_4) = (0.1, 0.01)$. /RIGHT/ $(c_r, \tilde{c}_4) = (0.1, 0.001)$.

this regime vanishes for $\widetilde{\mathcal{S}}$, the same is not necessarily true for $\mathcal{S}$, since the $\widetilde{\mathcal{S}}$-phase diagram occupies the infinity of the $\mathcal{S}$-phase diagram. More work is needed to clarify what happens in this part of the model's parameter space.

Appendix D

False vacua

Let us assume that for some combination of model parameters false vacua of the model are well separated and their distribution functions $\rho_i(\Phi)$ effectively do not overlap. Numerics imply this is a good approximation starting near the edge of and going deeper into the $\uparrow\uparrow$-phase. We can then write

$$\rho \approx \sum_i \alpha_i \rho_i, \qquad \sum_i \alpha_i = 1, \qquad i \geq 0. \tag{D.1}$$

These vacua would correspond to different sign combinations of the field eigenvalues and would have different energies due to logarithmic repulsion in the effective action coming from $\Delta(\Lambda)$.

We can rewrite our quantities in terms of their versions restricted to these false vacua:

$$\langle \mathcal{O} \rangle = \sum_i \alpha_i \int \mathrm{d}\Phi \, \mathcal{O} \, \rho_i = \sum_i \alpha_i \langle \mathcal{O} \rangle_i \tag{D.2}$$

and

$$\begin{aligned}
C &= \langle S^2 \rangle - \langle S \rangle^2 && \text{(D.3)}\\
&= \sum_i \alpha_i \langle S^2 \rangle_i - \left(\sum_i \alpha_i \langle S \rangle_i \right)^2 && \text{(D.4)}\\
&= \sum_i \alpha_i \langle S^2 \rangle_i - \sum_i \alpha_i^2 \langle S \rangle_i^2 - 2 \sum_{i<j} \alpha_i \alpha_j \langle S \rangle_i \langle S \rangle_j && \text{(D.5)}\\
&= \sum_i \alpha_i (\langle S^2 \rangle_i - \langle S \rangle_i^2) + \sum_i \alpha_i (1-\alpha_i) \langle S \rangle_i^2 - 2 \sum_{i<j} \alpha_i \alpha_j \langle S \rangle_i \langle S \rangle_j && \text{(D.6)}\\
&= \sum_i \alpha_i C_i + \sum_i \alpha_i (1-\alpha_i) \langle S \rangle_i^2 - 2 \sum_{i<j} \alpha_i \alpha_j \langle S \rangle_i \langle S \rangle_j && \text{(D.7)}\\
&= \sum_i \alpha_i C_i + \sum_i \alpha_i (1-\alpha_i) E_i^2 - 2 \sum_{i<j} \alpha_i \alpha_j E_i E_j. && \text{(D.8)}
\end{aligned}$$

Assumimg

$$E_0 < E_{i>0}, \qquad \alpha_0 \gg \alpha_{i>0}, \qquad \frac{E_0}{E_{i>0}} = O(1), \tag{D.9}$$

we find up to $O(\alpha_i)$

$$\begin{aligned}
C &\approx \sum_i \alpha_i C_i + \alpha_0(1-\alpha_0)E_0^2 + \sum_{i>0}\alpha_i E_i^2 - 2\sum_{i>0}\alpha_0\alpha_i E_0 E_i &\quad \text{(D.10)}\\
&= \sum_i \alpha_i C_i + \alpha_0(1-\alpha_0)E_0^2 + \sum_{i>0}\alpha_i E_i^2 - 2\alpha_0 E_0 \sum_{i>0}\alpha_i E_i &\quad \text{(D.11)}\\
&= \sum_i \alpha_i C_i + \alpha_0(1-\alpha_0)E_0^2 + \sum_{i>0}\alpha_i E_i^2 - 2\alpha_0 E_0 (E-\alpha_0 E_0) &\quad \text{(D.12)}\\
&= \sum_i \alpha_i C_i + \alpha_0(1+\alpha_0)E_0^2 - 2\alpha_0 E_0 E + \sum_{i>0}\alpha_i E_i^2. &\quad \text{(D.13)}
\end{aligned}$$

As it can be seen in Figure D.1, our simulations satisfies

$$\frac{C_i}{C_j} = O(1), \qquad |E_i - E| \ll |E|, \qquad E_i < 0, \tag{D.14}$$

so $E_i \approx E$ and

$$C \approx \sum_i \alpha_i C_i + (1-\alpha_0)^2 E^2. \tag{D.15}$$

Finally, using

$$\frac{C_i}{C_j} = O(1) \tag{D.16}$$

and assuming that $1-\alpha_0 \ll 1$, we have

$$C \approx C_0. \tag{D.17}$$

This analysis becomes relevant near the ↑↓ → ↑↑ transition. It assures that if we are stuck in the lowest energy local minimum of the potential and unable to probe all the minima, the simulation will still give at least a qualitatively correct result for the peak of C and, therefore, for the transition line position.

We can also use short simulation runs in the large $\tilde{c}_2$ regime to assess E_i and conclude which field configuration has the lowest energy and if the ordered phase is present at the particular point of the phase diagram. We used this method to confirm the phase at a few locations in the phase diagram in Figure 4.13. We aimed to explore all the different eigenvalue-sign combinations since, due to the complicated kinetic term, it is not obvious that eigenvalue permutations would necessarily lead to the same estimates. This approach disproportionately favors the small trace combinations, which is a problem since the number of combinations grows as 2^N, so it quickly becomes impossible to cycle through all of them. Luckily, Figure D.1 implies that a partial vacuum scan is sufficient. On the left-hand side of Figure D.1, we see a system in the ↑↑-phase since the field configuration with the largest magnetization has the lowest energy. On the right-hand side, the system is in the ↑↓-phase, and even when we start with the fully ordered initial state, we end up with a partially ordered state

$$\frac{|\langle \operatorname{tr}\Phi\rangle|}{\sqrt{\langle \operatorname{tr}\Phi^2\rangle}} \approx 0.34, \tag{D.18}$$

which has an unequal number of positive and negative eigenvalues.

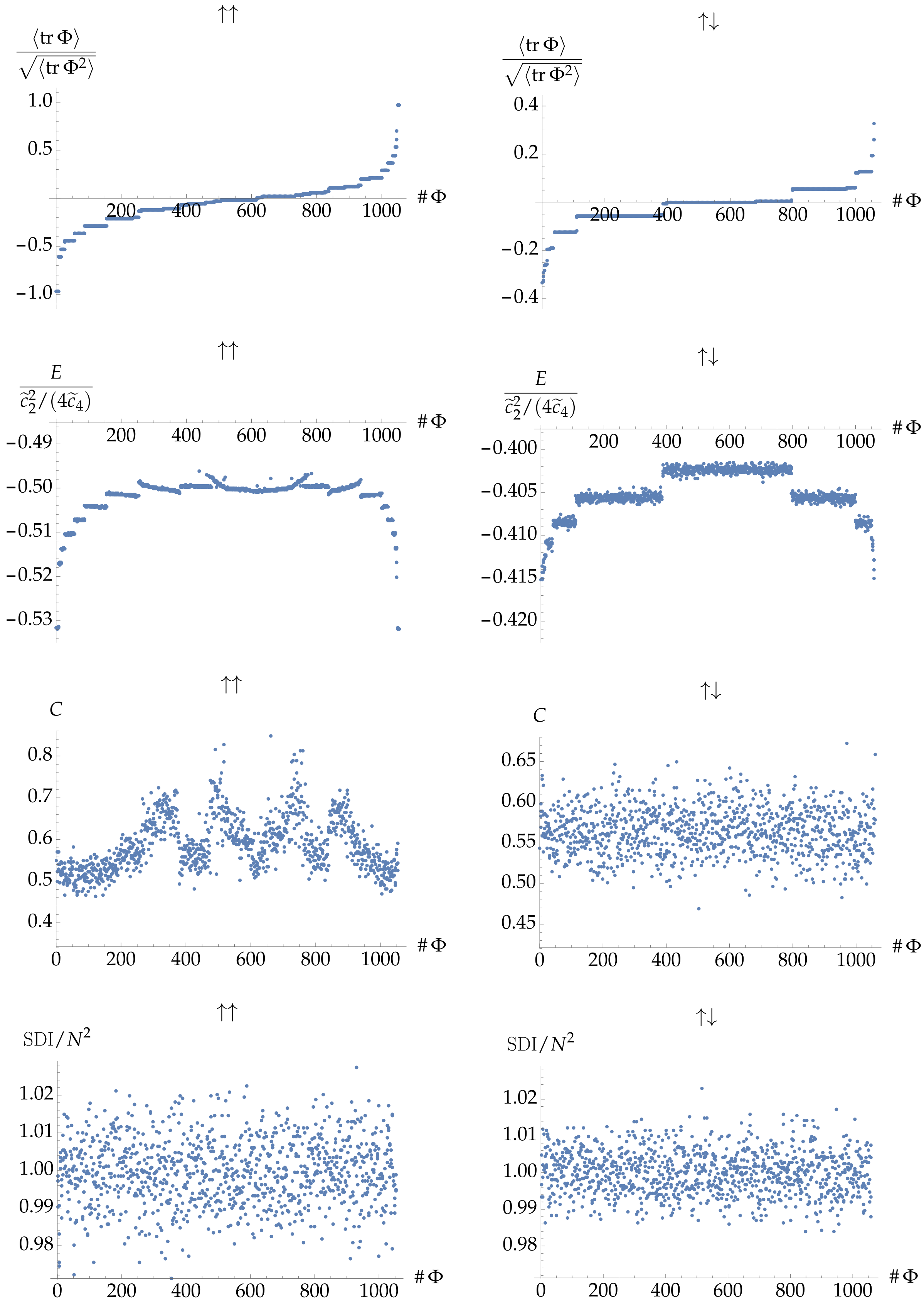

Figure D.1: Thermodynamical observables for $N = 24$ assessed in short runs around the different vacuum choices. The (false) vacuum iterations are ordered (#Φ) by the non-decreasing value of tr Φ. /LEFT/ $(c_k, c_r, \widetilde{c}_2, ,\widetilde{c}_4) = (1, 0.2, 6, 1)$. /RIGHT/ $(c_k, c_r, \widetilde{c}_2, ,\widetilde{c}_4) = (1, 0.2, 6, 2.5)$.

Appendix E

Transition line coefficients

In order to access the large N convergence of the $\updownarrow\rightarrow\uparrow\uparrow$ transition line and subsequently that of $a(N)$ and $b(N)$, we compared the following two approaches.

Table E.1: Comparison of the estimates of a_i and b_i using fits for different $\Delta\nu_k$ and fixed $\widetilde{c}_4$ (method I, using (4.3.29)) to the estimates from $\nu_k = 0$ and variable $\widetilde{c}_4$ and N (method II, using (4.3.30)).

O	$\Delta\nu_k$	$\widetilde{c}_4$	expression	method I	method II
N	-1.0	$1 \cdot 10^{-5}$	b_0	$11.4(9)$	$10.5(5)$
$\sqrt{N}$	-1.0	$1 \cdot 10^{-5}$	b_1	$-36(6)$	$-31(4)$
	-0.5	$5 \cdot 10^{-3}$	b_0	$10.6(6)$	$10.5(5)$
1	-1.0	$1 \cdot 10^{-5}$	$b_2 + a_0/\sqrt{\widetilde{c}_4}$	$55(9)$	$46(9)$
	-0.5	$5 \cdot 10^{-3}$	$b_1 + a_0/\sqrt{\widetilde{c}_4}$	$-32(3)$	$-31(4)$
	0.0	$1 \cdot 10^{-3}$	$b_0 + a_0/\sqrt{\widetilde{c}_4}$	$10.7(5)$	$10.8(5)$
	2.0	$1 \cdot 10^{-2}$	a_0	$-0.00(4)$	$0.1(2)$
$\frac{1}{\sqrt{N}}$	-0.5	$5 \cdot 10^{-3}$	$b_2 + a_1/\sqrt{\widetilde{c}_4}$	$50(3)$	$44(9)$
	0.0	$1 \cdot 10^{-3}$	$b_1 + a_1/\sqrt{\widetilde{c}_4}$	$-24(4)$	$-29(4)$
	0.5	$1 \cdot 10^{-2}$	$b_0 + a_1/\sqrt{\widetilde{c}_4}$	$12(1)$	$11.2(9)$
	2.0		a_1	$-0.0(2)$	$0.07(7)$
$\frac{1}{N}$	-1.0	$1 \cdot 10^{-5}$	$a_2 + b_4\sqrt{\widetilde{c}_4}$	$1.99(7)$	$2.0(2)$
	0.0	$1 \cdot 10^{-3}$	$b_2 + a_2/\sqrt{\widetilde{c}_4}$	$86(6)$	$109(9)$
	0.5	$1 \cdot 10^{-2}$	$b_1 + a_2/\sqrt{\widetilde{c}_4}$	$-17(8)$	$-11(4)$
	1.0		$a_2 + b_0\sqrt{\widetilde{c}_4}$	$3.3(3)$	$3.1(1)$
	2.0		a_2	$2.3(3)$	$2.06(9)$

Method I

For fixed $\widetilde{c}_4$ and various fixed ν_k, we varied N and for each detected $\widetilde{c}_2(N)$ at which the transition occurs. We then fitted the $1/\sqrt{N}$-expansion of (4.3.29) (Figure E.1) to get the combinations of a_i, b_i and $\widetilde{c}_4$ (Table E.1).

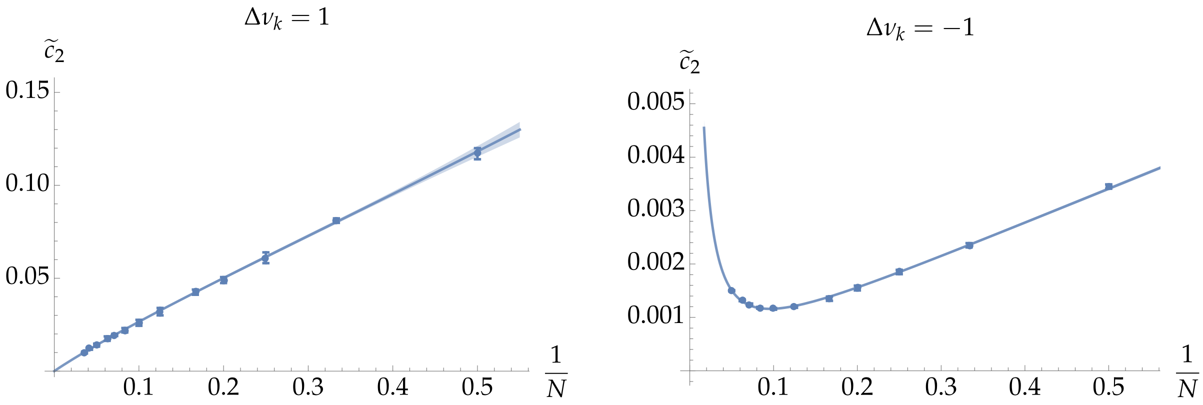

Figure E.1: Examples of $1/\sqrt{N}$-series fits for different scalings of the kinetic term. Pale-colored stripes represent the 68% confidence intervals of the fits. /LEFT/ Scaling $\widetilde{\nu}_k = 1$ at $\widetilde{c}_4 = 10^{-2}$ for $N \leq 28$. /RIGHT/ Scaling $\widetilde{\nu}_k = -1$ at $\widetilde{c}_4 = 10^{-5}$ for $N \leq 20$.

In Figure E.1 we see examples of undesirable scalings of the kinetic term

$$\nu_k = +1: \qquad \widetilde{c}_2 = \frac{0.33(3)}{N} - \frac{0.24(10)}{N^{3/2}} + \frac{0.16(11)}{N^2}, \tag{E.1a}$$

$$\nu_k = -1: \qquad \widetilde{c}_2 = 6.3(2)N + 0.55(9) - \frac{0.36(6)}{\sqrt{N}} + \frac{0.114(9)}{N}. \tag{E.1b}$$

For both of them there is no non-trivial large N limit of the transition line, the first one being zero, and the second one infinite. Plots for desirable scaling are presented in Section 4.3.

Method II

For fixed N and $\nu_k = 0$, we constructed the transition line for a range of $\widetilde{c}_4$ and then extracted $a(N)$ and $b(N)$ using (4.3.22). We then varied N and fitted series (4.3.30) to get a_i and b_i (Figure 4.5).

Applying the method II to the χ-data from Figure 4.5, we got the expansions (4.3.30) restated here:

$$a(N) = \sum_{k=0}^{\infty} \frac{a_i}{\sqrt{N}^k} = 0.01(1) + \frac{0.07(7)}{\sqrt{N}} + \frac{2.06(9)}{N}, \tag{E.2a}$$

$$b(N) = \sum_{k=0}^{\infty} \frac{b_i}{\sqrt{N}^k} = 10.5(5) - \frac{31(4)}{\sqrt{N}} + \frac{43(9)}{N} - \frac{24(8)}{N\sqrt{N}}, \tag{E.2b}$$

To obtain them, we used the lowest order polynomial in $1/\sqrt{N}$ that fits well with the data. The higher terms turn out to be indiscernible from zero within their large uncertainties. The C-data have much less predictive power since the peaks of C are wide, skewed, nearly flat and do not scale with N, unlike the peaks in χ which are well resolved.

The comparison of these two approaches is given in Table E.1. We see that the choice of $\nu_k = 0$ scaling of the kinetic term leads to consistent values for coefficients of the transition line. Also, with increasing matrix size, $\Delta\nu_k > 0$ transition points collapse to zero in the predicted manner, which is for $\Delta\nu_k \geq 1$ practically linear.

Appendix F

Triple point extrapolations

Different extrapolations of the R-off triple point position in the infinite matrix limit are collected in Table F.1. As it can be seen, all the intercepts are consistent with the triple point located at the origin of the parameter space.

Table F.1: Different models of R-off triple point position fitting. A linear fit is performed for data subsets with higher N, where nonlinearities are imperceptible.

c_i	data	model	fit
$\widetilde{c}_4$	$\mathcal{X}$	linear	$\widetilde{c}_4 = -0.014(18) + 5.9(7)/N$
		quadratic	$\widetilde{c}_4 = -0.003(17) + 5.0(9)/N + 19(12)/N^2$
		power law	$\widetilde{c}_4 = +0.016(21) + 12(5)/N^{1.25(14)}$
	C	linear	$\widetilde{c}_4 = -0.12(10) + 16(3)/N$
$\widetilde{c}_2$	$\mathcal{X}$	linear	$\widetilde{c}_2 = +0.05(8) + 38(3)/N$
		quadratic	$\widetilde{c}_2 = -0.02(14) + 43(7)/N - 76(81)/N^2$
		power law	$\widetilde{c}_2 = -0.2(4) + 25(11)/N^{0.83(21)}$
	C	linear	$\widetilde{c}_2 = +0.9(9) + 93(21)/N$

Appendix G

Curvature terms in the effective action

This section contains a part of our results [79] concerning the $S_{\mathrm{R+PP}}$ submodel.

It can be proven that HCIZ integral (4.6.55) can be written as a power series in t

$$\mathrm{HCIZ} = \frac{c_N}{t^{N(N-1)/2}} \frac{\det \mathring{e}^{\,t|a\rangle\langle b|}}{\Delta(A)\Delta(B)} = \sum_{i=0}^{\infty} t^i \cdot \mathrm{HCIZ}_i \tag{G.1}$$

where the first 4 terms are[*]

$$\mathrm{HCIZ}_0 = 1, \tag{G.2a}$$

$$\mathrm{HCIZ}_1 = \frac{\operatorname{tr} A \operatorname{tr} B}{N}, \tag{G.2b}$$

$$\mathrm{HCIZ}_2 = \sum_{\pm} \frac{(\operatorname{tr}^2 A \pm \operatorname{tr} A^2)(\operatorname{tr}^2 B \pm \operatorname{tr} B^2)}{4N(N \pm 1)}, \tag{G.2c}$$

$$\begin{aligned} \mathrm{HCIZ}_3 = {} & \sum_{\pm} \frac{(\operatorname{tr}^3 A \pm 3 \operatorname{tr} A \operatorname{tr} A^2 + 2 \operatorname{tr} A^3)(\operatorname{tr}^3 B \pm 3 \operatorname{tr} B \operatorname{tr} B^2 + 2 \operatorname{tr} B^3)}{36N(N \pm 1)(N \pm 2)} \\ & + \frac{(\operatorname{tr}^3 A - \operatorname{tr} A^3)(\operatorname{tr}^3 B - \operatorname{tr} B^3)}{9N(N-1)(N+1)}. \end{aligned} \tag{G.2d}$$

If we substitute[†] $A = \operatorname{diag}(1, \dots, N)$ and $B = \Lambda^2$, and write

$$\mathrm{HCIZ} = \exp\left(- \sum_{i=1}^{\infty} t^i S_i \right) \tag{G.3}$$

$$= 1 - tS_1 + t^2 \left(\frac{S_1^2}{2} - S_2 \right) - t^3 \left(\frac{S_1^3}{6} - S_1 S_2 + S_3 \right) + O(t^4), \tag{G.4}$$

then equating terms in (G.1) and (G.4) gives

$$S_1 = -\frac{N+1}{2} \operatorname{tr} \Lambda^2, \qquad S_2 = -\frac{N}{24} \operatorname{tr} \Lambda^4 + \frac{1}{24} \operatorname{tr}^2 \Lambda^2, \qquad S_3 = 0. \tag{G.5}$$

---

[*] Summation $\sum_{\pm}$ contains only two terms corresponding to either all + or all − signs.

[†] The switch $R \to -16A$ leads to a sub-leading difference in $S_N(\Lambda)$, which disappears in the large N limit.

Finally, by substituting $t \to -16c_r$, we obtain the large N effective action up to the $O(c_r^3)$

$$S_N(\Lambda) = N\,\mathrm{tr}\left(-\left(\widetilde{c}_2 - 8c_r\right)\Lambda^2 + \left(\widetilde{c}_4 - \frac{32}{3}c_r^2\right)\Lambda^4\right) + \frac{32}{3}c_r^2\,\mathrm{tr}^2\,\Lambda^2 - \log\Delta^2(\Lambda). \tag{G.6}$$

Let us, as an example, prove (G.2b). Each column col_i of the matrix

$$\mathring{e}^{\,t|a\rangle\langle b|} = \begin{pmatrix} e^{ta_1b_1} & e^{ta_1b_2} & \dots & e^{ta_1b_N} \\ e^{ta_2b_1} & e^{ta_2b_2} & \dots & e^{ta_2b_N} \\ \vdots & \vdots & & \vdots \\ e^{ta_Nb_1} & e^{ta_Nb_2} & \dots & e^{ta_Nb_N} \end{pmatrix} \tag{G.7}$$

can be expanded in t as

$$\mathrm{col}_i = \begin{pmatrix} 1 \\ 1 \\ \vdots \\ 1 \end{pmatrix} + t \begin{pmatrix} a_1b_i \\ a_2b_i \\ \vdots \\ a_Nb_i \end{pmatrix} + \frac{t^2}{2!} \begin{pmatrix} a_1^2b_i^2 \\ a_2^2b_i^2 \\ \vdots \\ a_N^2b_i^2 \end{pmatrix} + \cdots$$

$$= \begin{pmatrix} 1 \\ 1 \\ \vdots \\ 1 \end{pmatrix} + tb_i \begin{pmatrix} a_1 \\ a_2 \\ \vdots \\ a_N \end{pmatrix} + \frac{t^2b_i^2}{2!} \begin{pmatrix} a_1^2 \\ a_2^2 \\ \vdots \\ a_N^2 \end{pmatrix} + \cdots. \tag{G.8}$$

Having in mind that we can split determinant along a column

$$\det(\dots, \alpha\,\mathrm{col}' + \beta\,\mathrm{col}'', \dots) = \alpha\det(\dots, \mathrm{col}', \dots) + \beta\det(\dots, \mathrm{col}'', \dots), \tag{G.9}$$

we can write $\det\mathring{e}^{\,t|a\rangle\langle b|}$ as

$$\det\mathring{e}^{\,t|a\rangle\langle b|} = \sum_{i\geq 0} t^iD_i = \sum_{k_i\geq 0} \frac{t^{k_1+k_2+\cdots+k_N}}{k_1!k_2!\dots k_N!} b_1^{k_1}b_2^{k_2}\dots b_N^{k_N} \begin{vmatrix} a_1^{k_1} & a_1^{k_2} & \cdots & a_1^{k_N} \\ a_2^{k_1} & a_2^{k_2} & \cdots & a_2^{k_N} \\ \vdots & \vdots & & \vdots \\ a_N^{k_1} & a_N^{k_2} & \cdots & a_N^{k_N} \end{vmatrix}, \tag{G.10}$$

where the matrix in the sum contains different choices of columns from the expansion (G.8).

Notice that $k_i \neq k_j$, otherwise columns col_i and col_j are proportional and the corresponding determinant vanishes. Due to this, $\det \mathring{e}^{\,t|a\rangle\langle b|}$ expansion starts with k_i that are permutations of $(0, 1, \ldots, N-1)$

$$k_i = \pi(i) - 1, \tag{G.11}$$

that is with

$$O\left(t^{0+1+\ldots+(N-1)}\right) = O\left(t^{N(N-1)/2}\right). \tag{G.12}$$

We get the second non-zero term by increasing one of the k_i by 1, but still demanding that all k_i be different. This is satisfied only by the replacement

$$N - 1 \to N, \tag{G.13}$$

meaning that k_i are permutations of $(0, 1, 2, \ldots, N-2, N)$. This choice yields

$$D_{N(N-1)/2+1} = \sum_{\pi} \frac{\prod_{i=1}^{N} b_i^{\pi(i)-1+\delta_{\pi(i),N}}}{0!1!\ldots(N-2)!N!} \begin{vmatrix} a_1^{\pi(1)-1+\delta_{\pi(i),N}} & \cdots & a_1^{\pi(N)-1+\delta_{\pi(i),N}} \\ a_2^{\pi(1)-1+\delta_{\pi(i),N}} & \cdots & a_2^{\pi(N)-1+\delta_{\pi(i),N}} \\ \vdots & & \vdots \\ a_N^{\pi(1)-1+\delta_{\pi(i),N}} & \cdots & a_N^{\pi(N)-1+\delta_{\pi(i),N}} \end{vmatrix}. \tag{G.14}$$

If we order the columns by ascending powers of a_i, we get a factor $\operatorname{sgn}\pi$ from column permutations

$$D_{N(N-1)/2+1} = \frac{1}{Nc_N} \sum_{\pi} \operatorname{sgn}\pi \prod_{i=1}^{N} b_i^{\pi(i)-1+\delta_{\pi(i),N}} \begin{vmatrix} a_1^0 & a_1^1 & \cdots & a_1^{N-2} & a_1^N \\ a_2^0 & a_2^1 & \cdots & a_2^{N-2} & a_2^N \\ \vdots & \vdots & & \vdots & \vdots \\ a_N^0 & a_N^1 & \cdots & a_N^{N-2} & a_N^N \end{vmatrix}. \tag{G.15}$$

Finally, by writing

$$\mathcal{B}_{ij} = b_i^{j-1+\delta_{j,N}}, \tag{G.16}$$

we recognize

$$\sum_{\pi} \operatorname{sgn}\pi \prod_{i=1}^{N} b_i^{\pi(i)-1+\delta_{\pi(i),N}} = \sum_{\pi} \operatorname{sgn}\pi \prod_{i=1}^{N} \mathcal{B}_{i,\pi(i)} = \det \mathcal{B}, \tag{G.17}$$

that is

$$D_{N(N-1)/2+1} = \frac{1}{Nc_N} \begin{vmatrix} a_1^0 & a_1^1 & \cdots & a_1^{N-2} & a_1^N \\ a_2^0 & a_2^1 & \cdots & a_2^{N-2} & a_2^N \\ \vdots & \vdots & & \vdots & \vdots \\ a_N^0 & a_N^1 & \cdots & a_N^{N-2} & a_N^N \end{vmatrix} \cdot \begin{vmatrix} b_1^0 & b_1^1 & \cdots & b_1^{N-2} & b_1^N \\ b_2^0 & b_2^1 & \cdots & b_2^{N-2} & b_2^N \\ \vdots & \vdots & & \vdots & \vdots \\ b_N^0 & b_N^1 & \cdots & b_N^{N-2} & b_N^N \end{vmatrix}. \tag{G.18}$$

Determinants in the previous formula are modified Vandermonde determinants, which we denote

$$\Delta(A_N|N-1\to N) \quad \text{and} \quad \Delta(B_N|N-1\to N), \tag{G.19}$$

where optional subscript N indicates the size of the matrix, and conditions stated after the vertical line represent the increased powers of matrix elements compared to $(0,1,\dots,N-1)$.

Looking at the expressions for small N, and having in mind that $\Delta(A)|D_i$, we hypothesize that

$$\Delta(A_N|N-1\to N) = \begin{vmatrix} 1 & a_1 & a_1^2 & \cdots & a_1^{N-2} & a_1^N \\ 1 & a_2 & a_2^2 & \cdots & a_2^{N-2} & a_2^N \\ \vdots & \vdots & \vdots & & \vdots & \vdots \\ 1 & a_N & a_N^2 & \cdots & a_N^{N-2} & a_N^N \end{vmatrix} = \Delta(A_N)\,\mathrm{tr}\,A_N, \tag{G.20}$$

and then proceed to prove (G.20) by induction. It is easy to check that (G.20) holds for $N=2$. Let us further assume that it is true for N and look what happens with the $(N+1)\times(N+1)$ matrix. We can first use the last row to eliminate 1s from the first column

$$\Delta(A_{N+1}|N\to N+1) = \begin{vmatrix} 1 & a_1 & a_1^2 & \cdots & a_1^{N-1} & a_1^{N+1} \\ 1 & a_2 & a_2^2 & \cdots & a_2^{N-1} & a_2^{N+1} \\ \vdots & \vdots & \vdots & & \vdots & \vdots \\ 1 & a_N & a_N^2 & \cdots & a_N^{N-1} & a_N^{N+1} \\ 1 & a_{N+1} & a_{N+1}^2 & \cdots & a_{N+1}^{N-1} & a_{N+1}^{N+1} \end{vmatrix} \begin{array}{l} \longleftarrow + \\ \longleftarrow + \\ \\ \longleftarrow + \\ \cdot(-1)\ \ \cdot(-1)\ \ \cdot(-1) \end{array} \tag{G.21}$$

$$= \begin{vmatrix} 0 & a_1-a_{N+1} & a_1^2-a_{N+1}^2 & \cdots & a_1^{N-1}-a_{N+1}^{N-1} & a_1^{N+1}-a_{N+1}^{N+1} \\ 0 & a_2-a_{N+1} & a_2^2-a_{N+1}^2 & \cdots & a_2^{N-1}-a_{N+1}^{N-1} & a_2^{N+1}-a_{N+1}^{N+1} \\ \vdots & \vdots & \vdots & & \vdots & \vdots \\ 0 & a_N-a_{N+1} & a_N^2-a_{N+1}^2 & \cdots & a_N^{N-1}-a_{N+1}^{N-1} & a_N^{N+1}-a_{N+1}^{N+1} \\ 1 & a_{N+1} & a_{N+1}^2 & \cdots & a_{N+1}^{N-1} & a_{N+1}^{N+1} \end{vmatrix}.$$

The next step is to use Laplace expansion along the first column, followed by the subtraction of $a_{N+1}\,\mathrm{col}_i$ from col_{i+1}, except for the last column col_{N+1} from which we subtract $a^2_{N+1}\,\mathrm{col}_N$:

$$\Delta(A_{N+1}|N\to N+1) = (-1)^{N+2}\times$$

$$\begin{array}{cccccc}
\cdot(-a_{N+1})\ \ulcorner\!\!\longrightarrow & \overset{+}{\downarrow} & & \cdot(-a_{N+1})\ \ulcorner\!\!\longrightarrow & \overset{+}{\downarrow}\ \ \overset{\cdot(-a^2_{N+1})}{\ulcorner}\!\!\longrightarrow & \overset{+}{\downarrow}
\end{array}$$

$$\times\begin{vmatrix}
a_1-a_{N+1} & a_1^2-a_{N+1}^2 & \cdots & a_1^{N-2}-a_{N+1}^{N-2} & a_1^{N-1}-a_{N+1}^{N-1} & a_1^{N+1}-a_{N+1}^{N+1}\\
a_2-a_{N+1} & a_2^2-a_{N+1}^2 & \cdots & a_2^{N-2}-a_{N+1}^{N-2} & a_2^{N-1}-a_{N+1}^{N-1} & a_2^{N+1}-a_{N+1}^{N+1}\\
\vdots & \vdots & & \vdots & \vdots & \vdots\\
a_N-a_{N+1} & a_N^2-a_{N+1}^2 & \cdots & a_N^{N-2}-a_{N+1}^{N-2} & a_N^{N-1}-a_{N+1}^{N-1} & a_N^{N+1}-a_{N+1}^{N+1}
\end{vmatrix}. \tag{G.22}$$

We can simplify the $(i,j+1)$ element of the determinant into

$$\left(a_i^{j+1}-a_{N+1}^{j+1}\right)-a_{N+1}\left(a_i^j-a_{N+1}^j\right)=a_i^j\left(a_i-a_{N+1}\right), \tag{G.23}$$

and $(i,N+1)$ element into

$$\left(a_i^{N+1}-a_{N+1}^{N+1}\right)-a_{N+1}^2\left(a_i^{N-1}-a_{N+1}^{N-1}\right)=a_i^{N-1}\left(a_i^2-a_{N+1}^2\right), \tag{G.24}$$

which gives

$$\Delta(A_{N+1}|N\to N+1) = (-1)^{N+2}\times$$

$$\times\begin{vmatrix}
a_1-a_{N+1} & a_1\left(a_1-a_{N+1}\right) & \cdots & a_1^{N-2}\left(a_1-a_{N+1}\right) & a_1^{N-1}\left(a_1^2-a_{N+1}^2\right)\\
a_2-a_{N+1} & a_2\left(a_2-a_{N+1}\right) & \cdots & a_2^{N-2}\left(a_2-a_{N+1}\right) & a_2^{N-1}\left(a_2^2-a_{N+1}^2\right)\\
\vdots & \vdots & & \vdots & \vdots\\
a_N-a_{N+1} & a_N\left(a_N-a_{N+1}\right) & \cdots & a_N^{N-2}\left(a_N-a_{N+1}\right) & a_N^{N-1}\left(a_N^2-a_{N+1}^2\right)
\end{vmatrix}. \tag{G.25}$$

The each element in the i^{th} row has a common multiplier $a_i - a_{N+1}$, which we can extract from the determinant to get

$$\Delta(A_{N+1}|N \to N+1) = (-1)^{N+2} \prod_{j=1}^{N} \left(a_i - a_{N+1}\right) \times \\ \times \begin{vmatrix} 1 & a_1 & \cdots & a_1^{N-2} & a_1^{N-1}\left(a_1 + a_{N+1}\right) \\ 1 & a_2 & \cdots & a_2^{N-2} & a_2^{N-1}\left(a_2 + a_{N+1}\right) \\ \vdots & \vdots & & \vdots & \vdots \\ 1 & a_N & \cdots & a_N^{N-2} & a_N^{N-1}\left(a_N + a_{N+1}\right) \end{vmatrix}. \tag{G.26}$$

We can now split the determinant along the last column

$$\begin{vmatrix} 1 & a_1 & \cdots & a_1^{N-2} & a_1^{N} \\ 1 & a_2 & \cdots & a_2^{N-2} & a_2^{N} \\ \vdots & \vdots & & \vdots & \vdots \\ 1 & a_N & \cdots & a_N^{N-2} & a_N^{N} \end{vmatrix} + a_{N+1} \begin{vmatrix} 1 & a_1 & \cdots & a_1^{N-2} & a_1^{N-1} \\ 1 & a_2 & \cdots & a_2^{N-2} & a_2^{N-1} \\ \vdots & \vdots & & \vdots & \vdots \\ 1 & a_N & \cdots & a_N^{N-2} & a_N^{N-1} \end{vmatrix}, \tag{G.27}$$

and end the proof by writing

$$\Delta(A_{N+1}|N \to N+1) = \prod_{j=1}^{N} (a_{N+1} - a_i) \left(\Delta(A_N|N-1 \to N) + a_{N+1}\Delta(A_N)\right) \tag{G.28}$$

$$= \prod_{j=1}^{N} (a_{N+1} - a_i) \left(\Delta(A_N) \operatorname{tr} A_N + a_{N+1}\Delta(A_N)\right) \tag{G.29}$$

$$= \prod_{j=1}^{N} (a_{N+1} - a_i) \Delta(A_N) \left(\operatorname{tr} A_N + a_{N+1}\right) \tag{G.30}$$

$$= \Delta(A_{N+1}) \operatorname{tr} A_{N+1}, \tag{G.31}$$

where in the second line we used our induction hypothesis (G.20).

This proof can be straightforwardly modified for other terms in the expansion of HCIZ. The key step is to identify the non-vanishing combinations of k_i in (G.10) once we increase the power of t by Δp. For the first few terms, it is easy to identify a small number of the possible partitions of Δp into a sum of positive numbers p_i, and then try to increase the highest values in $(0, 1, \ldots, N-1)$ by p_i in such a way to keep all k_i different. For S_2 we need permutations of

$$(0, 1, \ldots, N-2, N+1) \tag{G.32a}$$

and

$$(0, 1, \ldots, N-3, N-1, N), \tag{G.32b}$$

and for S_3 the permutations of

$$(0, 1, \ldots, N-2, N+2), \tag{G.33a}$$

$$(0, 1, \ldots, N-3, N-1, N+1), \tag{G.33b}$$

and

$$(0, 1, \ldots, N-4, N-2, N-1, N). \tag{G.33c}$$

The application of the HCIZ formula and *Mathematica* expansions was proposed by Juraj Tekel. The HCIZ exponential series expansion was proposed by Dragan Prekrat, who also hypothesized and partially proved the form of the expansion terms. Finally, the proof by induction was derived by Dragana Ranković.

List of Symbols and Abbreviations

NC	noncommutative, noncommutativity
GW	the Grosse-Wulkenhaar model
ACF	autocorrelation function
PP	pure potential term: combined mass and quartic terms
EOM	equation of motion
SDI	Schwinger-Dyson Identity
HCIZ	Harish-Chandra-Itzykson-Zuber integral

$\mathfrak{h}$	Heisenberg algebra
$\mathfrak{h}^{\mathrm{tr}}$	truncated Heisenberg algebra
$\mathfrak{h}^{\mathrm{tr}}_{\epsilon}$	modified truncated Heisenberg algebra
$\mathbb{R}^2_\theta$	Moyal plane
S^2_N	Fuzzy sphere
c_k	kinetic term normalization parameter
c_r	curvature coupling
c_2	mass parameter
c_4	quartic coupling
$\widetilde{c}_i$	rescaled parameter $i \in \{k, r, 2, 4\}$
ν_i	scaling of the parameter c_i, $i \in \{k, r, 2, 4\}$
$\updownarrow$	disordered phase
$\uparrow\downarrow$	striped phase
$\uparrow\uparrow$	ordered phase
ρ, ρ_Φ	eigenvalue distribution
ρ_{tr}	trace distribution

Bibliography

[1] L. Carroll, Alice's Adventures in Wonderland (The Project Gutenberg EBook, 2008)

[2] M. Bayley, The mathematical meaning of Alice in Wonderland, New Scientist **204**, 38 (2009)

[3] R. Jackiw, Physical instances of noncommuting coordinates, Nucl. Phys. B Proc. Suppl. **108**, 30 (2002), arXiv:hep-th/0110057

[4] H. S. Snyder, Quantized Space-Time, Phys. Rev. **71**, 38 (1947)

[5] J. Bellissard, A. van Elst, and H. Schulz-Baldes, The noncommutative geometry of the quantum Hall effect, Journal of Mathematical Physics **35**, 5373 (1994), https://doi.org/10.1063/1.530758

[6] K. Fujii, From quantum optics to non-commutative geometry: A Non-commutative version of the Hopf bundle, Veronese mapping and spin representation (2005), arXiv:quant-ph/0502174

[7] N. Seiberg and E. Witten, String theory and noncommutative geometry, JHEP **09**, 032 (1999), arXiv:hep-th/9908142

[8] S. Minwalla, M. Van Raamsdonk, and N. Seiberg, Noncommutative perturbative dynamics, JHEP **02**, 020 (2000), arXiv:hep-th/9912072

[9] C.-S. Chu, J. Madore, and H. Steinacker, Scaling limits of the fuzzy sphere at one loop, JHEP **08**, 038 (2001), arXiv:hep-th/0106205

[10] B. P. Dolan, D. O'Connor, and P. Presnajder, Matrix ϕ^4 models on the fuzzy sphere and their continuum limits, JHEP **03**, 013 (2002), arXiv:hep-th/0109084

[11] C. P. Martin, J. Trampetić, and J. You, UV/IR mixing in noncommutative $SU(N)$ Yang–Mills theory, Eur. Phys. J. C **81**, 878 (2021), arXiv:2012.09119 [hep-th]

[12] E. Langmann and R. J. Szabo, Duality in scalar field theory on noncommutative phase spaces, Physics Letters B **533**, 168âĂŞ177 (2002)

[13] H. Grosse and R. Wulkenhaar, Renormalization of ϕ^4 theory on noncommutative $\mathbb{R}^2$ in the matrix base, JHEP **12**, 019 (2003), arXiv:hep-th/0307017

[14] M. Disertori, R. Gurau, J. Magnen, and V. Rivasseau, Vanishing of Beta Function of Non Commutative $\phi^4(4)$ Theory to all orders, Phys. Lett. B **649**, 95 (2007), arXiv:hep-th/0612251

[15] Z. Wang, Constructive Renormalization of the 2-dimensional Grosse-Wulkenhaar Model, Annales Henri Poincare **19**, 2435 (2018), arXiv:1805.06365 [math-ph]

[16] M. Burić and M. Wohlgenannt, Geometry of the Grosse-Wulkenhaar Model, JHEP **03**, 053 (2010), arXiv:0902.3408 [hep-th]

[17] S. A. Franchino-Viñas and S. Mignemi, Asymptotic freedom for $\lambda\phi^4_\star$ QFT in Snyder–de Sitter space, Eur. Phys. J. C **80**, 382 (2020), arXiv:1911.08921 [hep-th]

[18] M. Burić, D. Latas, and L. Nenadović, Fuzzy de Sitter Space, Eur. Phys. J. C **78**, 953 (2018), arXiv:1709.05158 [hep-th]

[19] M. Burić and D. Latas, Discrete fuzzy de Sitter cosmology, Phys. Rev. D **100**, 024053 (2019), arXiv:1903.08378 [hep-th]

[20] D. N. Blaschke, Gauge Fields on Non-Commutative Spaces and Renormalization, Fortsch. Phys. **62**, 820 (2014), arXiv:1402.5980 [hep-th]

[21] M. Burić, H. Grosse, and J. Madore, Gauge fields on noncommutative geometries with curvature, JHEP **07**, 010 (2010), arXiv:1003.2284 [hep-th]

[22] M. Burić, M. Dimitrijević, V. Radovanović, and M. Wohlgenannt, Quantization of a gauge theory on a curved noncommutative space, Phys. Rev. D **86**, 105024 (2012), arXiv:1203.3016 [hep-th]

[23] M. Burić, L. Nenadović, and D. Prekrat, One-loop structure of the $U(1)$ gauge model on the truncated Heisenberg space, Eur. Phys. J. C **76**, 672 (2016), arXiv:1610.01429 [hep-th]

[24] S. S. Gubser and S. L. Sondhi, Phase structure of noncommutative scalar field theories, Nucl. Phys. B **605**, 395 (2001), arXiv:hep-th/0006119

[25] P. Castorina and D. Zappala, Spontaneous breaking of translational invariance in non-commutative lambda ϕ^4 theory in two dimensions, Phys. Rev. D **77**, 027703 (2008), arXiv:0711.2659 [hep-th]

[26] H. Mejía-Díaz, W. Bietenholz, and M. Panero, The continuum phase diagram of the 2d non-commutative $\lambda\phi^4$ model, JHEP **10**, 056 (2014), arXiv:1403.3318 [hep-lat]

[27] D. J. Gross and E. Witten, Possible Third Order Phase Transition in the Large N Lattice Gauge Theory, Phys. Rev. D **21**, 446 (1980)

[28] X. Martin, A Matrix phase for the ϕ^4 scalar field on the fuzzy sphere, JHEP **04**, 077 (2004), arXiv:hep-th/0402230

[29] M. Panero, Numerical simulations of a non-commutative theory: The Scalar model on the fuzzy sphere, JHEP **05**, 082 (2007), arXiv:hep-th/0608202

[30] D. O'Connor and C. Saemann, Fuzzy Scalar Field Theory as a Multitrace Matrix Model, JHEP **08**, 066 (2007), arXiv:0706.2493 [hep-th]

[31] F. Garcia Flores, X. Martin, and D. O'Connor, Simulation of a scalar field on a fuzzy sphere, Int. J. Mod. Phys. A **24**, 3917 (2009), arXiv:0903.1986 [hep-lat]

[32] F. Lizzi and B. Spisso, Noncommutative Field Theory: Numerical Analysis with the Fuzzy Disc, Int. J. Mod. Phys. A **27**, 1250137 (2012), arXiv:1207.4998 [hep-th]

[33] A. P. Polychronakos, Effective action and phase transitions of scalar field on the fuzzy sphere, Phys. Rev. D **88**, 065010 (2013), arXiv:1306.6645 [hep-th]

[34] M. P. Vachovski, Numerical studies of the critical behaviour of non-commutative field theories, Ph.D. thesis, National University of Ireland Maynooth (2013), http://mural.maynoothuniversity.ie/5439/

[35] J. Tekel, Uniform order phase and phase diagram of scalar field theory on fuzzy $\mathbb{C}P^n$, JHEP **10**, 144 (2014), arXiv:1407.4061 [hep-th]

[36] B. Ydri, New algorithm and phase diagram of noncommutative ϕ^4 on the fuzzy sphere, JHEP **03**, 065 (2014), arXiv:1401.1529 [hep-th]

[37] S. Rea and C. Sämann, The Phase Diagram of Scalar Field Theory on the Fuzzy Disc, JHEP **11**, 115 (2015), arXiv:1507.05978 [hep-th]

[38] J. Tekel, Phase structure of fuzzy field theories and multitrace matrix models, Acta Phys. Slov. **65**, 369 (2015), arXiv:1512.00689 [hep-th]

[39] J. Tekel, Matrix model approximations of fuzzy scalar field theories and their phase diagrams, JHEP **12**, 176 (2015), arXiv:1510.07496 [hep-th]

[40] B. Ydri, K. Ramda, and A. Rouag, Phase diagrams of the multitrace quartic matrix models of noncommutative Φ^4 theory, Phys. Rev. D **93**, 065056 (2016), arXiv:1509.03726 [hep-th]

[41] B. Ydri, Lectures on Matrix Field Theory, Vol. 929 (Springer, 2017) arXiv:1603.00924 [hep-th]

[42] P. Sabella-Garnier, Time dependence of entanglement entropy on the fuzzy sphere, JHEP **08**, 121 (2017), arXiv:1705.01969 [hep-th]

[43] J. Tekel, Asymmetric hermitian matrix models and fuzzy field theory, Phys. Rev. D **97**, 125018 (2018), arXiv:1711.02008 [hep-th]

[44] K. Hatakeyama, A. Tsuchiya, and K. Yamashiro, Renormalization on the fuzzy sphere, PTEP **2018**, 063B05 (2018), arXiv:1805.03975 [hep-th]

[45] S. Kováčik and D. O'Connor, Triple Point of a Scalar Field Theory on a Fuzzy Sphere, JHEP **10**, 010 (2018), arXiv:1805.08111 [hep-th]

[46] D. Prekrat, K. N. Todorović-Vasović, and D. Ranković, Detecting scaling in phase transitions on the truncated Heisenberg algebra, JHEP **03**, 197 (2021), arXiv:2002.05704 [hep-th]

[47] M. Šubjaková and J. Tekel, Fuzzy field theories and related matrix models, PoS **CORFU2019**, 189 (2020), arXiv:2006.12605 [hep-th]

[48] M. Šubjaková and J. Tekel, Second moment fuzzy-field-theory-like matrix models, JHEP **06**, 088 (2020), arXiv:2002.02317 [hep-th]

[49] E. Brezin and J. Zinn-Justin, Renormalization group approach to matrix models, Phys. Lett. B **288**, 54 (1992), arXiv:hep-th/9206035

[50] B. Ydri, The One-plaquette model limit of NC gauge theory in 2D, Nucl. Phys. B **762**, 148 (2007), arXiv:hep-th/0606206

[51] A. Pelissetto and E. Vicari, Critical phenomena and renormalization group theory, Phys. Rept. **368**, 549 (2002), arXiv:cond-mat/0012164

[52] J.-B. Zuber, Introduction to random matrices (2012), https://www.lpthe.jussieu.fr/ zuber/RMT_2012.pdf

[53] B. Eynard, T. Kimura, and S. Ribault, Random matrices (2015), arXiv:1510.04430 [math-ph]

[54] R. J. Szabo, Quantum field theory on noncommutative spaces, Phys. Rept. **378**, 207 (2003), arXiv:hep-th/0109162

[55] J. Madore, An introduction to noncommutative differential geometry and its physical applications, Vol. 257 (2000)

[56] V. Rivasseau, Non-commutative Renormalization, Prog. Math. Phys. **53**, 19 (2007), arXiv:0705.0705

[57] L. Nenadović, Properties of classical and quantum field theory on a curved noncommutative space, Ph.D. thesis, University of Belgrade, Faculty of Physics (2017), https://nardus.mpn.gov.rs/handle/123456789/9453

[58] A. Armoni, Noncommutative Two-Dimensional Gauge Theories, Phys. Lett. B **704**, 627 (2011), arXiv:1107.3651 [hep-th]

[59] R. Horvat, A. Ilakovac, J. Trampetić, and J. You, On UV/IR mixing in noncommutative gauge field theories, JHEP **12**, 081 (2011), arXiv:1109.2485 [hep-th]

[60] S. F. Viñas and P. Pisani, Worldline approach to the Grosse-Wulkenhaar model, JHEP **11**, 087 (2014), arXiv:1406.7336 [hep-th]

[61] R. Wulkenhaar, Renormalisation of noncommutative ϕ^4_4-theory to all orders, Habilitation thesis, TU Wien, Faculty of Physics (2004), https://ivv5hpp.uni-muenster.de/u/raimar/publications/habilitation/raimar-habil.pdf

[62] B. Ydri, Computational Physics: An Introduction to Monte Carlo Simulations of Matrix Field Theory (World Scientific, Singapore, 2017) arXiv:1506.02567 [hep-lat]

[63] M. Betancourt, A Conceptual Introduction to Hamiltonian Monte Carlo (2018), arXiv:1701.02434 [stat.ME]

[64] S. Brooks, A. Gelman, G. L. Jones, and X.-L. Meng, Handbook of Markov Chain Monte Carlo (Chapman & Hall/CRC, 2011)

[65] A. Beskos, N. Pillai, G. Roberts, J.-M. Sanz-Serna, and A. Stuart, Optimal tuning of the hybrid Monte Carlo algorithm, Bernoulli **19**, 1501 (2013)

[66] G. Franzese, A. Fierro, A. De Candia, and A. Coniglio, Autocorrelation functions in 3D fully frustrated systems, Physica A: Statistical Mechanics and its Applications **257**, 376 (1998)

[67] S. Frühwirth-Schnatter, Finite mixture and Markov switching models, 1st ed. (Springer, Berlin, 2006)

[68] S. Kováčik and J. Tekel, Eigenvalue-flipping algorithm for matrix Monte Carlo, JHEP **04**, 149 (2022), arXiv:2203.05422 [hep-lat]

[69] D. Prekrat, Renormalization footprints in the phase diagram of the Grosse-Wulkenhaar model, Phys. Rev. D **104**, 114505 (2021), arXiv:2104.00657 [hep-th]

[70] D. Anninos and B. Mühlmann, Notes on matrix models (matrix musings), Journal of Statistical Mechanics: Theory and Experiment **2020**, 083109 (2020)

[71] E. Brezin, C. Itzykson, G. Parisi, and J. B. Zuber, Planar Diagrams, Commun. Math. Phys. **59**, 35 (1978)

[72] V. G. Filev and D. O'Connor, On the Phase Structure of Commuting Matrix Models, JHEP **08**, 003 (2014), arXiv:1402.2476 [hep-th]

[73] S. Kawamoto, T. Kuroki, and D. Tomino, Renormalization group approach to matrix models via noncommutative space, JHEP **08**, 168 (2012), arXiv:1206.0574 [hep-th]

[74] S. R. Das, A. Dhar, A. M. Sengupta, and S. R. Wadia, New Critical Behavior in $d = 0$ Large N Matrix Models, Mod. Phys. Lett. A **5**, 1041 (1990)

[75] M. Burić, J. Madore, and L. Nenadović, Spinors on a curved noncommutative space: coupling to torsion and the Gross–Neveu model, Class. Quant. Grav. **32**, 185018 (2015), arXiv:1502.00761 [hep-th]

[76] G. W. Semenoff and R. J. Szabo, Fermionic matrix models, Int. J. Mod. Phys. A **12**, 2135 (1997), arXiv:hep-th/9605140

[77] I. Aref'eva and I. Volovich, Spontaneous symmetry breaking in fermionic random matrix model, JHEP **10**, 114 (2019), arXiv:1902.09970 [hep-th]

[78] W. Janke, D. A. Johnston, and R. Kenna, Properties of higher-order phase transitions, Nucl. Phys. B **736**, 319 (2006), arXiv:cond-mat/0512352

[79] D. Prekrat, D. Ranković, N. K. Todorović-Vasović, S. Kováčik, and J. Tekel, Approximate treatment of noncommutative curvature in quartic matrix model (2022), arXiv:2209.00592 [hep-th]

Curriculum Vitae

Dragan Prekrat was born on July 2nd 1982 in Pančevo, Serbia. After finishing Mathematical High School in Belgrade (MHB) in 2001, he enrolled on the Theoretical and Experimental Physics at the University of Belgrade – Faculty of Physics, (UB-Phys). He graduated in 2009 (9.62/10 GPA) by defending his thesis (grade 10/10) titled *Hawking radiation*, which was supervised by Prof. Dr Maja Burić. Afterwards, during 2009/2010, he completed MSc courses at UB-Phys (9.50/10 GPA), and in 2010 started his PhD studies (9.00/10 GPA) under the supervision of Prof. Dr Maja Burić. Due to delays with paper publication during the COVID-19 pandemic, he re-enrolled in 2021.

From 2011 to 2022, Dragan Prekrat was employed at UB-Phys, as a part of the government-funded national research project No. 171031, *Physical Implications of Modified Spacetime*, first as a Research Trainee and since 2017 as a Research Assistant. During this period, he also worked part-time as a Physics Teacher in MHB (2013/2014), and as a Teaching Associate at the University of Belgrade – Faculty of Pharmacy (UB-Pharm, 2014-2022). In 2022, he started working as a Teaching Assistant for Physics course at UB-Pharm.

During his PhD studies, he visited LMU Munich (2010-2011) and DIAS Dublin (2017 and 2018, COST Action MP1405). He participated in several international conferences and helped organize the *GR100* event (2015). He is a member of the Group for Gravitation, Particles, and Fields at the Institute of Physics Belgrade, and the Center for Quantum Theoretical Physics at UB-Phys.

Dragan Prekrat (co-)authored three publications in leading international journals. His research areas are noncommutative quantum field theories, phase transitions in matrix models, and Monte Carlo Simulations.

Biografija

Dragan Prekrat je rođen 2. jula 1982. godine u Pančevu. Po završetku Matematičke gimnazije u Beogradu 2001. godine, započeo je osnovne akedemske studije na Fizičkom fakultetu Univerziteta u Beogradu (UB-Fiz), na smeru Teorijska i eksperimentalna fizika. Tu je i diplomirao 2009. godine sa prosečnom ocenom 9,62 i ocenom 10 na diplomskom radu na temu *Hokingovo zračenje* pod rukovodstvom prof. dr Maje Burić. Na UB-Fiz je 2009/2010. godine pohađao i kurseve sa master studija sa prosečnom ocenom 9,50. Doktorske akademske studije na UB-Fiz je prvi put upisao 2010. godine rukovodstvom prof. dr Maje Burić. Usled isteka roka studiranja zbog zastoja u recenziranju radova tokom pandemije COVID-19, iste je ponovo upisao 2021. Ispite sa doktorskih studija je položio sa prosečnom ocenom 9,00.

Od 2011. do 2022. godine, Dragan Prekrat je bio zaposlen na UB-Fiz, prvo kao istraživač pripravnik na nacionalnom projektu *Fizičke implikacije modifikovanog prostor-vremena* (MPNTR, br. 171031), a od 2017. kao istraživač saradnik. Takođe je predavao fiziku u Matematičkoj gimnaziji u Beogradu (2013/2014) i radio kao kao saradnik u nastavi na Farmaceutskom fakultetu Univerziteta u Beogradu (2014-2022), gde je 2022. izabran za asistenta.

Tokom studija, boravio je na LMU u Minhenu (2010/2011) kao i na institutu DIAS u Dablinu (2017. i 2018, COST akcija MP1405). Bio je učesnik više međunarodnih škola i konferencija, a 2015. član organizacionog odbora skupa *100 godina Opšte teorije relativnosti*. Član je Grupe za gravitaciju, čestice i polja na Institutu za fiziku u Beogradu i Centra za kvantnu i teorijsku fiziku na UB-Fiz.

Dragan Prekrat je (ko)autor tri rada u M21 časopisima. Bavi se nekomutativnom kvantnom teorijom polja, matričnim modelima na nekomutativnim prostorima i Monte Karlo simulacijama.

образац изјаве о ауторству

Изјава о ауторству

Име и презиме аутора Драган Прекрат

Број индекса 8030/2021

Изјављујем

да је докторска дисертација под насловом

Phase transitions in matrix models on the truncated Heisenberg space

- резултат сопственог истраживачког рада;
- да дисертација у целини ни у деловима није била предложена за стицање друге дипломе према студијским програмима других високошколских установа;
- да су резултати коректно наведени и
- да нисам кршио/ла ауторска права и користио/ла интелектуалну својину других лица.

Потпис аутора

У Београду, 5.9.2022.

Прекрат Драган

образац изјаве о истоветности штампане и електронске верзије докторског рада

Изјава о истоветности штампане и електронске верзије докторског рада

Име и презиме аутора Драган Прекрат

Број индекса 8030/2021

Студијски програм Квантна поља, честице и гравитација

Наслов рада Phase transitions in matrix models on the truncated Heisenberg space

Ментор проф. др Маја Бурић

Изјављујем да је штампана верзија мог докторског рада истоветна електронској верзији коју сам предао/ла ради похрањивања у **Дигиталном репозиторијуму Универзитета у Београду.**

Дозвољавам да се објаве моји лични подаци везани за добијање академског назива доктора наука, као што су име и презиме, година и место рођења и датум одбране рада.

Ови лични подаци могу се објавити на мрежним страницама дигиталне библиотеке, у електронском каталогу и у публикацијама Универзитета у Београду.

Потпис аутора

У Београду, 5.9.2022.

Прекрат Драган

образац изјаве о коришћењу

Изјава о коришћењу

Овлашћујем Универзитетску библиотеку „Светозар Марковић“ да у Дигитални репозиторијум Универзитета у Београду унесе моју докторску дисертацију под насловом:

Phase transitions in matrix models on the truncated Heisenberg space

која је моје ауторско дело.

Дисертацију са свим прилозима предао/ла сам у електронском формату погодном за трајно архивирање.

Моју докторску дисертацију похрањену у Дигиталном репозиторијуму Универзитета у Београду и доступну у отвореном приступу могу да користе сви који поштују одредбе садржане у одабраном типу лиценце Креативне заједнице (Creative Commons) за коју сам се одлучио/ла.

[✓ 1. Ауторство (CC BY)]

2. Ауторство – некомерцијално (CC BY-NC)

3. Ауторство – некомерцијално – без прерада (CC BY-NC-ND)

4. Ауторство – некомерцијално – делити под истим условима (CC BY-NC-SA)

5. Ауторство – без прерада (CC BY-ND)

6. Ауторство – делити под истим условима (CC BY-SA)

(Молимо да заокружите само једну од шест понуђених лиценци.
Кратак опис лиценци је саставни део ове изјаве).

Потпис аутора

У Београду, 5.9.2022.